

Degano, Marco (2012) EMI filter design for matrix converters in airspace applications. PhD thesis, University of Nottingham.

Access from the University of Nottingham repository:

http://eprints.nottingham.ac.uk/12744/1/Marco_Degano_PhD.pdf

Copyright and reuse:

The Nottingham ePrints service makes this work by researchers of the University of Nottingham available open access under the following conditions.

- Copyright and all moral rights to the version of the paper presented here belong to the individual author(s) and/or other copyright owners.
- To the extent reasonable and practicable the material made available in Nottingham ePrints has been checked for eligibility before being made available.
- Copies of full items can be used for personal research or study, educational, or not-for-profit purposes without prior permission or charge provided that the authors, title and full bibliographic details are credited, a hyperlink and/or URL is given for the original metadata page and the content is not changed in any way.
- Quotations or similar reproductions must be sufficiently acknowledged.

Please see our full end user licence at:

http://eprints.nottingham.ac.uk/end_user_agreement.pdf

A note on versions:

The version presented here may differ from the published version or from the version of record. If you wish to cite this item you are advised to consult the publisher's version. Please see the repository url above for details on accessing the published version and note that access may require a subscription.

For more information, please contact eprints@nottingham.ac.uk



The University of
Nottingham

UNITED KINGDOM · CHINA · MALAYSIA

EMI Filter Design for Matrix Converters in Airspace Applications

Dott. Ing. Marco Degano

Thesis submitted to The University of Nottingham
for the degree of Doctor of Philosophy, December 2012

Abstract

Advanced power electronics systems are increasingly being used for AC motor drives, due to their numerous advantages in terms of performance and flexibility. In a bid to improve system performance and reduce converter size, higher switching frequencies are being used; this however pushes switching frequencies harmonics into the MF band (300 kHz to 3 MHz) and possibly even into the HF band (3 MHz to 30 MHz). Interest in the research of the electromagnetic interference produced by power electronics and drives systems has therefore grown over the past few years. To study, reduce or even possibly eliminate any interaction with other appliances, suitable EMI filters need to be designed and implemented. Such a need for developing filtering devices requires accurate HF models for the polluting system to be developed.

The focus of this thesis is on the characterization of a matrix converter induction motor drive for aerospace application from the point of view of EMI interference and on the design and implementation of suitable filtering systems. Concerns about Electro Magnetic Interferences are particularly justified in the light of the fact that high reliability is sought after in such applications. Failures of aircrafts' subsystems could have catastrophic consequences, therefore strict standards [1] regulating environmental susceptibility, electromagnetic interference and mechanical testing; amongst others, of such subsystems, need to be adhered to. The main interest in this work lies in the electromagnetic regulations defining the allowable conducted emissions in the frequencies between 150 kHz and 30 MHz. Parasitic elements play a dominating role in the behaviour of the system in this frequency range. The problem is that they are difficult to identify and model since they are not always directly associable to a specific component, therefore every possible path for the currents have to be considered.

The first goal achieved by this work is to characterize the EMI signature of a matrix converter induction motor drive using common and differential mode measurements of the converter and motor impedances separately. Based only on these measurements the project aims to synthesize accurate HF models for the Induction Motor and the Matrix Converter in common and differential mode, without the need of deep level studies

that may involve long Finite Elements (FE) simulations of the physical system characteristics. This thesis proposes two general novel HF models for Matrix Converters and Induction Motors that could also be applied in any other application or operating condition. These models are automatically tuned and optimized by a suitably developed Genetic Algorithm (GA) routine capable to match those models with real experimental measurements. The aforementioned will be then used in a detailed simulation of the whole drive system to validate the modelling procedure. Following this, a suitable EMI filter complying with the stated regulations on the basis of the developed modelling is implemented. This thesis reports the methodologies used for both input and output filter design, together with description and analysis of some issues encountered during the process. The EMI output filter has been physically set-up; the experimental procedure of its realization is reported in this work, including novel design choices and analysis at a device level. Different emissions measurement taken before and after the filter insertion are presented and discussed, showing the effectiveness of the implemented filtering system.

Contents

1	Introduction	1
1.1	Introduction to Electromagnetic Compatibility	1
1.2	EMI related to power converters	3
1.3	Instruments for EMI measurement	5
1.4	EMC mitigation strategies	7
1.5	Literature review and background	10
1.6	Existing HF models	12
1.7	Aims and objectives	13
1.8	Structure of the thesis	14
2	Experimental implementation of matrix converter drive	16
2.1	Introduction	16
2.2	Introduction on Matrix converters	16
2.2.1	Modulation	17
2.2.2	Commutation strategies	19
2.3	Matrix converter chosen for the experimental tests	21
2.3.1	Hardware improvements	23
2.4	Controller boards	24
2.5	Measurement transducers	25
2.6	Motor drive and control technique	26
2.7	Experimental test at full voltage	28
3	HF Modelling Strategy	29

CONTENTS

3.1	Introduction	29
3.2	Impedance measurements	29
3.3	Genetic Algorithms and their use for structural identification	31
3.4	HF model simulations	36
4	Motor and matrix converter model	39
4.1	Introduction	39
4.2	HF motor modelling with Casadei's model	39
4.2.1	Difficulty to find adequate models	40
4.3	Suggested HF Motor model	41
4.3.1	Attempt to reduce optimizing time	43
4.3.2	Matching with impedance measurements	44
4.4	Matrix converter model	45
4.4.1	Input and output CM impedance characterization	48
4.4.2	Input and output DM impedance characterization	50
4.5	GA to model other components	51
4.5.1	Modelling of the LISN	51
4.6	Cable model	53
5	EMI Measurements	56
5.1	Introduction	56
5.2	Requirements for conducted EMI	57
5.3	Probe calibration	57
5.3.1	Calibration procedure	59
5.4	Experimental current measurements: CM & DM	61
5.5	Actual measurements	63
5.5.1	EMI Comparison with a two level inverter	67
6	Simulations of input and output system EMI	71
6.1	Introduction	71
6.2	Implementation of Matrix converter Modulation in Saber simulator	71

CONTENTS

6.3	Saber frequency analysis validation	73
6.4	LF motor model	74
6.5	Complete Matrix converter drive HF model	77
6.6	Output EMI simulations	79
6.7	Input EMI simulations	81
7	Filter Design and realization	82
7.1	Introduction	82
7.2	Output filter: identification of the attenuation required	82
7.3	Design of filter components	84
7.3.1	DM inductor design with Ferrites	85
7.3.2	DM filter Capacitors choice	87
7.4	DM output filter implementation	89
7.4.1	Frequency positioning of the DM filter resonance	91
7.4.2	Powerlite C material	91
7.5	CM output filter implementation	93
7.6	HF Modelling the output filter	96
7.7	Input DM and CM filter design	98
8	Filter realization and experimental results	102
8.1	Introduction	102
8.2	Assembling the output filter	102
8.3	Experimental emission measurements	103
8.3.1	Input emissions	104
8.3.2	Output emissions	107
8.3.3	Influence of the modulation index q on the emissions	110
9	Conclusions and Further work	114
A	Scientific Publications	116
A.1	Papers published on refereed International Journals	116
A.2	Papers published on refereed International Conferences	117

CONTENTS

B External DLL	118
B.1 C code	118
B.2 MAST code	122
References	124

List of Figures

1.1	Decomposition of EMC problem	1
1.2	Output current of matrix converter	3
1.3	Frequency spectrum of the current in Fig. 1.2	4
1.4	Example of DM and CM current paths: PWM-VSI [2]	4
1.5	Spectrum analyzer block diagram (Agilent, AN 150)	6
1.6	Frequency mixer operation (Agilent, AN 150)	6
1.7	π filter, single and double stage	9
1.8	L filter, single and double stage	9
1.9	T filter, single and double stage	9
1.10	Feedthrough capacitor with its symbol	10
1.11	Scheme of a matrix converter	11
1.12	Proposed circuit by Yaskawa et al. [3]	11
1.13	HF Motor models chosen for preliminary simulations.	13
2.1	Matrix concept	16
2.2	IGBT module used	19
2.3	Output voltage comparison for modulation techniques	20
2.4	4 step commutation sequence	21
2.5	Matrix converter used	22
2.6	New control boards	23
2.7	Clamp circuit schematic	23
2.8	V/f control technique	27
2.9	V/f implementation	27

LIST OF FIGURES

2.10	Measurement at full voltage	28
3.1	Example of error integration for impedance	34
3.2	Explanation of area calculation for double triangle case	35
3.3	HF Motor model in Simulink with topology toggling resistors	37
3.4	Matrix converter input capacitor equivalent network	38
4.1	Casadei's HF induction motor schematic	40
4.2	Motor: parasitic impedance measurement	41
4.3	Motor: common and differential mode impedance measurement	41
4.4	Attempt to fit motor's parasitics with model as in [4]	42
4.5	Proposed HF motor model	43
4.6	Motor's model parasitic fitting	44
4.7	Motor's model common mode fitting	46
4.8	Motor's model differential mode fitting	47
4.9	Matrix input capacitor equivalent network	47
4.10	Matrix input capacitor measured and fitted impedance	47
4.11	Matrix input parasitic network	49
4.12	Matrix output parasitic network	49
4.13	Matrix input CM: matching of the measured and simulated impedance	50
4.14	Matrix output CM: matching of the measured and simulated impedance	50
4.15	Procedure to calculate analytically the impedance across a-bc	51
4.16	Matrix converter input DM: matching of the measured and simulated impedance	52
4.17	Matrix converter output DM: matching of the measured and simulated impedance	52
4.18	Lisn schematic	53
4.19	Lisn: matching of the reference and simulated impedance	53
4.20	Cable model	54
5.1	Typical Setup for Conducted RF Interference Test	58
5.2	Maximum Level of Conducted RF Interference – Power Lines	58

LIST OF FIGURES

5.3	Calibration curve for current probe FCC F-35A	59
5.4	Setup for current probe calibration	61
5.5	Path for common and differential mode currents for two and three wire systems	62
5.6	CM and DM current measurement for a two wire system	62
5.7	CM and DM current measurement for a three wire system	63
5.8	CM current measurement for the Matrix converter input	64
5.9	DM current measurement for the Matrix converter input	64
5.10	CM current measurement for the Matrix converter output, motor side	65
5.11	DM current measurement for the Matrix converter output, motor side	65
5.12	Output current for different values of modulation index q	66
5.13	DM EMI at Matrix converter input varying q	66
5.14	CM EMI at Matrix converter input varying q	66
5.15	DM EMI at Matrix converter output varying q	67
5.16	CM EMI at Matrix converter output varying q	67
5.17	Input DM EMI comparison for Matrix and Two-level converters	68
5.18	Input CM EMI comparison for Matrix and Two-level converters	68
5.19	Output DM EMI comparison for Matrix and Two-level converters	68
5.20	Output CM EMI comparison for Matrix and Two-level converters	69
5.21	CM Voltage measurement for Matrix converter	70
5.22	CM Voltage measurement for Two-level converter	70
6.1	Output V_{ab} simulation/measurement comparison	73
6.2	Experimental setup for spectrum measurements validation	74
6.3	Output V_{ab} simulation/measurement comparison	75
6.4	Measured voltage and current at the motor	76
6.5	Cross-correlation between voltage and current	76
6.6	Matrix ideal switch model for one output phase	77
6.7	Complete HF model	78
6.8	Datasheet of input filter ETS N1825	79

LIST OF FIGURES

6.9	CM Conducted EMI, output	80
6.10	DM Conducted EMI, output	80
6.11	CM Conducted EMI, input	81
6.12	DM Conducted EMI, Input	81
7.1	Output DM filter design	85
7.2	Permeability of Ferroxcube 3E27[5] and Epcos N30[6] materials	86
7.3	Permeability of Magnetics J material[7]	86
7.4	B/H curve for material N30[6]	87
7.5	Emission with DM filter using J material	89
7.6	Comparison of DM emissions with filter made of J or AMCC material	90
7.7	Output current after DM filter insertion, inductor with AMCC alloy	90
7.8	Output current after DM filter insertion, inductor with J ferrite	90
7.9	Bode plot of output DM filter	91
7.10	Permeability vs. Temperature for Powerlite C-cores[8]	92
7.11	Output CM emissions after DM filter insertion	92
7.12	Output CM emissions after DM filter insertion	94
7.13	Output DM emissions after DM filter insertion	94
7.14	Schematic of the output filter	95
7.15	Inductor model	96
7.16	DM Inductor: matching of the measured and simulated impedance	97
7.17	DM Inductor: matching of the measured and simulated impedance	97
7.18	Ferrite tube model	97
7.19	Ferrite tube: matching of the measured and simulated impedance	98
7.20	DM output filter: matching of the measured and simulated impedance	98
7.21	CM output filter: matching of the measured and simulated impedance	98
7.22	Bode plot of input DM filter	99
7.23	Input DM emissions estimation after DM filter insertion	100
7.24	Input CM emissions estimation after filter insertion	101
7.25	Schematic of the input filter	101

LIST OF FIGURES

8.1	Output filter with component details	103
8.2	Comparison of Measured input DM emissions: without and with output EMI filter (115V-400Hz to 80V-50Hz)	104
8.3	Comparison of Measured input DM emissions: without and with output EMI filter (115V-400Hz to 80V-100Hz)	104
8.4	Comparison of Measured input CM emissions: without and with output EMI filter (115V-400Hz to 80V-50Hz)	105
8.5	Comparison of Measured input CM emissions: without and with output EMI filter (115V-400Hz to 80V-100Hz)	105
8.6	Comparison of Measured input DM emissions: without and with output EMI filter (240V-50Hz to 168V-50Hz)	106
8.7	Comparison of Measured input DM emissions: without and with output EMI filter (240V-50Hz to 168V-100Hz)	106
8.8	Comparison of Measured input CM emissions: without and with output EMI filter (240V-50Hz to 168V-50Hz)	106
8.9	Comparison of Measured input CM emissions: without and with output EMI filter (240V-50Hz to 168V-100Hz)	107
8.10	Comparison of Measured output DM emissions: without and with output EMI filter (115V-400Hz to 80V-50Hz)	107
8.11	Comparison of Measured output DM emissions: without and with output EMI filter (115V-400Hz to 80V-100Hz)	108
8.12	Comparison of Measured input CM emissions: without and with output EMI filter (115V-400Hz to 80V-50Hz)	108
8.13	Comparison of Measured input CM emissions: without and with output EMI filter (115V-400Hz to 80V-100Hz)	108
8.14	Comparison of Measured output DM emissions: without and with output EMI filter (240V-50Hz to 168V-50Hz)	109
8.15	Comparison of Measured output DM emissions: without and with output EMI filter (240V-50Hz to 168V-100Hz)	109
8.16	Comparison of Measured input CM emissions: without and with output EMI filter (240V-50Hz to 168V-50Hz)	110
8.17	Comparison of Measured input CM emissions: without and with output EMI filter (240V-50Hz to 168V-100Hz)	110

LIST OF FIGURES

8.18 Input CM and DM emissions for different values of modulation index q (115V-400Hz input, 100Hz output)	111
8.19 Output DM emissions for different values of modulation index q (115V-400Hz input, 100Hz output)	112
8.20 Output CM emissions for different values of modulation index q (115V-400Hz input, 100Hz output)	112
8.21 Input CM and DM emissions for different values of modulation index q (240V-50Hz input, 50Hz output)	113
8.22 Output DM emissions for different values of modulation index q (240V-50Hz input, 50Hz output)	113
8.23 Output CM emissions for different values of modulation index q (240V-50Hz input, 50Hz output)	113

List of Tables

2.1	Pin-Out of Matrix control signal	24
2.2	Pin-Out of Matrix analog signals	24
3.1	Used parameters for Genetic Algorithms	33
4.1	Parasitics optimized parameters for proposed HF motor model	42
4.2	CM optimized parameters	45
4.3	DM optimized parameters	46
4.4	Matrix converter input capacitors model values	46
4.5	Matrix converter input and output parasitics model values	48
4.6	LISN main inductor values, in order from line side to load side	54
4.7	Input cable, dimensions and model parameters	55
4.8	Output cable, dimensions and model parameters	55
6.1	Comparison of LF motor parameters obtained with FFT and correlation	76
7.1	Type of filters for EMI applications [9]	83
7.2	Attenuation for crucial points in DM output emissions	84
7.3	List of toroids available with magnetic characteristics for $I_{peak}=1A$	88
7.4	Attenuation for crucial points in CM output emissions	93
7.5	List of material for EMI output filter	95
7.6	Model parameters	96
7.7	Model parameters	97
7.8	Attenuation for crucial points in DM input emissions	99

LIST OF TABLES

7.9	Attenuation for crucial points in CM input emissions	100
8.1	Modulation index and motor rms current for measurements with aircraft supply at 115V, 400Hz	111
8.2	Modulation index and motor rms current for measurements with standard supply at 240V, 50Hz	111

Introduction

1.1 Introduction to Electromagnetic Compatibility

Electromagnetic Compatibility (EMC) is the study of the interaction that occurs among electronic systems when energy is radiated from an emitter through electromagnetic fields or is conducted via voltages or currents, and it is received by an appliance. The reception of unwanted energy occurs frequently via unintended methods and from different sources, however the interference only occurs when it causes an undesired behaviour in the receiver.

Three aspects are matter of concern to the EMC: generation, transmission and reception of electromagnetic energy. These three aspects are related to a source (or emitter), a coupling path where the energy is transferred, and a receiver (Fig. 1.1).



Figure 1.1: Decomposition of EMC problem

There are different sources of electromagnetic waves with wide spectral content, both in Nature such as lightning or cosmic waves, and in man-made appliances, for example DC motors or fluorescent light. Sources of limited spectral content are mostly related to man-created devices like transmitters, where the desired output must be concentrated in a limited part of the electromagnetic spectrum. Nowadays, in addition to these, power converters due to their large dV/dt transitions, are becoming another important source of unwanted radiations that can easily interfere with other devices.

The transfer mechanism can be broken down in two different kinds, *radiated* and *conducted*, depending on whether the energy is passed through radio signals, in which the coupling path is the material between the two devices, or via the interconnecting cables, where the coupling path is the conductive connection shared by the source and

the receiver. The topology of the energy transfer can be either *emissions* or *susceptibility*, depending on whether the focus of the study is on the generated noise or on the received one.

Historically, the first organization to introduce standards to limit the electromagnetic pollution was the *Comité International Spécial des Perturbations Radioélectriques* (CISPR), founded in 1934, now part of *International Electrotechnical Commission* (IEC). Its intention was initially just to protect the sound broadcast services; however nowadays all electronic equipment is both very sensitive to EMI and can produce interference at high frequencies because its internal signals (e.g. clock signals) have frequency in the order of several Mega Hertz. Because of this, now, numerous national and international organizations issue norms related to various aspects of EMC based upon CISPR expertise, limiting specific EMI emissions for internal use by individual countries and organizations, such as armed forces or large corporations. Manufacturers of electric apparatus and systems must comply with the national standards before being allowed to access the market [2].

Standards define the admissible emissions, the measuring setup, the testing circuit layout and the source impedance too. Standards are in continuous evolution, trying to match as close as possible the real conditions that an equipment will find on the field. However this is not an easy task; for example to standardize the test procedure a LISN is usually specified as a source impedance, but its 50 Ohm impedance are not always a good approximation for the generator source impedance, for power converters usually it is much lower. This could lead to a design for an equipment that will pass the lab test because it will be designed to accomplish the standard, but when tested in the real environment it will fail because the actual test conditions will be much different.

Electronic systems that are electromagnetically compatible with their environment implies that they do not produce nor are they susceptible to interference, or in other terms, they must satisfy three criteria [10]:

- It does not cause interference with other systems.
- It is not susceptible to emissions from other systems.
- It does not cause interference with itself.

This is not important just for a functional performance, it is also a legal requirement that must be satisfied before the appliance can be sold, therefore EMC design have become an integral part of any equipment design.

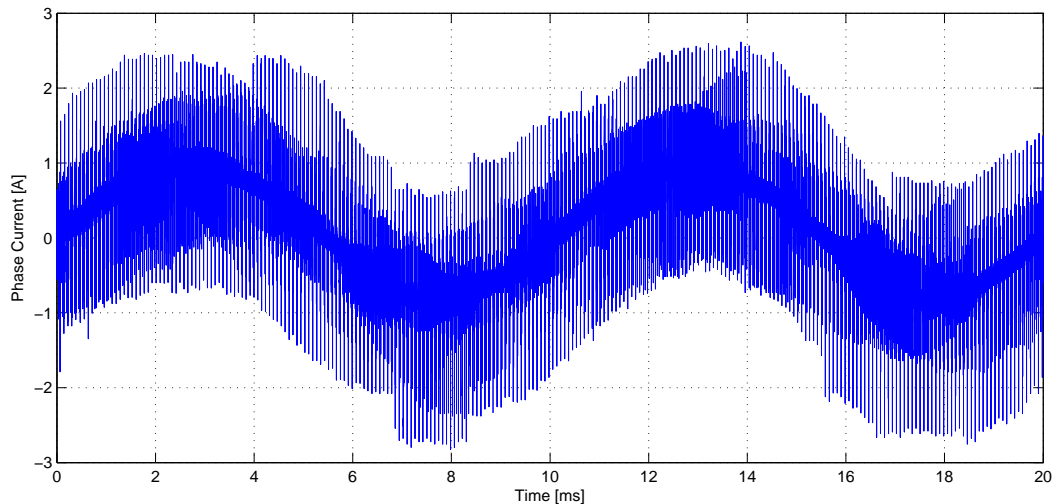


Figure 1.2: Output current of matrix converter

1.2 EMI related to power converters

The introduction of power converters, especially voltage source PWM inverters, granted a powerful control for motor drives, making them the common choice for motor drive systems. Still, they introduced new issues typical of their nature both at the input and the output side, that can mainly be summarized with:

- Bad influence on other electrical systems with the radiated and conducted emissions
- High current harmonics injection on the input, creating power pollution
- Motors insulation failure due to surge voltage at the windings
- Premature bearing failure due to current induced by common mode voltage[11, 12]

All of these problem are due to converters switch-mode operation, that creates ripple current both at the input and at the output. An example to illustrate this behaviour can be seen in Fig. 1.2 which shows the output current of a matrix converter supplied at $240V_{rms}$, 50Hz feeding a 1.5kW asynchronous motor with $170V_{rms}$ at 100Hz. Fig. 1.3 shows the spectrum of waveform in Fig. 1.2 where high frequency components are visible at the multiples of the switching frequency, in this case 12.5kHz. The rapid changes of the switched voltages in power converters, because of the parasitic capacitive coupling, generate currents in the earth path, so they do at the motor side for the same reason. The frequency of interest included in EMI normative are 0.15 – 30MHz, to protect the bandwidth of radio and TV broadcasts. In this range mainly the conducted EMI

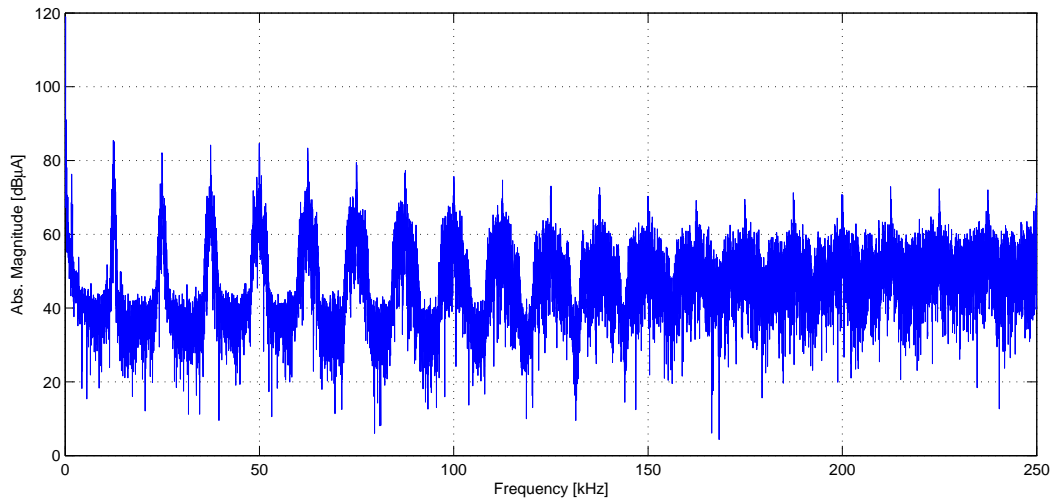


Figure 1.3: Frequency spectrum of the current in Fig. 1.2

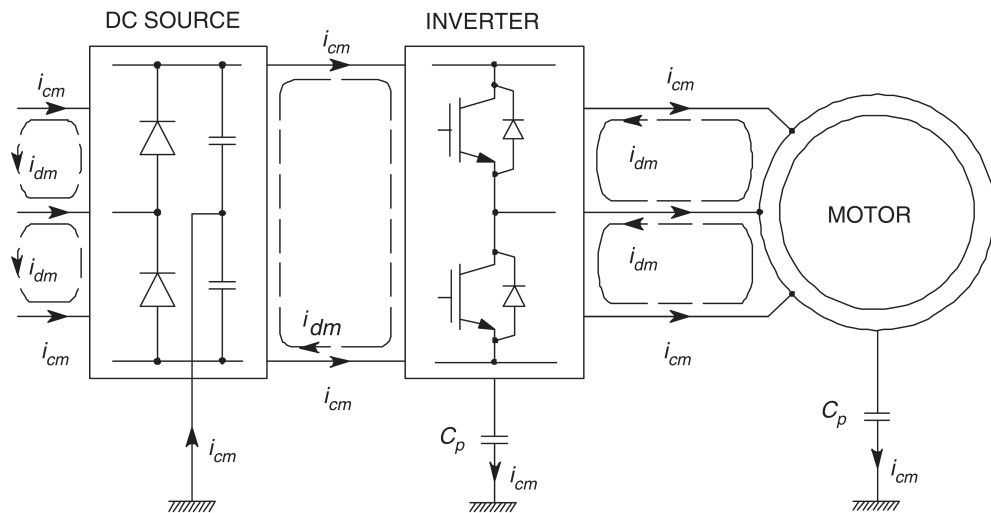


Figure 1.4: Example of DM and CM current paths: PWM-VSI [2]

need to be suppressed, while control over the radiated ones is required only under special circumstances. Conducted EMI appears in the form of common-mode (CM) and differential-mode (DM) voltages and currents; current paths are represented in Fig. 1.4 for a conventional two level inverter with DC link. Common-mode currents, i_{cm} , flow close to ground through parasitic capacitances, C_p , while DM currents, i_{dm} , flow only in the phase wires of the system [2].

Referring to a generic three-phase system, the CM voltage and current are defined as:

$$V_{cm} = \frac{V_1 + V_2 + V_3}{3} \quad (1.2.1)$$

$$I_{cm} = I_1 + I_2 + I_3 \quad (1.2.2)$$

Regarding the differential mode, the differential voltage across wires a and b , for example, is simply:

$$V_{dm} = V_a - V_b \quad (1.2.3)$$

Obtaining the DM current for a phase wire, a for example, is not so straightforward because the measured line current I_a includes both the differential and the common mode, therefore the latter must be subtracted from that measured to obtain the desired value:

$$I_{a_{dm}} = I_a - \frac{I_{cm}}{3} \quad (1.2.4)$$

As mentioned earlier, the high dV/dt transitions, typical of power converters, generate EMI. They are due to the transient charge currents mainly in inter-wire capacitance, semiconductor p-n junctions and parasitic capacitances toward ground. These currents appear as spikes superimposed to the fundamental signal. The currents that close toward ground constitute the CM emissions, the others generate the DM ripple which has a pattern strictly related to the switching frequency and the used modulation.

1.3 Instruments for EMI measurement

There are specific rules that define the instruments to be used for EMI measurements, they are stated on the standard that imposes the limitations on the EMI, according to the specific environment the equipment will be used in. The standards for Aircraft systems which are of interest for the application of this research work, are identified on the DO-160E document, and they define the mode of acquisition for the equipment under test. The measuring instrument is a spectrum analyser, used with the peak detector and a resolution bandwidth of 1kHz. To understand the imposed limits, a brief description on how the instrument works is needed; to this aim the description found on the Agilent's AN 150, is very appropriate:

A spectrum analyser is a frequency-selective, peak-responding voltmeter calibrated to display the rms value of a sine wave.

Basically it decomposes the signal in all of its harmonics and then it records the amplitude for every frequency constituting the measured signal. It has to be pointed out that, because of its implementation, it loses the phase information, therefore from the readings it is not possible to reconstruct the original signal as it would be with the Fourier Transform. Even so this is not an issue because we are interested only in the power of the interference, therefore only the magnitude is required.

A spectrum analyser can be represented with the block scheme in Fig. 1.5. The main

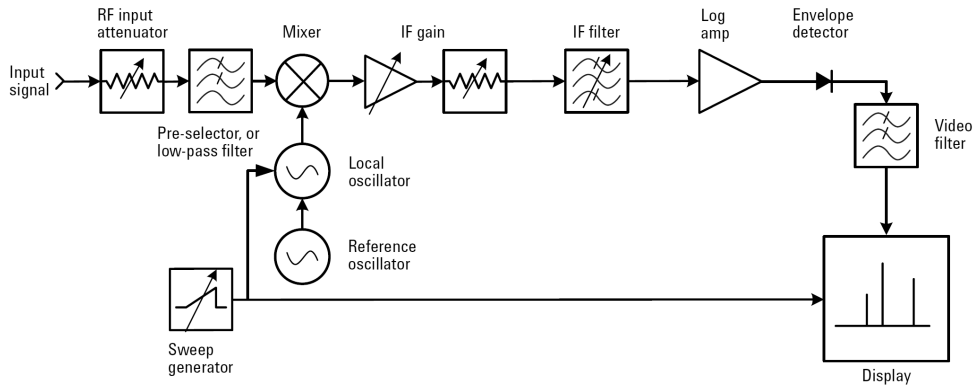


Figure 1.5: Spectrum analyzer block diagram (Agilent, AN 150)

components are: a couple of low/band-pass filters, a local oscillator that provides the sweeping reference signal, a mixer, a detector and some attenuators/amplifiers to optimize the signal level for the processing. The core of the system is the frequency mixer: multiplying two sine waves with frequency f_{sig} and f_{LO} , according to the equation 1.3.1, will generate two new signals, one with frequency $f_{sig} - f_{LO}$ and another with frequency $f_{sig} + f_{LO}$, as represented in Fig. 1.6.

$$\sin f_1 \cdot \sin f_2 = \frac{\cos(f_1 - f_2) - \cos(f_1 + f_2)}{2} \tag{1.3.1}$$

When the result of this multiplication falls within the bandwidth of the intermediate-

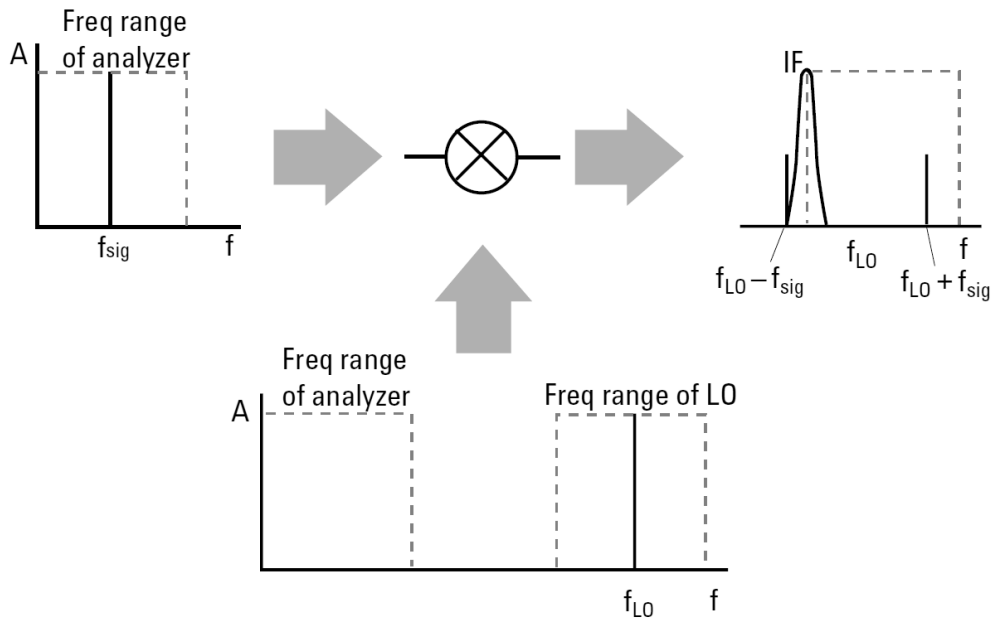


Figure 1.6: Frequency mixer operation (Agilent, AN 150)

frequency (IF) filter, there will be a signal detected and displayed. Extending this concept to a continuous spectrum signal (input) and a frequency sweep for the local oscil-

lator, the resulting output will be the same as having the filter swept throughout the whole spectrum. This frequency mixing, therefore, makes it possible to apply the same resolution filter to all the frequencies under analysis, otherwise it would be impossible to change the filter's center frequency without changing its bandwidth. After this filtering the signal is amplified with a logarithmic amplifier to display a wider range of signals, and is then fed to the detector to be finally displayed on the screen. Modern spectrum analyser, after the frequency mixing, adopt some analog to digital conversion to take advantage of the digital filtering, thus allowing narrower filters and faster sweep time.

The unit of measure for emissions, if it is related to power, usually is the *dBW*, that is defined as

$$P_{dBW} = 10 \cdot \log_{10} P_W \quad (1.3.2)$$

For smaller signals usually the *dBmW* unit is used, and it is simply

$$P_{dBmW} = 10 \cdot \log_{10} P_{mW} \quad (1.3.3)$$

The relationship between the two is:

$$P_{dBmW} = 10 \cdot \log_{10}(P_W \cdot 1000) = 30 + 10 \cdot \log_{10} P_W \quad (1.3.4)$$

The emission limits can be expressed in other units, for example in the DO-160E they are in *dBμA*. Because the spectrum analyser is able to detect voltages, the reading unit must be converted. This can easily be done when the current probe's impedance *Z* is known, with the following equation, and this impedance is usually specified on the datasheet.

$$I_{dB\mu A} = 20 \cdot \log_{10} \frac{V_{\mu V}}{Z} = 20 \cdot \log_{10} V_{\mu V} - 20 \cdot \log_{10} Z \quad (1.3.5)$$

A particular case for this is when some current probes (current clamps) have an unitary impedance for a defined frequency range, for them the last term will be 0, making the two measurements of voltage and current actually coincident, therefore the reading of *dBμV* will be the same as for the *dBμA*, removing the need for any conversion.

1.4 EMC mitigation strategies

In order to minimise the interaction between appliances, there are basically three possible ways for a generic appliance [10]:

- **Suppress the emission at its source:** the device must be optimized to reduce the generation of EMI, with proper layout, smoothing transients and possibly adding an EMI filter for input and output.

- **Make the coupling path as inefficient as possible:** shield every possible input for external noise (using shielded/twisted cables) and place the device as far as possible from known EMI sources.
- **Make the receiver less susceptible to the emission:** filter the inputs or adopt error correction techniques to limit the noise influence on the overall performance.

Possibly, during the design and EMC study, all of them must be considered and optimized, not to create problems to other devices and to minimize susceptibility to external noise. However, the first point is the one to closely keep under consideration at the design stage because small design details at this point, such as keeping the current loops as close as possible or providing some shielding for the noisy sections of the circuit, can reduce a lot the emissions thus simplifying greatly the filter design procedure.

Despite all of this, for a power converter, the need for an EMI filter for the input and the output is usually a must, and the common solutions are passive low-pass filters like capacitors or inductive-capacitive (LC) networks. After simulating or measuring the required attenuation, the filter topology has to be chosen according to the magnitude of the attenuation and the application of the filter. The typical non dissipative filters for EMI applications are three, as reported in [9]: L, T and π filter. They can be used either in single or multiple stage configuration to increase the filtering capability.

- The single π filter [Fig 1.7] has an attenuation of 60dB/dec, in double stage it attenuates 100 dB/dec. This filter is very good when the line to ground capacitors are not an issue, but it will present problems if used on a converter's output stage because of the high inrush current through the switching devices at every commutation. Also it would not be a good choice if there are limitations on the overall capacitance line-to-line or line-to-ground.
- The L filter [Fig 1.8] is the one used the most, in spite of its lower attenuation: just 40 dB/dec for the single stage and 80 dB/dec for the double stage. It works well to feed power converters and it reduces the number of components to be used, limiting in this way the total capacitance and the total weight mainly due to the inductors.
- The T filter [Fig 1.9] has the same attenuation of the π filter, it is desirable for a low impedance line (high current demand) when the values of the inductors are not too high. Anyway this filter topology will starve the switchers if used to feed a power converter because of its output inductor.

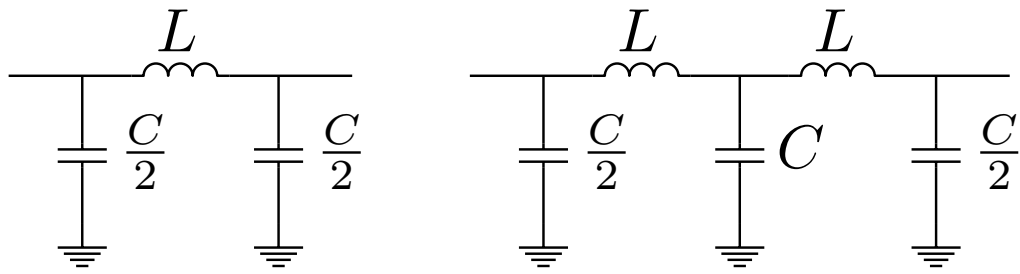


Figure 1.7: π filter, single and double stage

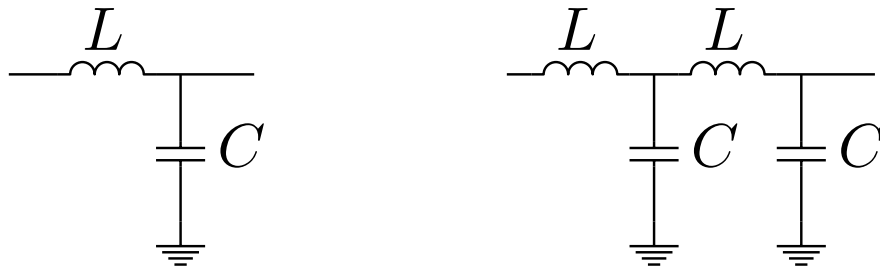


Figure 1.8: L filter, single and double stage

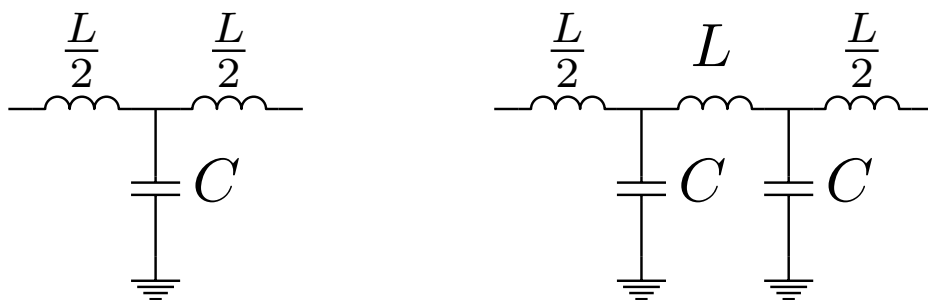


Figure 1.9: T filter, single and double stage



Figure 1.10: Feedthrough capacitor with its symbol

To realize these filters, choke coils are used as inductors, with high frequency ferrite cores commonly made out of iron powder. For the CM inductor all the phases are wound on the same core in a way that the total flux created will be nearly zero. This will allow the core to be designed only for a small fraction of the rated current, reducing its size without compromising its effectiveness.

As regarding to the capacitors, they must have a low parasitic series inductance to perform well at the high frequency involved. The best capacitors under this aspect are the feedthrough capacitors, Fig. 1.10. They have three contacts: two are the two sides of a metal rod where the phase current flows, while all around it there is the dielectric and an enclosure for the ground contact. They provide the shortest possible path for the current to be coupled to the third contact (ground), granting the lowest equivalent series inductance. These capacitors, nevertheless, are very application specific so are both expensive and difficult to find. More common type of capacitors used are the class X and Y capacitor. Their dielectric can be paper, metallized paper, polystyrene or ceramic. The class specify the grade of electric insulation the capacitor is granted to withstand, and it's related to the application it is supposed to be used. X capacitors are meant to be used across line phases, so that a short circuit will not cause any risk to personnel. Y capacitor are supposed to be used as capacitance towards ground. The use of these requires more strict rules to be followed because a short failure will connect the phase directly to the ground (usually the casing), posing a serious threat of electrical shock to the user.

1.5 Literature review and background

In the literature there are plenty of studies on the EMI problems related to power converters. For example [13–18] to cite just a few, deal with HF interference mitigation for normal PWM converters, suggesting solutions to attenuate the high-frequency noise created by the switches by means of the introduction of passive L or LC EMI filters. Others articles implement an active circuit to minimize these currents, such as [19, 20]

that, with a push-pull network driven by a forth winding on the common mode choke, compensate the CM current thus reducing the voltage of the motor's shaft.

However, the design of EMI filters for a matrix converter (Fig. 1.11) is a rather new challenge since this topology of converter, even if so interesting, is not largely utilized yet. In commercial applications the idea of the Matrix Converter has been introduced

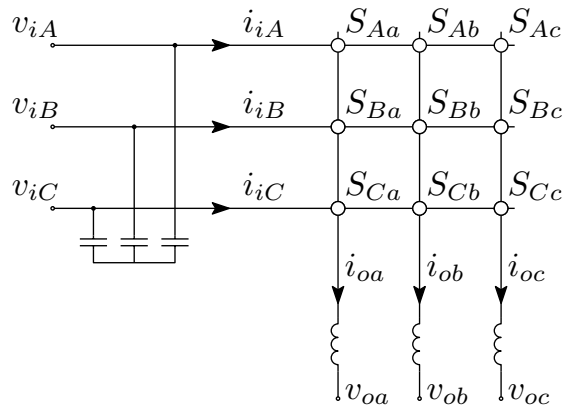


Figure 1.11: Scheme of a matrix converter

because it allows some improvements compared to the standard two level inverter: mainly it has reduced power losses because the voltages are lower and it does not need bulky electrolytic capacitors, thus leading to a miniaturization of the whole converter, with the possibility of a direct integration within the end-plate of the machine [21]. More details about the matrix converter system will be provided in the next chapter, where the experimental matrix converter will be described.

About the EMI mitigation for matrix converters, some work has been done by Yaskawa et al. [3, 22]; they presented integrated filters for the input and the output of the converter to reduce common and differential mode conducted emission. They designed

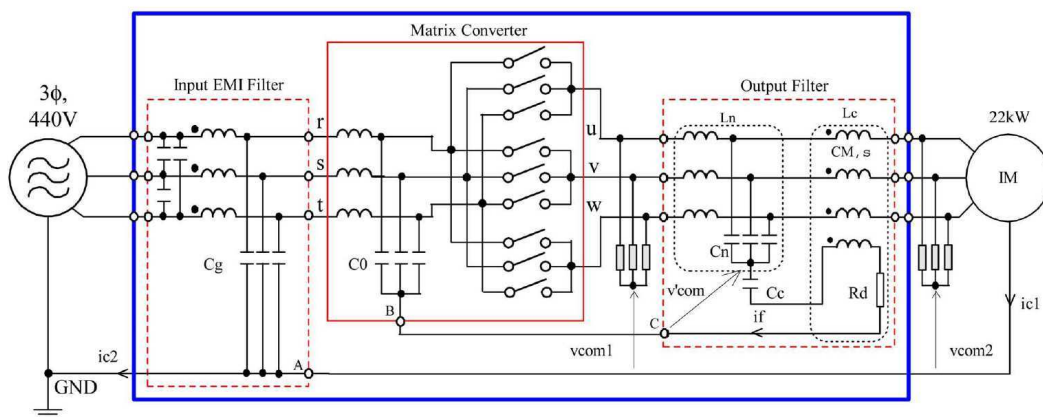


Figure 1.12: Proposed circuit by Yaskawa et al. [3]

the filters individually, and the parametrization is described with the guideline they have been using for the selection of the resonance frequency and the value of the components. There is also a description of the key role the parasitic components play at high frequency, hindering a good attenuation. Their proposed circuit is shown in Fig. 1.12, however there is no indication on which materials have been used for the inductors, nor is there an indication on how the filter has been realized or its dimensions. In addition the standard they are referring to is the CISPR-11[23], that has different requirements respect to the case of an airspace related application. Therefore the indications they provide can be used only for a general idea, they are not sufficient for an extensive study needed for this thesis.

1.6 Existing HF models

A good approach for a proper filter design implies first an accurate HF modelling and simulation for the whole system, to perform an initial decision on the filter required and afterwards an initial tuning of it, without the need of any practical work that is time and resource consuming. For this application, the HF parametrization started focusing on the motor, that is the device to be controlled. In the scientific literature various HF models for AC Induction Motors are present, with a range of analytical approaches [24, 25] and more practical approaches, as in [26], where a model has been developed (Fig. 1.13a) and then tuned to match existing measurements. Different models with more detailed information and guidelines for the tuning are provided in [4, 27, 28]. In particular this last model provides good accuracy in a wide frequency range. It consists of two coil-like networks in series to represent the part of the winding embedded in the stator's slots and the end windings respectively, together with the mutual coupling (Fig. 1.13b). To tune the model parameters values, a trial and error method has been used by the authors. The models in [26] and in [4] have been chosen as a starting point for the HF motor modelling; however, using this model, the matching of the experimental impedance measurements of the motor under test was not satisfying, despite the large number of attempts tried with the GA algorithms. Hence further investigation was necessary to find a suitable HF model for the motor of the experimental setup. Together with the motor HF model, cables and converter need a model too. For the cables the model will be created as in [29], starting from its geometrical dimensions. Regarding the converter model, no literature has so far appeared on HF modelling of Matrix converter, showing therefore the need of investigations in this direction. The converter model will be here derived starting from the impedance measurements too; since its power side consists only of IGBTs, its main characteristic is expected to be

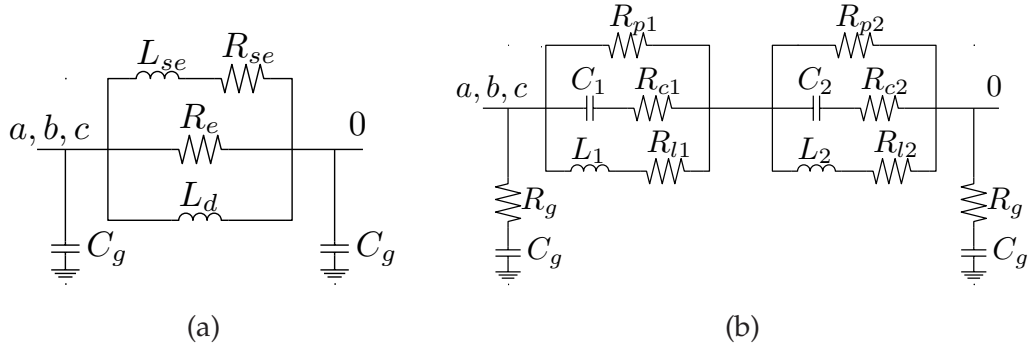


Figure 1.13: HF Motor models chosen for preliminary simulations.

just a stray capacitance due to the switches connected to the grounded heat-sink, the modelling task should be quite straightforward. The experimental impedance measurements, taken according to the needed configurations and provided in the next few chapters, will support this and will show the high accuracy matching obtained.

1.7 Aims and objectives

The aims of this work are to provide a guideline on how to set-up an EMI filter study and to design EMI filters, targeting especially matrix converters for aerospace applications. A description on the used methods to initiate the simulations, with some considerations on the simulation time, accuracy and portability of the controller's code within the simulation software needs to be addressed. The high frequency impedance measurements are also important to create a precise reference for all the various model-fitting process needed to produce the final model; special care must be placed in identifying the configurations for the measurement. These configurations will have to be targeted to measure the impedance of the parasitic current paths that need to be limited to fulfil the standard.

Another aim is to provide guidelines on how the EMI measurements will have to take place, with considerations on the probe calibration to minimize measurement errors and a summary with all the settings to be applied on the spectrum analyser for a proper reading.

The tools used for the HF modelling include a set of Genetic Algorithms, used to fit the models with actual impedance measurements, this process has been used to identify nearly every component because of its simplicity of use. Once the system have been parametrized and simulated, the filter design process can begin, with considerations on materials, dimensions and costs. EMI measurements with and without the filter will be needed to verify the attenuation obtained, and to prove that the converter satisfy the DO-160E standard [1] to be certified as a suitable Aircraft Equipment. Some

experimental tests at full power will be carried out, to demonstrate the functionality of the converter with the EMI filter fitted.

1.8 Structure of the thesis

Chapter 2 will deal with the experimental implementation of the matrix converter used for this work, starting with a description of the matrix converter concept, followed with the details of the components of the actual implementation and a description of the improvements made to the experimental setup. The chapter will conclude with some experimental measurements of the converter running at rated voltage.

Chapter 3 illustrates the high frequency modelling strategy adopted for the IM and the matrix converter, where the models' parameter identification is based on experimental impedance measurements and genetic algorithm optimization to fit the model's parameters to the data acquired.

Chapter 4 will provide the HF models for all the components of the experimental setup, starting with a description on the models existing in the literature, followed by further improvements needed to match the impedance measurements. Novel models for the motor, the converter and the cables will be suggested, to be included in a HF simulation to estimate the actual emissions.

Chapter 5 includes the drive system experimental emission measurements, starting with the requirements provided in the standard DO-160E, followed by directions on how to use the instruments and a procedure to calibrate current probes. The last section will group the drive's emissions, measured with such a procedure, that will need to be attenuated to satisfy the regulations.

Chapter 6 reports the performed simulations, with a brief introduction on how to include in the Saber Simulator the controller's code in its native language. A low frequency simulation, used to validate the model comparing the real output voltages with the simulated ones will be then explained, followed by the full characterization of the whole system at high frequency to estimate properly the emissions.

Chapter 7 will initially deal with the details of the output filter design starting with the identification of the required attenuation, then a simulation to validate the component's choice, and finally an HF modelling of the filter will be presented. It will conclude with the design of the input filter, that for time limitation has not been experimentally implemented.

Chapter 8 will report the experimental results obtained with the aforementioned out-

CHAPTER 1: INTRODUCTION

put filter added to the system, presenting comprehensive emission measurements for different operating conditions, to prove the satisfactory performance of the designed filter.

Experimental implementation of matrix converter drive

2.1 Introduction

This chapter starts with a general introduction on matrix converters, then goes more in detail with the hardware which has been chosen to design the EMI filter.

Section 2.3 describes the actual Matrix converter implementation shown in Fig. 2.5 with the pin-out of its input/output connectors. It also describes its new controller boards (Fig. 2.6) with some reference on how the sensing resistors have been designed, giving details about the motor used and a brief description of the control techniques and modulation used.

2.2 Introduction on Matrix converters

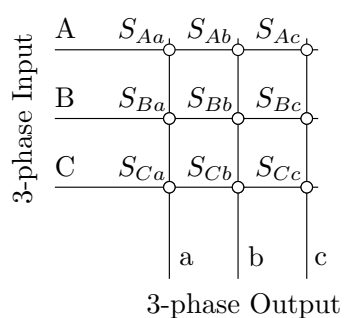


Figure 2.1: Matrix concept

The concept of a Matrix converter was first introduced in 1976 [30]. It is a direct AC/AC converter consisting only of bidirectional switches that connect each input phase to every output one. Because of the lack of the energy storage that others energy converters generally use, the instantaneous input and output power must be the same at any given moment.

Because of the nature of the switching devices, the power flow is bidirectional too so Matrix converters can, if needed, be used to regenerate power without any modification of the circuit, simply controlling in an appropriate way the switching times of the semiconductor

components. Furthermore this type of converter can provide intrinsically controllable power factor and allows lower switching losses [31] compared to traditional two-level inverters.

2.2.1 Modulation

Many modulation techniques have been proposed in the literature for matrix converter systems, but the two mostly used are SVM [32] and Venturini [33]. The latter is used in this research work. The basic mathematical solutions for the modulation strategy proposed by Venturini can be derived using the concept of switching function [34]. The idea starts from the general relationships between input and output voltage and currents, then can be represented as in (2.2.1):

$$\begin{aligned} \begin{bmatrix} v_a(t) \\ v_b(t) \\ v_c(t) \end{bmatrix} &= \begin{bmatrix} m_{Aa}(t) & m_{Ba}(t) & m_{Ca}(t) \\ m_{Ab}(t) & m_{Bb}(t) & m_{Cb}(t) \\ m_{Ac}(t) & m_{Bc}(t) & m_{Cc}(t) \end{bmatrix} \begin{bmatrix} v_A(t) \\ v_B(t) \\ v_C(t) \end{bmatrix} \\ \begin{bmatrix} i_A(t) \\ i_B(t) \\ i_C(t) \end{bmatrix} &= \begin{bmatrix} m_{Aa}(t) & m_{Ab}(t) & m_{Ac}(t) \\ m_{Ba}(t) & m_{Bb}(t) & m_{Bc}(t) \\ m_{Ca}(t) & m_{Cb}(t) & m_{Cc}(t) \end{bmatrix} \begin{bmatrix} i_a(t) \\ i_b(t) \\ i_c(t) \end{bmatrix} \end{aligned} \quad (2.2.1)$$

where $m_{ij}(t)$ are the modulation indexes. Taking for example the first switch, is so defined: $m_{Aa}(t) = t_{Aa}/T_{seq}$ where t_{Aa} refers to the on time for the switch between input phase "A" and output phase "a", and T_{seq} is the modulation period of the PWM. The matrices can be represented in a compact format such as:

$$\begin{aligned} [v_o(t)] &= [M(t)] [v_i(t)] \\ [i_i(t)] &= [M(t)]^T [i_o(t)] \end{aligned} \quad (2.2.2)$$

The desired outcome is usually to obtain a sinusoidal output voltage and a sinusoidal input current, therefore starting from a given input voltage and one output current as described:

$$\begin{aligned} [v_i(t)] &= V_i \begin{bmatrix} \cos(\omega_i t) \\ \cos(\omega_i t - 2\pi/3) \\ \cos(\omega_i t + 2\pi/3) \end{bmatrix} \\ [i_o(t)] &= I_o \begin{bmatrix} \cos(\omega_o t + \phi_o) \\ \cos(\omega_o t + \phi_o - 2\pi/3) \\ \cos(\omega_o t + \phi_o + 2\pi/3) \end{bmatrix} \end{aligned} \quad (2.2.3)$$

the modulation matrix $M(t)$ must produce the generic output:

$$\begin{aligned}
 [v_o(t)] &= qV_i \begin{bmatrix} \cos(\omega_o t) \\ \cos(\omega_o t - 2\pi/3) \\ \cos(\omega_o t + 2\pi/3) \end{bmatrix} \\
 [i_i(t)] &= q \frac{\cos(\omega_o)}{\cos(\omega_i)} I_o \begin{bmatrix} \cos(\omega_i t + \phi_i) \\ \cos(\omega_i t + \phi_i - 2\pi/3) \\ \cos(\omega_i t + \phi_i + 2\pi/3) \end{bmatrix}
 \end{aligned} \tag{2.2.4}$$

In these formulae q is the voltage ratio, ω_i and ω_o are the input and output angular frequencies and ϕ_i and ϕ_o are the input and output displacement angles. Venturini derived two solutions, the first one is under the assumption that $\phi_i = \phi_o$ and the second one that $\phi_i = -\phi_o$:

$$\begin{aligned}
 M1(t) &= \frac{1}{3} \begin{bmatrix} 1 + 2q \cos(\omega_m t) & 1 + 2q \cos(\omega_m t - 2\pi/3) & 1 + 2q \cos(\omega_m t + 2\pi/3) \\ 1 + 2q \cos(\omega_m t + 2\pi/3) & 1 + 2q \cos(\omega_m t) & 1 + 2q \cos(\omega_m t - 2\pi/3) \\ 1 + 2q \cos(\omega_m t - 2\pi/3) & 1 + 2q \cos(\omega_m t + 2\pi/3) & 1 + 2q \cos(\omega_m t) \end{bmatrix} \\
 &\text{with } \omega_m = (\omega_o - \omega_i)
 \end{aligned} \tag{2.2.5}$$

$$\begin{aligned}
 M2(t) &= \frac{1}{3} \begin{bmatrix} 1 + 2q \cos(\omega_m t) & 1 + 2q \cos(\omega_m t - 2\pi/3) & 1 + 2q \cos(\omega_m t + 2\pi/3) \\ 1 + 2q \cos(\omega_m t - 2\pi/3) & 1 + 2q \cos(\omega_m t + 2\pi/3) & 1 + 2q \cos(\omega_m t) \\ 1 + 2q \cos(\omega_m t + 2\pi/3) & 1 + 2q \cos(\omega_m t) & 1 + 2q \cos(\omega_m t - 2\pi/3) \end{bmatrix} \\
 &\text{with } \omega_m = -(\omega_o - \omega_i)
 \end{aligned} \tag{2.2.6}$$

The combination of these two solution will provide the control over the input displacement factor in a way that

$$\begin{aligned}
 M(t) &= \alpha_1 \cdot M1(t) + \alpha_2 \cdot M2(t) \\
 &\text{where } \alpha_1 + \alpha_2 = 1
 \end{aligned} \tag{2.2.7}$$

Setting $\alpha_1 = \alpha_2$ will provide unitary input displacement, no matter which is the load displacement factor. Otherwise, changing this ratio will provide a means to control the input displacement to have a lagging or leading factor, however for this case the load displacement factor must be known. Opting for the unitary displacement condition, the modulation functions can be simplified in a compact formula:

$$\begin{aligned}
 m_{Kj} &= \frac{t_{Kj}}{T_{seq}} = \frac{1}{3} \left[1 + \frac{2v_K v_j}{V_i^2} \right] \\
 &\text{for } K = A, B, C \text{ and } j = a, b, c
 \end{aligned} \tag{2.2.8}$$

This solution allows a maximum modulation index q of 50%, visible in the top of Fig. 2.3a, representing the case of a standard three phase 50Hz input supply while the output is set to be at 100Hz. Further work, carried out by Venturini and Alesina, improved

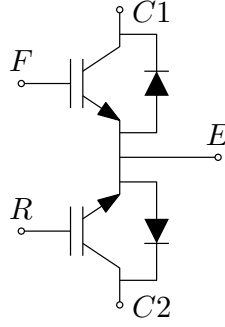


Figure 2.2: IGBT module used

this limit to a maximum of 86.6% by means of an injection to the common mode voltage of the third harmonic [35]. This way the lobes of the input voltage envelope could be fully used, as in Fig. 2.3b to generate the maximum output available for a given input voltage, that corresponds to $\sqrt{3}/2$ of the input.

The new output target voltage becomes:

$$[v_o(t)] = qV_i \begin{bmatrix} \cos(\omega_o t) - \frac{1}{6} \cos(3\omega_o t) + \frac{1}{2\sqrt{3}} \cos(3\omega_i t) \\ \cos(\omega_o t - 2\pi/3) - \frac{1}{6} \cos(3\omega_o t) + \frac{1}{2\sqrt{3}} \cos(3\omega_i t) \\ \cos(\omega_o t + 2\pi/3) - \frac{1}{6} \cos(3\omega_o t) + \frac{1}{2\sqrt{3}} \cos(3\omega_i t) \end{bmatrix} \quad (2.2.9)$$

The new solution for the modulation indexes in formula 2.2.8 now becomes, in a compact representation:

$$m_{Kj} = \frac{1}{3} \left[1 + \frac{2v_K v_j}{V_i^2} + \frac{4q}{3\sqrt{3}} \sin(\omega_i t + \beta_K) \sin(3\omega_i t) \right] \quad (2.2.10)$$

for $K = A, B, C$ and $j = a, b, c$ with $\beta_K = 0, 2\pi/3, 4\pi/3$ for $K = A, B, C$ respectively

This is the formula implemented in the control algorithm that, starting from the modulation index q and the output angular frequency given by the V/f control in Fig. 2.9, will generate the nine modulating indexes m_{ij} fed to the nine PWM generators inside the FPGA. The output of each of these channels has a hardware state machine that, accordingly to the output current, will autonomously generate the correct timing for the four-step commutation, without the need of overloading the control code to control individually each of the 18 switches (2×9 unidirectional switches, as in Fig. 2.2).

2.2.2 Commutation strategies

A general 3×3 three-phase Matrix converter system is composed of 9 switches, S_{Aa} to S_{Cc} as in Fig. 2.1. This direct connection from input to output limits the possibility of

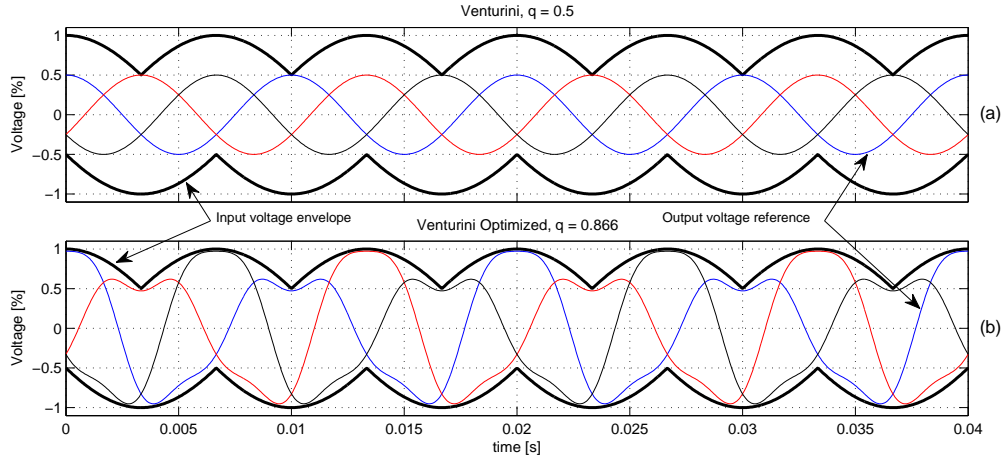


Figure 2.3: Output voltage comparison for modulation techniques

the input and the output to be of different nature: it should not have inductors both at the input and output (imposed current) or capacitors (imposed voltage). Failing this condition, the switch will have to close across two different sources of voltage or currents, driven on each side at different values; this is an unacceptable condition that will most probably cause the failure of the device. Assuming to have a motor as a load, because of its inductive nature, every output must be connected to an input at any given time, to prevent current transients.

Usually the chosen devices for the switches are IGBT because of their current capabilities, however these devices are intrinsically unidirectional, thus every switch in Fig. 2.1 actually consists of two devices connected in anti-parallel, in common collector or, more often, common emitter configuration. Taking this into account and considering the finite amount of time needed for a semiconductor to change state, it is clear that to change configuration of the switches a special sequence must be introduced, to overcome these problems [36][37]. To do so three commutation techniques have been introduced: 2 step, 3 step or 4 step commutations. The two step commutation technique simply uses a single dead time between the switching off of a transistor and the switching on of the other one, leaving to the clamp circuit the task of dealing with the over-voltages generated when there is no path for the current. The four step commutation sequence is represented in Fig. 2.4, where each switch adopts the common emitter configuration; the IGBT that creates a path for the current to flow from the source to the load will be called forward IGBT and the one that allows the current to go from the load to the source will be called reverse IGBT. This sequence implies a first step with the switching off of the reverse IGBT (1); to control the appropriate IGBT the current's direction can be sensed and fed to the control. The second step will close the forward

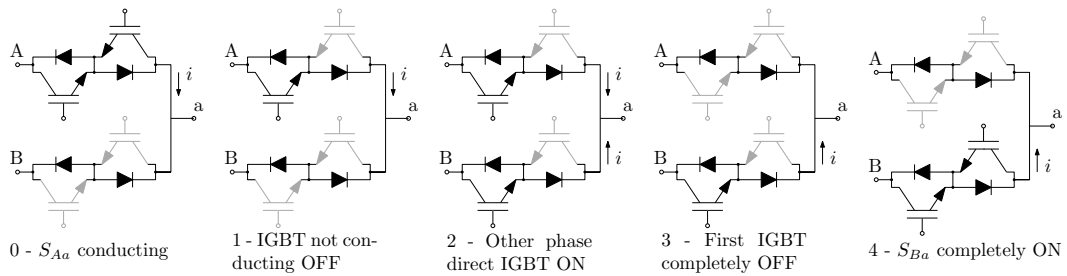


Figure 2.4: 4 step commutation sequence

IGBT in the switch to be turned on (2), creating a parallel path for the current to the load; to be noted that, because both reverse IGBT are off, there is no path for any phase to phase current. Then the first IGBT is completely switched off and the current flows only from the second phase (3), and finally the second switch is completely switched on with the closure of the reverse IGBT (4). It is clear that this technique, compared to a standard inverter, needs some extra components to sense the current's direction to control properly the gate signals, however this will allow lower commutation losses because half of the commutations will be at zero current (soft switching). The three step commutation is just a particular case of the 4 step one, where the two middle commutations are triggered at the same time, this is justified by the fact that a semiconductor is faster to switch off rather than to switch on.

2.3 Matrix converter chosen for the experimental tests

The converter used for this study is a compact Matrix Converter designed at Nottingham University by Dr. James Campbell Fig. 2.5. It features nine 60A four-quadrant IGBT modules SK60GM123[38], all connected to a six layer PCB board. Additionally, on the inputs, there are three line to line filter capacitors of $2\mu\text{F}$ and a diode rectifier for the clamp circuit and, on the outputs, there is another rectifier connected always to the same clamp.

This last component, the clamp circuit (Fig. 2.7) is composed of two capacitors of $150\mu\text{F}$, 450V in series, each one having a $47\text{k}\Omega$ resistor in parallel. It is necessary to deal with the currents when the modulation is not precise enough (e.g. if there are small periods with all the IGBTs off during the switching sequence) and, more importantly, to collect the magnetic energy stored into the machine when the converter is switched off: at this time all the switches will go off at once so, without this network, the load current would have no path to follow generating high voltage spike at the motor terminals that would definitely damage the converter. On the output there are



Figure 2.5: Matrix converter used

three circuits with a digital output to sense the direction of the output current (needed for the four step commutation sequence), three LEM LAH 25-NP current sensors[39] and three LEM LV-25-P voltage sensors[40], one of the latter ones is used for the clamp circuit, to detect whether there is an over-voltage on the clamp capacitors. The board needs two different supplies, +5V for the logic and the gate drives and a dual supply $\pm 15V$ for the current and voltage transducers. The control signals for the IGBT are grouped in a 26-pin header, located at the center top of the converter, their function is described in Table 2.1. Their numbers reflect the one on the PCB design, and the connector's key shroud corresponds to the table's left hand side. The signal's names are defined this way: the number in the signal name specifies on which input phase the IGBT terminal C1 is connected to, 1,2 and 3 represent phases R,S and T. An F (forward) or an R (reverse) specify which of the two IGBT within the module (Fig. 2.2), then the last character is to specify which of the output phases the IGBT terminal C2 is

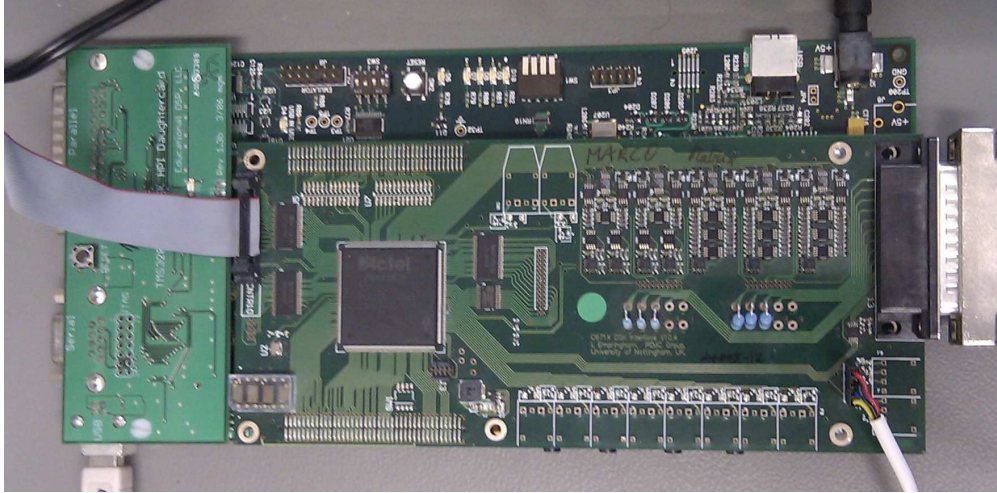


Figure 2.6: New control boards

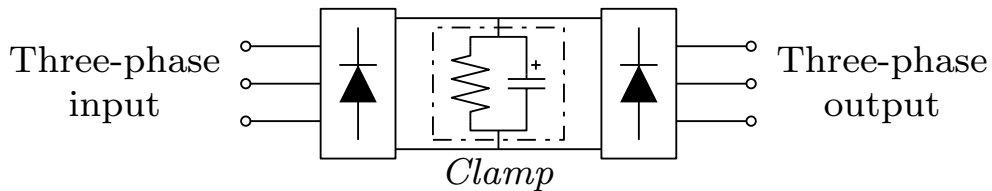


Figure 2.7: Clamp circuit schematic

connected to: A, B or C that correspond to the output phases U, V and W as they are named on the PCB.

The orange 4-way connector at the bottom of Fig. 2.5 is the input for the 2 voltage transducers; it has been used to sense the line to line voltage for the phases RS and ST. The last connector, visible on the bottom left always in Fig. 2.5, one carries the analog signals, described in Table 2.2. It collects the outputs for the current and voltage transducers, and is meant to be connected to six of the 12 bit analog-to-digital converter (A2D) present on the controller board.

2.3.1 Hardware improvements

Because the converter had previously been used, its hardware had to be thoroughly checked before energizing it. Only a small problem has been detected: the digital signal about the output current's direction on phase W was not working properly, this was due to the sensing circuit: the ground reference at the pin 5 of the optocoupler was missing. Once the problem has been identified, it has been solved by soldering a small wire from the closest ground directly on the pin. A minor upgrade was applied removing an analog comparator formerly used to manually set the trip for the clamp

over-voltage, wiring the voltage transducer's output directly to the 9-way connector for the analog signals. This allowed a more flexible control on the trip threshold directly on the FPGA board with one of its hardware trips, that can be adjusted digitally within the code. This modification allowed also a continuous monitoring of the clamp voltage through one of the analog-to-digital converters on the FPGA board, and the possibility to display this value on the new FPGA's display.

2	Q3FC	1	Gnd
4	Gnd	3	Q2FC
6	Q1FC	5	Q2RA
8	Q3RA	7	Q2RB
10	Q3RC	9	Q2RC
12	Q3RB	11	Q3FB
14	Gnd	13	Q2FB
16	DirA	15	Q1FB
18	DirB	17	Q1RC
20	DirC	19	Q1RA
22	Q3FA	21	Q1RB
24	Gnd	23	Q2FA
26	Q1FA	25	Gnd

Table 2.1: Pin-Out of Matrix control signal

1	Gnd
2	I_{outA}
3	I_{outB}
4	I_{outC}
5	NC
6	V_{Clamp}
7	V_{ST}
8	V_{RS}
9	NC

Table 2.2: Pin-Out of Matrix analog signals

2.4 Controller boards

The original control boards for this converter were missing, so new ones have been purchased: a Texas Instruments TMS320C6713 DSK fitted with the Actel FPGA A3P400 based board and the daughter card LLC Educational Fig. 2.6; these are the current work horses used for nearly every project in the PEMC group at the University of Nottingham. The DSP features a 225MHz core, 32MB of dynamic ram used to store data to be transferred via the host interface and a 32bit wide external memory interface used to communicate with the FPGA. The used flash-based FPGA has 400k System gates, 9k flip-flops, 54 Kb RAM and a maximum of 151 I/O pins. The board, designed by Dr. Lee Empringham, has a 50MHz crystal, whose frequency is used for the three state machines that generate the switching signals. The DSP and the FPGA boards work in a symbiosis that acts as follows: the FPGA is set to generate an interrupt on the DSP

at the desired switching frequency; this signals also triggeres the conversion of the 10 Analog to Digital (A2D) converters fitted on the FPGA board. Once the conversion is finished the DSP reads the data from the FPGA, it processes it within the control algorithm chosen to generate the modulation timing for the next step, then it loads this times inside the FPGA's PWM generators. This mechanism may seem awkward, but it has been chosen for its level of abstraction: actually the FPGA is "invisible" to the programmer; once it has been programmed with the appropriate firmware it acts simply as an external memory where the DSP reads and writes some data. This way, for simple applications, there is no need of any detailed knowledge about FPGA, nor about VHDL programming. Within the Nottingham PEMC group there are some standard "packets" with the FPGA code just to be programmed and a basic C algorithm for the DSP that has only to be loaded, in this way reducing the development time and time to get to know the control boards. However, some VHDL code has been written to improve the communication with the display, the digital resistors that sets the trip levels and the Digital to analog converter. The modules thus created allow faster transfer data to print values on the display in real time plus, with the 8 bit, 4 channel digital-to-analog converter (D2A) present on the PCB, a real time debugger can be used to "spy" on any desired variable in the code.

2.5 Measurement transducers

In order to use the A2D converters present on the board, the sensing resistors needed to be designed; they have to transform the current signal coming from the LEM transducers into voltage signals for the conversion. This calculation is quite straightforward, once the desired range of measurement is determined, and the following two sections explain how to do it.

Voltage transducers

The maximum voltage that can be read by the voltage transducers is set by the resistors on the high voltage side, already fitted on the PCB: $47\text{k}\Omega$ high power thick film resistor. From the data-sheet of the voltage transducer LV-25-P, remaining within its nominal primary current value, will allow to measure $\pm 14\text{mA}$ or $\pm 658\text{V}$, that is a suitable value for the purposes of this study, hence no need to replace them. Consequently to the 25:10 conversion ratio, the induced secondary current will be of 35mA . Because the

A2D converter input must be in the $\pm 5V$ range, the maximum resistor needed will be:

$$R_{max} = \frac{V_{max}}{I_{max}} = \frac{5}{0.035} \simeq 140\Omega$$

A further check is needed for the resistor's power rating, in the worst case scenario. For the resistors at the primary the power is calculated in the following way:

$$P = \frac{V^2}{R} = \frac{658^2}{47000} = 9.2W < 10W_{rated}$$

For the secondary:

$$P = \frac{V^2}{R} = \frac{5^2}{140} = 0.18W < 0.6W_{rated}$$

Current transducers

The current transducers are LEM LAH 25-NP which have three terminals that can be connected in series for better accuracy or in parallel to measure the higher currents, accordingly to the application. The PCB connects all three of them in parallel, implying a maximum rated current of 55A. This value is quite high, so it has been chosen to design the sense resistor to be able to measure properly up to a maximum current of $40A_{peak}$, to obtain more accuracy for lower readings. The transducer's conversion ratio is 1:1000, so 40A will be translated in 40mA at the secondary. For the resistor design Ohm's law has again been used:

$$R_{min} = \frac{V_{max}}{I_{max}} = \frac{5}{0.04} \simeq 130\Omega$$

The usual check for the power confirms that the chosen resistor is suitable:

$$P = \frac{V^2}{R} = \frac{5^2}{130} = 0.192W < 0.5W_{rated}$$

2.6 Motor drive and control technique

The motor used to build the matrix converter drive is a 1.5kW **Brook Hansen** asynchronous motor (type W-DA90LK) star connected, that has been supplied by the converter output. For the purpose of this thesis there are no requirements on the control nor on the modulation, therefore a simple V/f control technique (Fig. 2.8) has been used; the control has only to accelerate the motor generating a sinusoidal output voltage of increasing frequency from 0Hz up to the final value of 100Hz, and then to maintain it. This is an open loop control, where no feedback about the motor position or speed is used.

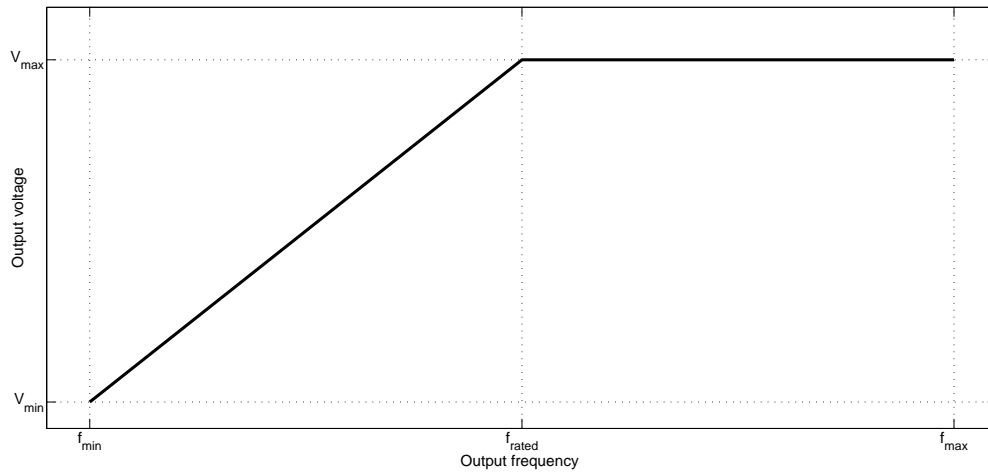


Figure 2.8: V/f control technique

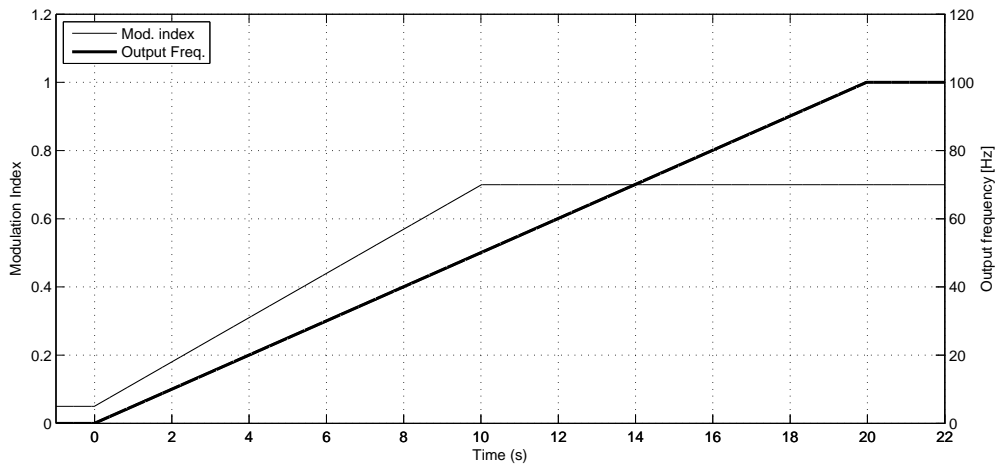


Figure 2.9: V/f implementation

To allow this an internal voltage reference has been created within the control code. To control the voltage, the modulation index is slowly increased from 5% to the final value of 70%, this happens during the first 10 seconds. The output frequency, instead, linearly increases from 0 to 100Hz in the first 20 seconds. Fig. 2.9 shows the representation of the speed and the modulation index during a run of the converter. The modulation technique used is the Venturini optimized that allows, injecting a third harmonic, to reach up to a maximum modulation index of 86.6%, rather than the 50% available with the basic Venturini (Fig. 2.3b).

2.7 Experimental test at full voltage

The converter was at the maximum voltage before starting the EMI measurements. The run test, visible in in Fig. 2.10, has been done supplying the converter at $240V_{rms}$ and 50Hz with a variable power supply, while it was driving the chosen motor at $170V_{rms}$ and 100Hz. The motor had no load connected on the shaft: the mechanical torque was only due to the friction and the cooling fan, and this explains why the output current is just below 1A. Again, there were no particular indications for the experimental setup, so that particular output frequency has been chosen just to be different from the input supply. Because the application of this work is for aerospace, the actual supply will be at $115V_{rms}$ and 400Hz. This condition has been tested too, but having a lower input voltage will lead to a lower output current, showing that the former case was the more demanding in terms of power, thus more indicative to prove the stability of the system.

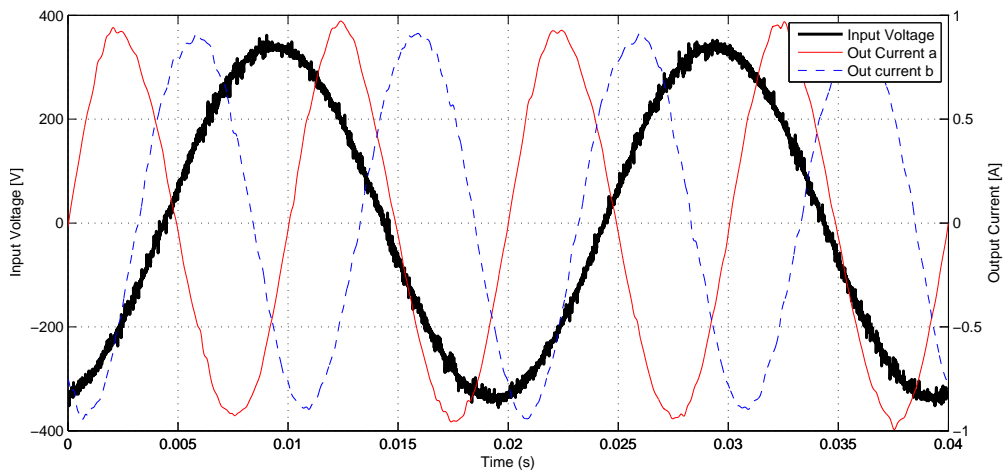


Figure 2.10: Measurement at full voltage

HF Modelling Strategy

3.1 Introduction

In literature some works have been presented with the aim to reduce EMI emission on inverter driven motors, some of which use a Finite Elements (FE) analysis approach to fully understand the stray components and so the current paths, as in [41]. Such FE simulations can provide a very accurate result, but they are time consuming and they are very specific for the chosen system. This will hinder a fast design for the EMI filter and will largely reduce the portability of the model eventually created. For these reasons the FE approach has been considered not of interest in this work, instead modelling and parametrization using experimental impedance measurements has been chosen in this thesis. This chapter describes the high frequency modelling strategy proposed, based on automated impedance measurements matching; however without going into details of the HF models yet. The experimental impedance measurement techniques used and how the measurements have been chosen will be firstly described. Then a brief introduction on the Genetic Algorithms, used to identify the model's parameters to match the experimental measurements, together with a description of the fitness function that weights how the results are close to the reference values provided, is given. A discussion on the way the HF impedance simulations have been carried out, trying to optimize the calculation time and still providing a good flexibility if some changes in the model are needed.

3.2 Impedance measurements

During the HF filter design process an accurate HF model is needed for the whole system. In order to do so, in this thesis, the starting point for the HF modelling is the actual

impedance measurement of every single component of the drive, along the frequencies of interest. To obtain these values an Impedance Analyzer (HP4194A with a 41941-61001 probe) has been used. It provides reliable measurements in the range 10kHz – 100MHz, of which we are interested only in the first 30MHz because the Conducted Emission specifications in [1] apply only in this range. This instrument can perform linear or logarithmic sweeps in the specified range of frequencies, storing internally up to 401 points of the measured complex impedance. The instrument also features an HP interface bus, interconnected with a pc to allow the download of the stored data. When the measurement has taken place, a *LabVIEW* program was used to read the internal registers and save them into an excel file, to be imported into the Matlab's environment for use as a reference during the HF modelling. This whole process is very straightforward and does not take long; it is a much faster approach than a Finite Element study that would have to be carried out on every component; even though the latter will be more accurate. This lack of high precision is unavoidable with this system, besides, it is a necessary trade-off in order to obtain results good enough for a quick start of the EMI filter design.

Configurations of measurements done

To characterize the whole system, every single component has to be measured; in more detail there is the AC motor, the matrix converter, the cables and the Line Impedance Stabilization Network (LISN). This latter component becomes part of the circuit because it must be used during the emissions measurements, as it is described by the reference standard [1], to provide a nominal line impedance no matter which voltage source is in use. The impedance measurement configurations have to match the emissions to be reduced, in more detail we need common and differential mode measurements. Starting with the motor, for the common mode all the input terminals need to be shorted together, and the impedance measured between this point and the ground. For the differential mode, instead, the measure needs to take place among one terminal and the others 2 shorted, leaving the ground connection floating.

Some considerations need to be made, because of the high frequency in play: over the last part of the interest range, 10 – 30MHz the parasitics play a dominant role in the impedance, and all the capacitive coupling will come into play dominating the impedance's behaviour. Therefore if, for the measurements, any external wire has been used, its impedance needs to be measured on its own and afterwards subtracted from the global measurement to get only the data of interest. For the measurements, wherever possible, all the data has been taken using no extra wires, to avoid the differences

that will be caused by the layout of the externals paths, that is another important factor for the measurements in high frequency. Regarding the matrix converter, the input filter capacitors have been unassembled and measured separately, then the input and output CM and DM impedances were measured independently, using a short wire to join all the three terminals plus one to bypass the output diodes that sense the output current direction. For the cable no measurements were needed because it was modelled considering just its geometrical parameters, using the formulae and the model given in [29]. The last component is the LISN, where its equivalent circuit with all the relative parameters is provided on its manual. The next chapter will deal with these two components in more detail.

Summarizing, the set of measurements needed for the aforementioned approach are:

- CM of the AC motor - *Measurement taken between the motor's terminals a+b+c shorted and the ground terminal*
- DM of the AC motor - *Measurement taken between terminal a and terminals b+c shorted*
- CM of the Matrix converter's input - *Measurement taken between the converter's terminals a+b+c and the ground one, after removing the input capacitors*
- DM of the Matrix converter's input - *Measurement taken between the converter's terminal a and the b+c ones, after removing the input capacitors*
- CM of the Matrix converter's output - *Measurement taken between the converter's terminals u+v+w and the ground one, after shorting the sense output diodes*
- DM of the Matrix converter's output - *Measurement taken between the converter's terminal u and the v+w ones, after shorting the sense output diodes*
- Input capacitors of the matrix converter - *Impedance to be added across the inputs of the converter*

3.3 Genetic Algorithms and their use for structural identification

For this work various models have been tested to see if they could fit adequately the measured impedance of each part of the system. Each one has different basic electrical components, the value of which had to be varied in order to match, with the whole

circuit, the reference impedance, experimentally measured. A method was therefore needed to regulate this value adapting sequence, in order to reach the matching in a reasonable amount of time and without the need to try every possible combination. This task identifies exactly what genetic algorithms do: they start with a set of random chosen values, and adapt continuously this set in order to reach the desired goal. If the model's impedance, at the end of the optimization, will be too different for the reference, it will show that the used model is not suitable and it should be improved or replaced.

The genetic algorithm [42, 43] uses the principles of natural selection and genetics from natural biological systems, in a computer algorithm, to simulate evolution. Essentially the GA is an optimization technique that performs a parallel, stochastic, but direct search that evaluates more than one area of the search space and can discover more than one solution to a problem. A "fitness function" measures the fitness of an individual (possible solution) to survive in a population of individuals. The genetic algorithm will seek the solution that minimizes the fitness function, generating at each step a new generation of solutions using the operations of mutation and crossover and selecting the best individuals for the population at the following step.

At initialization a specified number of individuals and generations are chosen with the first population of individuals being generated randomly. The individuals are then tested and a fitness value is associated to each one of them. Through the genetic operation of selection the individuals with the higher fitness value will have a higher probability to be selected in the population at the following step. Once the selection procedure has terminated, the genetic operations of mutation and crossover are used to create the new generation of individuals starting from the selected individuals. Once the new generation is created, each individual is again tested and the whole procedure is iterated. The algorithm will update the best individual at each generation. The search procedure will terminate when a fixed termination criteria (maximum number of generations or a target error) is fulfilled.

Original software has been developed within the Matlab[®] environment, which uses Genetic Algorithms to automatically tune the parameters of the HF model in a simulation to match specific experimental impedance measurements. The user can set, in appropriate fields, bounds for the parameter values and probability of mutation and crossover. It has been preferred not to use the built in GA toolbox of Matlab because it does not guarantee versatility and the possibility of a full control of every algorithm setting

All the information about the circuit parameters are coded into a string. Each of these strings, therefore, represents an individual, i.e. a possible solution for the optimization

Parameter	Value
Generation gap	0.9
Crossover rate	0.88
Mutation rate	0.36
Insertion rate	0.8
Number of individuals	150
Number of generations	60

Table 3.1: Used parameters for Genetic Algorithms

problem. At the initialization, a specified number of individuals and generations are chosen, and the first population of individuals is generated randomly. At time k , the genetic operations of mutation and crossover are used to create the new generation of individuals starting from the selected individuals at the previous time $k-1$. In the optimization, the program will recursively calculate the model's impedance versus the frequency, evaluating each of the individuals in the current population.

Using the simulation results, a fitness value will be associated to all the individuals, proportionally to the difference between the simulated impedance and the reference one. Through the genetic operation of selection the individuals with the higher fitness value will have a higher probability to be selected in the population at the following step. Only the "most fit" individuals evolve to the next generation at time $k+1$. The algorithm will update at each step the best individual. The search procedure will terminate when the fixed target error or a maximum number of generations is reached. The final output of the procedure will be an optimum set of parameters with minimized fitness function.

The fitness function is based on the error between the measured impedance of the system and the respective calculation with the current parameters based on the individual. Usually more attempts are needed to find an optimum solution since the system can converge to local minima. However, with genetic algorithms, this happens less frequently than with other optimization strategies. In fact the GA provides a stochastic optimization method where if it "gets stuck" at a local optimum, it tries to simultaneously find other parts of the search space and "jump out" of the local optimum, aiming at a global one.

The used parameters for the individuals generation are grouped in Table 3.1, and occasionally only the number of generation and individuals per generation were changed, if the found solution wasn't close enough to the desired goal.

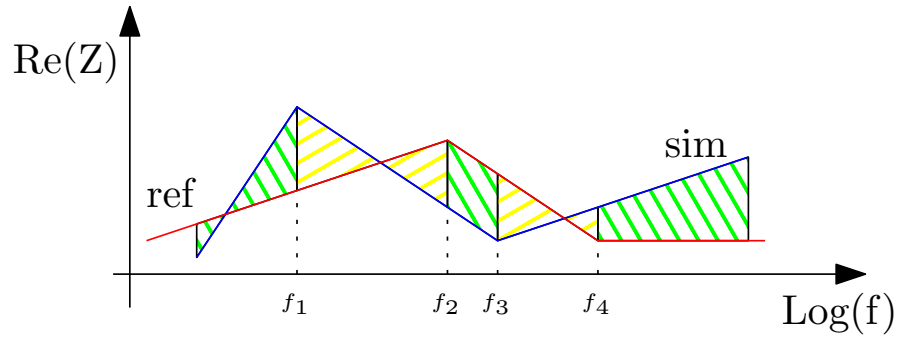


Figure 3.1: Example of error integration for impedance

Fitness Function

The goodness of every individual is evaluated by the Fitness Function that associates a numerical value to each of them; this function is the way to map how far each individual is from the desired goal. It can weight in different ways many aspects of the final result, i.e. giving more importance to solutions generating a better match in a certain range of frequencies or penalizing more the individuals that do not produce a desired characteristic, such as a resonating frequency if the goal is to match an impedance with that behaviour.

The Fitness Function used for the impedance matching in this work consists of the integral of the error between the measured reference impedance versus the frequency and the relative simulated one with the parameters chosen by the GA, this is visually represented by the area between the reference and the simulated impedance. Because the impedance is a complex number, this area is calculated twice, once for the real and once for the imaginary part, these two numbers are successively added to get the final error. Fig. 3.1 shows the area so calculated, in this case just for the real part of the impedance. The reference and the simulated impedance points might not be sampled at the same frequency, so a process of interpolation takes place and subdivide the series of data at all the vertex of either of the two curves, to obtain eventually two set of values sampled at the same frequencies. In this example the algorithm for the error integration calculates the total area given by the five subsections shown in alternate colors and patterns, every area can only be either a trapezium (third and fifth case) or the double opposite triangle (first, second and fourth case); this is because it is defined by 4 segments, two of which have to be parallel, representing the frequency subdivision in the impedances, that have been adjusted to be the same. To distinguish between the two cases and pick the right formula, the algorithm simply checks if the reference and the simulated impedance values cross each other or not.

Calling Δ_A and Δ_B the differences of impedance at any two contiguous frequencies, and because the frequency is represented on a logarithmic scale to properly weight low and high frequencies, depending on the case the formula to calculate the area is given by:

$$A_{Triangles} = \frac{(\Delta_A^2 + \Delta_B^2) \cdot (\log_{10}(f_2) - \log_{10}(f_1))}{2 \cdot (\Delta_A + \Delta_B)} \quad (3.3.1)$$

$$A_{Trapezium} = \frac{(\Delta_A + \Delta_B) \cdot (\log_{10}(f_3) - \log_{10}(f_2))}{2} \quad (3.3.2)$$

The first formula has been obtained with some simple geometry: Fig. 3.2 represents

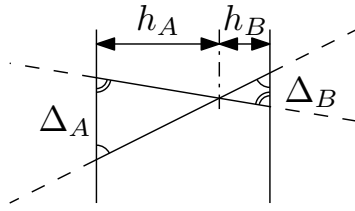


Figure 3.2: Explanation of area calculation for double triangle case

the case of the two triangles. The two vertical lines are parallel because it's the frequency on the impedance measurement, the other two lines are the impedance profile. The two triangles formed are similar because they have the three angles equals (using the property of parallel lines cut by a transversal), so we can apply the following equation:

$$\Delta_A : h_A = \Delta_B : h_B \quad (3.3.3)$$

and from that we can obtain:

$$h_A = \frac{\Delta_A \cdot h_B}{\Delta_B} \quad \text{and} \quad h_B = \frac{\Delta_B \cdot h_A}{\Delta_A} \quad (3.3.4)$$

Also, the sum of the two heights is equal to the logarithmic frequency step:

$$\log_{10}(f_2) - \log_{10}(f_1) = h = h_A + h_B \quad (3.3.5)$$

combing this equation with the previous ones:

$$\begin{aligned} h &= \frac{\Delta_A \cdot h_B}{\Delta_B} + h_B \Rightarrow h_B = \frac{\Delta_B \cdot h}{\Delta_A + \Delta_B} \\ h &= h_A + \frac{\Delta_B \cdot h_A}{\Delta_A} \Rightarrow h_A = \frac{\Delta_A \cdot h}{\Delta_A + \Delta_B} \end{aligned} \quad (3.3.6)$$

The sum of the two areas will be: $\Delta_A \cdot h_A + \Delta_B \cdot h_B$ that becomes:

$$\frac{\Delta_A^2 \cdot h}{\Delta_A + \Delta_B} + \frac{\Delta_B^2 \cdot h}{\Delta_A + \Delta_B} \quad (3.3.7)$$

Thus proving Eqn. 3.3.1.

Defining the bounds for the fitting

A key role for the optimization process is played by the bounds given to each parameter so that they can be selected within reasonable limits. This will facilitate the optimization's convergence, saving computational time, plus it will hinder the process being trapped in local minima. On the other hand, too narrow limits can lead to wrong solutions being selected, above all where the final values are saturated toward the chosen boundaries. Unfortunately there is no general rule on how to determine the boundary values, even so a great role is played by experience when, according to the topology, there is already an idea of the range of the various components of the model. An example could be if capacitors have to be modelled, it is expected that the main capacitance will be close to the nominal value and the associated series resistance will be low.

To find the range for the HF parameters values in the motor model optimization, given the number of parameters to be selected, some initial runs of GA have been launched with wide bounds, and then this range has been narrowed around the more recurrent values.

3.4 HF model simulations

A key point for the HF impedance simulation combined with the GA is the computational speed and the versatility of the model to be quickly modified if needed. The first approach used was to iteratively run a circuit Saber simulation within the Matlab GA script, where the value of every component, for each iteration, was passed to the Saber simulator. This approach implied an understanding of how to externally execute a series of repetitive steps with the Synopsys tools: launch Saber Simulator, run a script to alter the component's values, execute the frequency analysis, close the simulator and open the Cosmoscope to import the results, export them into a file and eventually import these results into Matlab's Workspace for the error calculation. This approach was very powerful due to the interface with a proper circuit simulator; the problem, however, was the time needed to execute all of those steps that could not allow more than a few simulations per minute. Because the GA needs hundred or possibly thousands of iterations, it is clear that this method was not suitable and needed to be changed. To fully take advantage of Matlab's speed in handling matrices, a set of the state space equations for the HF motor model has been extrapolated; this approach provided the fastest computational speed, but was very poor in terms of versatility of the model. With this approach, for every configuration, a different set of equations had to be calculated again for common and differential mode plus one for the parasitic measurement.

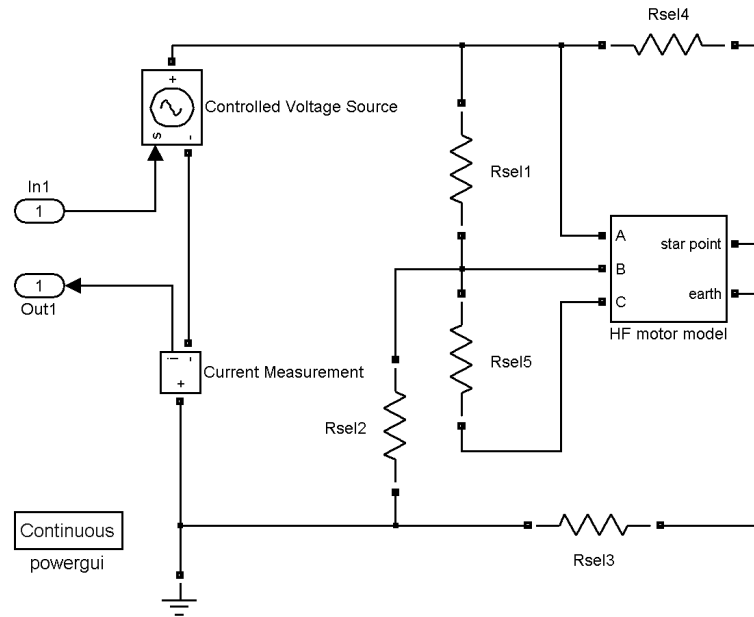


Figure 3.3: HF Motor model in Simulink with topology toggling resistors

It is clear that it will take quite some time when the number of variables is more than 10, as in the case of the HF model of an induction motor. Furthermore, in the case that a different circuit topology needs to be considered, the equations need to be re-written all over again even if just a single component has to be added or removed.

A good compromise solution finally adopted was to use the Simulink tool PowerSim to implement the HF circuit and, rather than recalling iteratively the simulink circuit simulations, the `linmod` command has been used in the GA script. This method produces the state space matrices of the network between an input and an output port. Therefore adding to this network a voltage controlled source as input and measuring a current as an output, and eventually using Ohm's law, will generate exactly the required transfer function that represents the impedance of a function of frequency (Fig. 3.3). So, providing that the HF circuit model is in a simulink file, the following three lines of code will implement the procedure previously described:

```
[A,B,C,D] = linmod(ModelName);
statespace = ss(A, B, C, D);
[ mag,phase,freq ] = bode(1/tf(statespace),Fref(:,1)*pi*2);
```

Here the `ss` function initializes the "statespace" variable with the state-space model obtained from the four matrices and the `tf` function transforms again this model into a transfer-function one. This latter model, together with the frequency reference "Fref", is eventually passed to the `bode` function giving three vectors as results: magnitude and phase of the impedance and a vector with the values of frequency for each of the

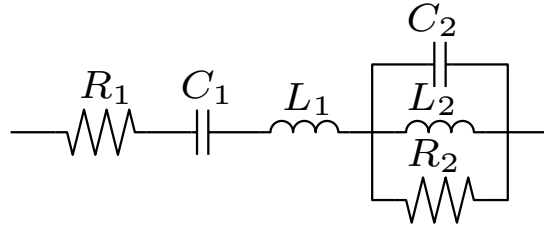


Figure 3.4: Matrix converter input capacitor equivalent network

impedance values according to the chosen resolution.

To fit multiple types of impedance measurements using the same circuit model an elegant solution has been used to change the topology of the circuit to match each measurement, which uses five resistors whose value was toggled between $0.1\text{m}\Omega$ and $50\text{G}\Omega$ according to the desired configuration. For example the model in Fig. 3.3 can emulate the parasitic measurements if $R_{sel}(1,3,4,5)$ are configured as a short and the others as an open circuit, the DM configuration when just $R_{sel}(2,5)$ are shorted and finally the CM configuration with only $R_{sel}(1,3,4,5)$ shorted. The value of these resistors will be changed in the same manner in which the parameters of the model were changed, that is defining them as global variables.

It must be said that designing the circuit in Simulink is not necessary if the network is simple and it can be calculated with simple algebra in the Transfer Function equations: this allows the GA to run much faster because the Simulink solver will not be invoked, the solution will be reached by only processing some matrices, the task Matlab is designed for.

This procedure has been used to model the converter's parasitics and the filter's components, where there is no mutual inductance. For example, for the model in Fig. 3.4, the equations to determine its impedance were simply:

```

tfc1 = tf(1, [C1 0]);
tfl1 = tf([L1 0], 1);
tfc2 = tf(1, [C2 0]);
tfl2 = tf([L2 0], 1);
tfp = 1/(1/tfc2+1/tfl2 +1/R2);
tft = tfc1+tfl1+R1+tfp;
[mag1, phase1, w1] = bode(tft, Frq*pi*2);

```

The model, in this case, is actually created only by the last two rows, hence the ease of use of this method is clear.

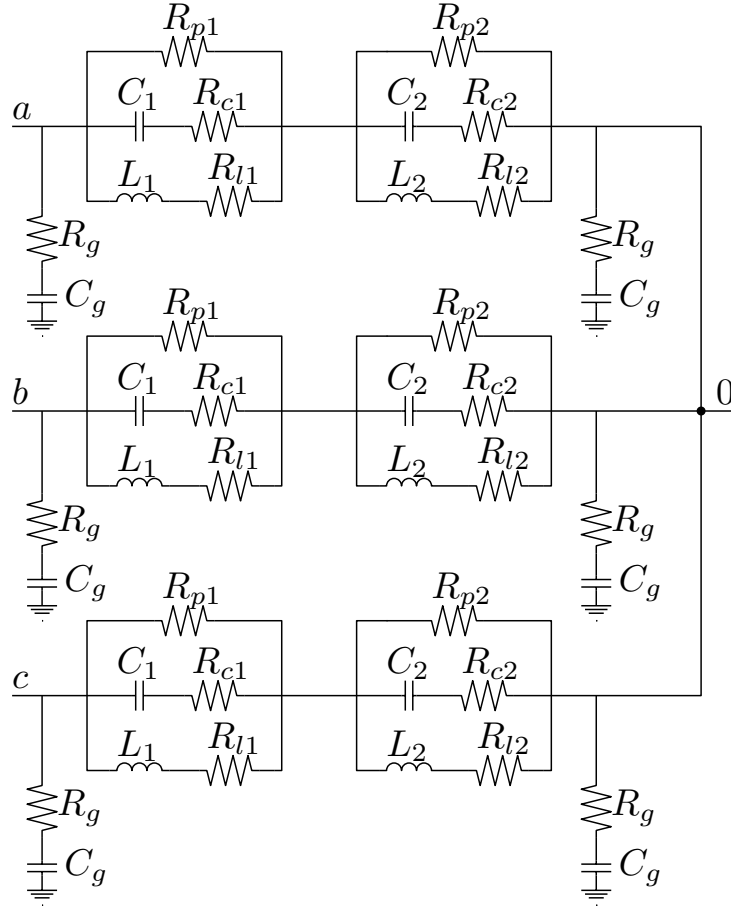
Motor and matrix converter model

4.1 Introduction

This chapter gives the details of the various HF models of the system, starting with the motor. Some articles have been selected to provide guidance with the motor modeling, such as [44] and [45]. However the models rely on basic HF motor schemes that are not capable to match effectively the measured motor's impedance in this work. Two other approaches presented in the literature [26] and [4] have proven feasible for our application suggesting an accurate HF motor model. The procedure described in the previous chapter will be used to fit the model's parameters to match the measured impedance; furthermore, after some investigations, the model in [4] will prove not to be fully compatible with the motor in use, so it will be refined to fit better with the actual impedance measurements. Afterwards a HF model for the matrix converter will be proposed, followed by the LISN model and the cable model, to fully replicate the whole system with a HF simulation.

4.2 HF motor modelling with Casadei's model

A promising HF IM modelling approach is described in [4], which is based on a previous work on an HF equivalent winding model [28]. The idea is to start from some experimental measurements and derive the motor model's parameters that fully characterize the model (Fig. 4.1) in a way that matches the measurements. It is possible to see that the parasitic capacitance C_g can easily be measured short-circuiting all the winding terminals and measuring the impedance across this point and ground, this will easily identify C_g and R_g . [4] presents some guidelines to identify some other parameters, such as the total inductance $L_1 + L_2$ measuring it at low frequency across the



M_1 = Mutual inductance between L_{1a}, L_{1b}, L_{1c}
 M_2 = Mutual inductance between L_{2a}, L_{2b}, L_{2c}

Figure 4.1: Casadei's HF induction motor schematic

windings, the total mutual inductance by measuring the inductance across two windings connecting them with positive and negative coupling, and the total input-output capacitance by measuring it at high frequencies. However, not all of the model's component can be so easily identified directly from the measurement, and the approach used in [4] to finally determine every single component is based on a trial-and-error method. This approach did not produce satisfactory results when applied for the identification of the IM motor HF circuit parameters in our specific case.

4.2.1 Difficulty to find adequate models

When trying to use the HF model in Fig. 4.1 to fit the experimental measurements with the GA, it has been noticed that the model as it was could not fit the parasitic measurements (shown in Fig. 4.2), because the simple RC network Fig. 4.1 that is

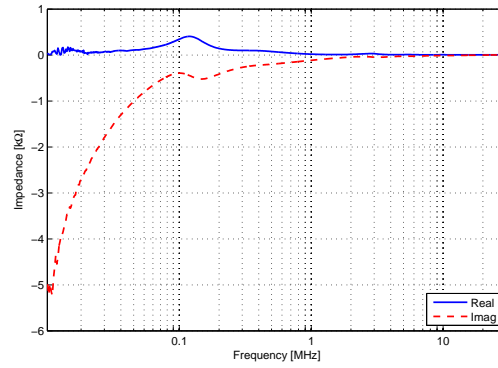


Figure 4.2: Motor: parasitic impedance measurement

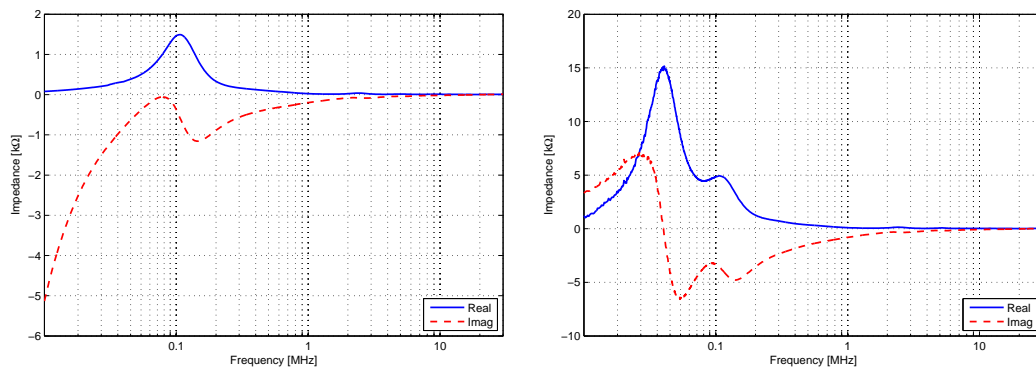


Figure 4.3: Motor: common and differential mode impedance measurement

supposed to characterize it, simply can not have a resonance as it appears at about 100kHz (Fig. 4.4). Therefore a new model has been proposed in this work that is able to replicate with more accuracy the impedance behaviour of the actual measurement.

4.3 Suggested HF Motor model

To overcome the aforementioned mismatching a new model has been proposed. This model has been developed on the reasonable assumption that the current, before coupling to the motor's case by means of the stray capacitance, will flow through some part of the winding. Thus, in the proposed model, there is a coil like network before the stray capacitance components, and assuming input-output symmetry the new model is represented in 4.5. Now the parasitic measurement can be easily fitted, as it is possible to see in Fig. 4.6. For this fitting only the outer components in the model have been identified during the optimization, the central part of the model will not carry any current during the parasitic measurement, hence it will not be possible to characterize it. The final optimized values for the components are listed in Table 4.1.

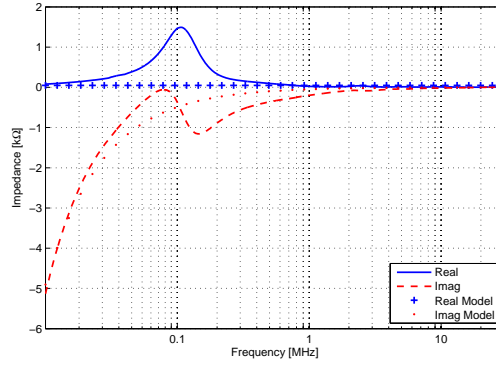
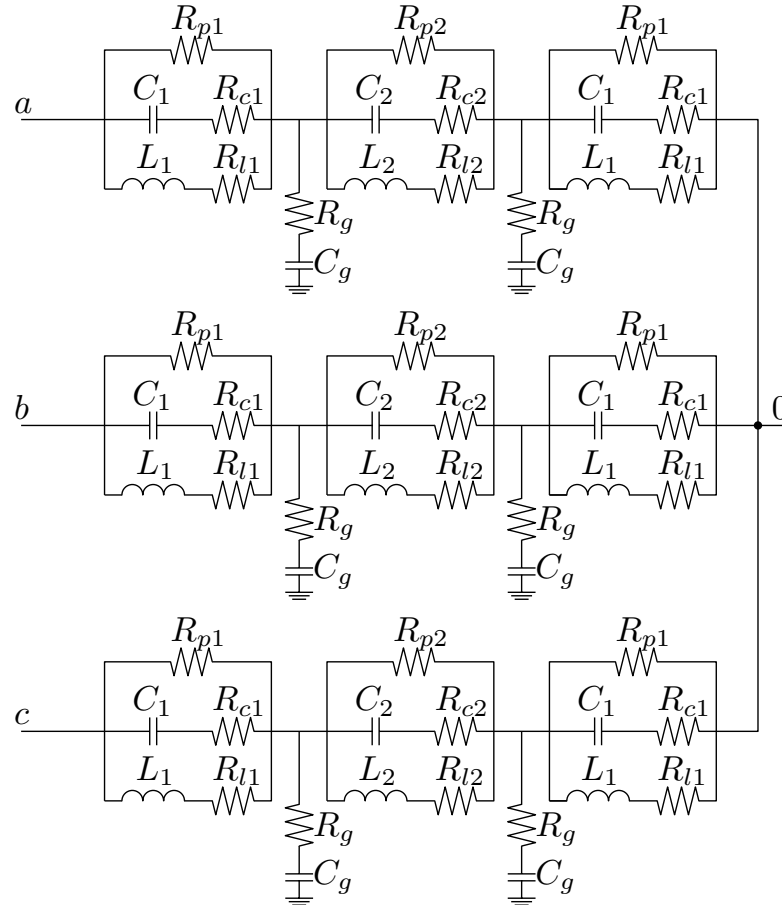


Figure 4.4: Attempt to fit motor’s parasitics with model as in [4]

Parameter	Range	Optimized Value
C_1	300p–1n [F]	622pF
L_1	1m–5m [H]	2.98mH
R_{c1}	1–80 [Ω]	54.5 Ω
R_{l1}	10–800 [Ω]	356 Ω
R_{p1}	1k–8k [Ω]	2.89k Ω
C_g	100p–1n [F]	527pF
R_g	10m–5 [Ω]	3.39 Ω

Table 4.1: Parasitics optimized parameters for proposed HF motor model



$$M_2 = \text{Mutual inductance between } L_{2a}, L_{2b}, L_{2c}$$

Figure 4.5: Proposed HF motor model

4.3.1 Attempt to reduce optimizing time

The idea of matching the impedance of the parasitics first comes from an attempt to reduce the optimization time. The variables have been split in two sets, the first one that includes the network toward ground and the outer coil-like network, and the second set that has the variables for the inner coil-like network. This process would lead to two different optimizations: the first one of seven variables (Table 4.1), and the second of just six. This could lead to better results than using only a single optimization process for the whole 13 variables because it reduces greatly the space of the search for the optimization: instead of a space of 13 dimensions, only half of it would have been necessary. However a set of simulations proved that the parasitic values found could not be assumed as the final values because the full model matching was not able to provide a close match. However this optimization, even if it could not provide useful values, allowed to determine the range for the variables that will be used for the next optimization process.

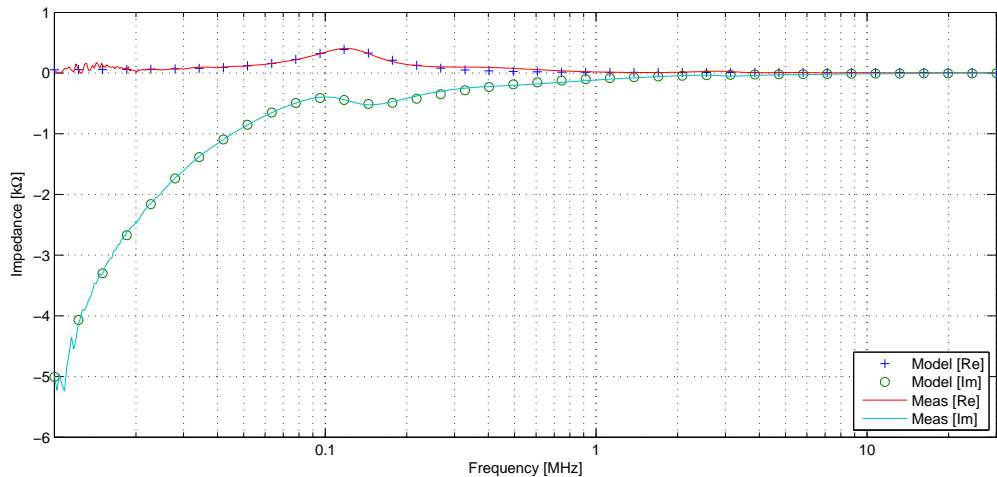


Figure 4.6: Motor's model parasitic fitting

4.3.2 Matching with impedance measurements

Different runs of the GA script were used to produce a good match with the measured impedance, sometimes the script fell in a local minima so a second run was useful to test if the result could be improved or not. When a parameter converges toward the limit imposed for a particular value, with some experience, it is possible to judge if that limit is too tight or if the script is going toward a local minima. Unfortunately there is no a direct way of discerning these two cases, but in general as a rule of thumb, if a variable gets too small it is because the procedure is trying not to use it. To solve this another run is needed, and an adjustment in the lower limit of that variable will be needed to force the program to investigate a solution with a significant value for that parameter. Regarding the simulations for the motor modelling, the used script was generating 250 individuals and 80 generations, and it took about 3 hours on a Core2 Duo 3GHz PC for each run.

Matching with common mode impedance measurements

During the CM optimization, the boundaries for the values obtained during the parasitics optimization have been kept the same as in Table 4.1 because they had already been narrowed down during a few successive optimizations of the parasitics components. In a generic run of the GA some values can have a range that spans over a few orders of magnitude, however in this case they are not bigger than one decade, thus helping the convergence of the GA. Table 4.2 reports the optimized values, comparing them with Table 4.1 it can be noticed that the common parameters are almost identical, thus proving the validity of the proposed method. The final impedance matching,

Parameter	Range		Optimized Value
C_1	300p–1n	[F]	669pF
L_1	1m–5m	[H]	2.91mH
R_{c1}	1–80	[Ω]	41.9 Ω
R_{l1}	10–800	[Ω]	352 Ω
R_{p1}	1k–8k	[Ω]	3k Ω
C_2	1n–5n	[F]	4.07nF
L_2	5m–50m	[H]	10.3mH
M_2	100n–110n	[H]	107nH
R_{c2}	100–50k	[Ω]	9.69k Ω
R_{l2}	10–400	[Ω]	381 Ω
R_{p2}	1k–100M	[Ω]	3.34M Ω
C_g	100p–1n	[F]	529pF
R_g	10m–5	[Ω]	0.54 Ω

Table 4.2: CM optimized parameters

applying these values to the model, can be seen in Fig. 4.7.

Matching with differential mode impedance measurements

Here the same considerations for the CM are applied, using the same range for the common parameters with the parasitics optimizations. Again the optimized values reported in Table 4.3 are very similar with the ones in Table 4.1, as expected. The final impedance matching, simulating this time the model for the differential mode topology, can be seen in Fig. 4.8.

4.4 Matrix converter model

The matrix converter is mainly a PCB board and few IGBTs, so it not expected to have a big resistive component nor an inductive one. Its parasitics are expected to be just capacitance to the ground, mainly due to the semiconductors, and some line to line capacitance due to the designed big power planes, assigned one for each phase. To model the converter the input capacitors have been removed, allowing a two step parametrization, by fitting them first and then studying the rest of the converter. Their model is depicted in Fig. 4.9 and the values can be found in Table 4.4 while the matching of the measured impedance with the simulated one is in Fig. 4.10.

Parameter	Range	Optimized Value
C_1	300p–1n [F]	762pF
L_1	1m–5m [H]	2.72mH
R_{c1}	1–80 [Ω]	36.2 Ω
R_{l1}	10–800 [Ω]	150 Ω
R_{p1}	1k–8k [Ω]	2.8k Ω
C_2	1n–5n [F]	3.13nF
L_2	5m–50m [H]	23.8mH
M_2	100n–110n [H]	110nH
R_{c2}	100–50k [Ω]	8.45k Ω
R_{l2}	10–400 [Ω]	241 Ω
R_{p2}	1k–100M [Ω]	17.2M Ω
C_g	100p–1n [F]	551pF
R_g	10m–5 [Ω]	0.2 Ω

Table 4.3: DM optimized parameters

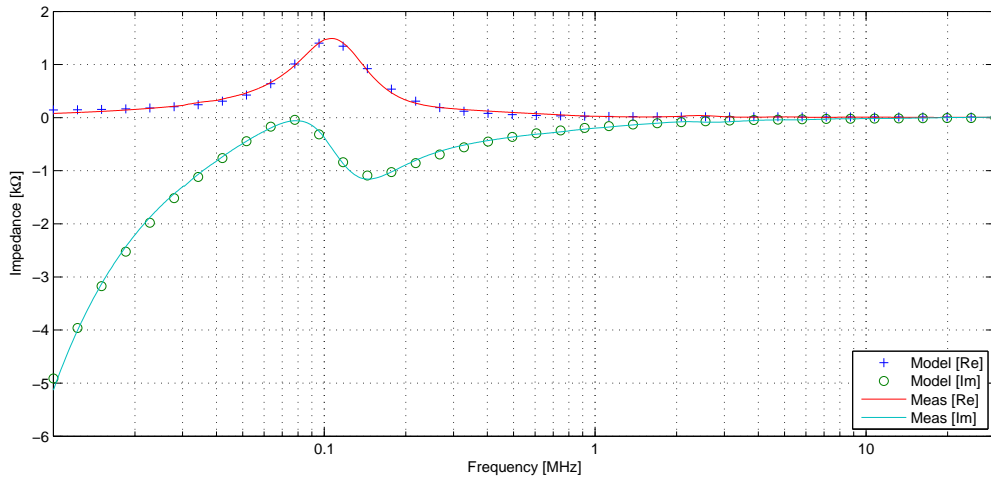


Figure 4.7: Motor's model common mode fitting

Parameter	Optimized Value
C_1	2.07 μ F
L_1	19.03 μ H
R_1	23.1m Ω
C_2	1.46 μ F
L_2	1.08nH
R_2	6.05m Ω

Table 4.4: Matrix converter input capacitors model values

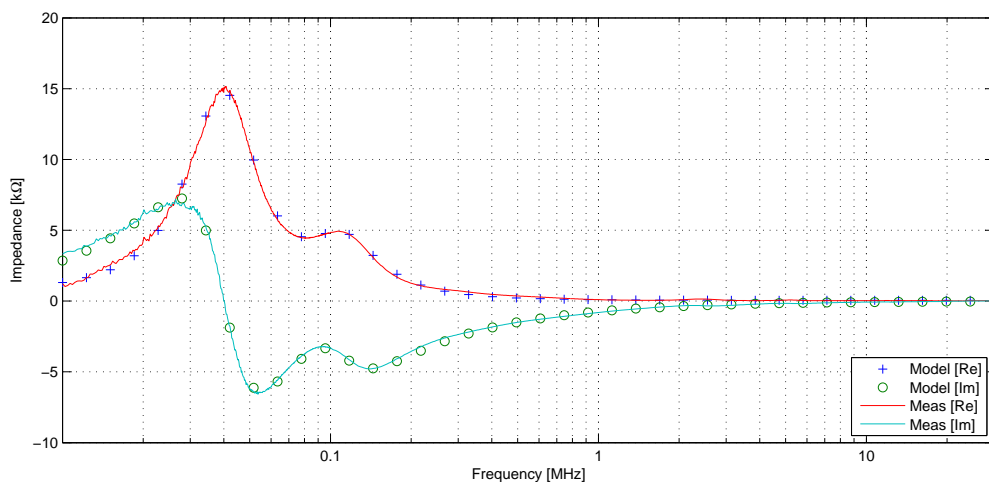


Figure 4.8: Motor's model differential mode fitting

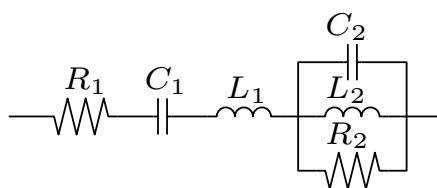


Figure 4.9: Matrix input capacitor equivalent network

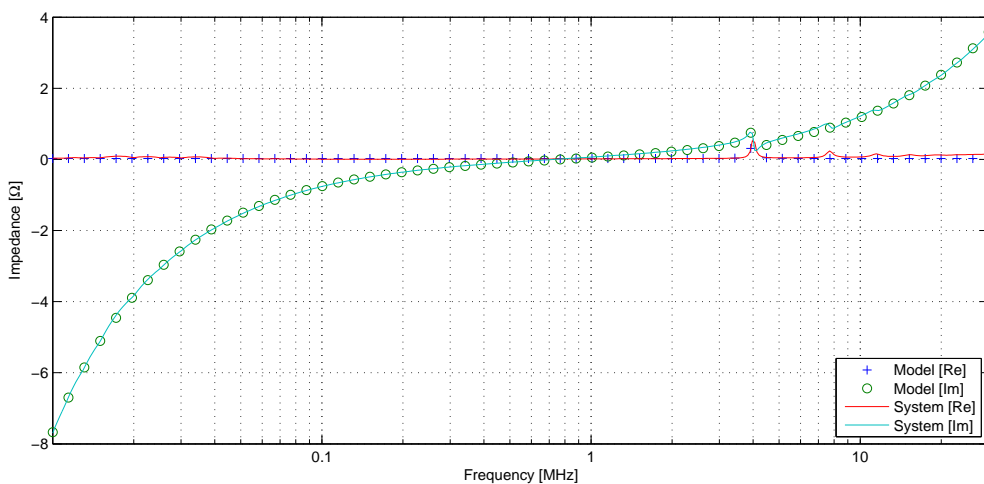


Figure 4.10: Matrix input capacitor measured and fitted impedance

Parameter	Optimized Value
C_{1cmi}	44.15nF
C_{2cmi}	4.69nF
L_{cmi}	77.59nH
R_{cmi}	99.37 Ω
C_{dmi}	6.8nF
L_{dmi}	57.35nH
R_{dmi}	14.12k Ω

Parameter	Optimized Value
C_{1cmo}	2.64nF
C_{2cmo}	415.2pF
L_{1cmo}	187.8nH
L_{2cmo}	610nH
R_{1cmo}	51.63k Ω
R_{2cmo}	1.26k Ω
C_{dmo}	719.6pF
L_{dmo}	257.9nH
R_{dmo}	31.13k Ω

Table 4.5: Matrix converter input and output parasitics model values

To further simplify the modelling for the converter this has been considered as the sum of two separate sections. The reason being that the IGBTs, when the board is not powered, act as an open circuit practically splitting the converter in two separate parts: one for the input with just some parasitic capacitive coupling between the tracks, and one for the output with the current sense transducers and the current direction sense circuitry. To measure properly the output parasitics impedance, the diodes used for the current direction sensing have been short circuited to emulate their conducting state. This is because they would otherwise act as a barrier for the low voltage signal used by the impedance analyser, effectively insulating the part of the matrix converter that comes after them. The measurements used to derive the system HF model are the usual two: differential and common mode, measured both at the input and at the output of the converter. For the modelling some considerations on the measurements helped to design the HF network: because for the CM measurements the parasitics components line to line will be shorted, only the parasitics components line to ground will play a role in the measurement, allowing a partial characterization of the parasitic network. Once the CM parameters have been identified their value will be taken into account to characterize the DM measurement.

4.4.1 Input and output CM impedance characterization

The common mode impedance measurement is the easiest to characterize because it consists only of the parasitics components between the lines shorted together and the ground (*-cm* components in the model). Some components in the model were identified from the topology, like the series capacitor (because there is no resistive path between the lines and ground) and the series inductor to represent the inductive behaviour of

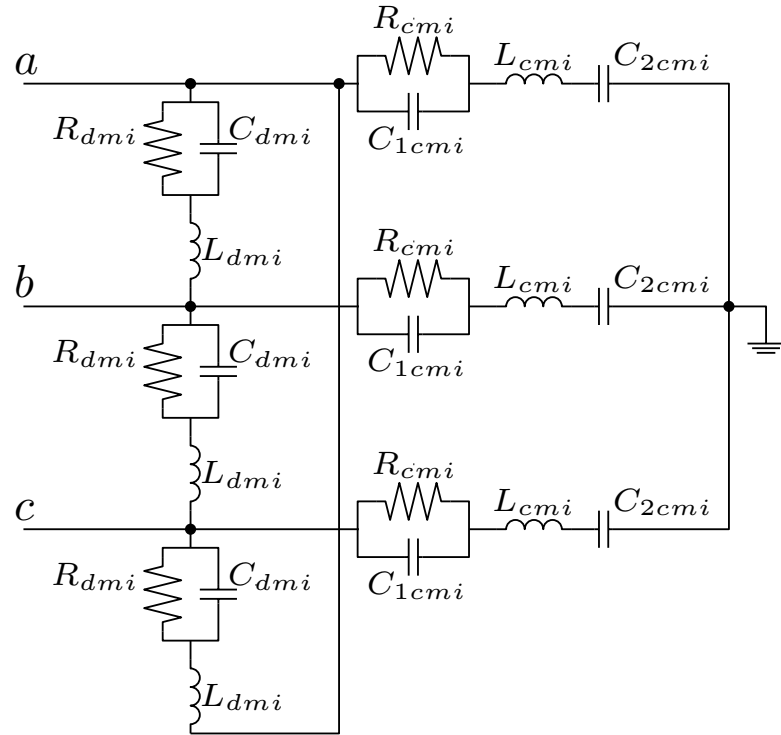


Figure 4.11: Matrix input parasitic network

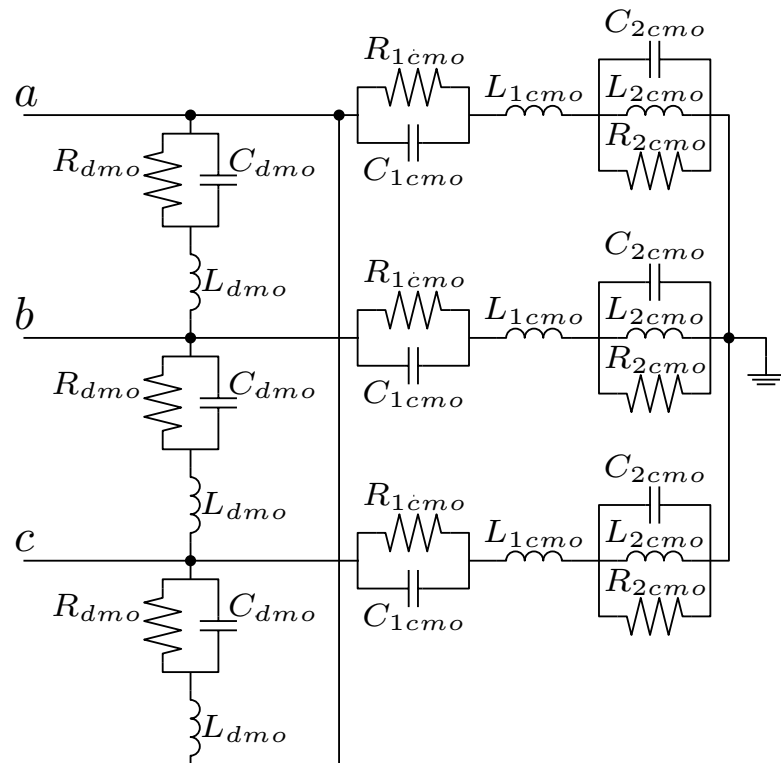


Figure 4.12: Matrix output parasitic network

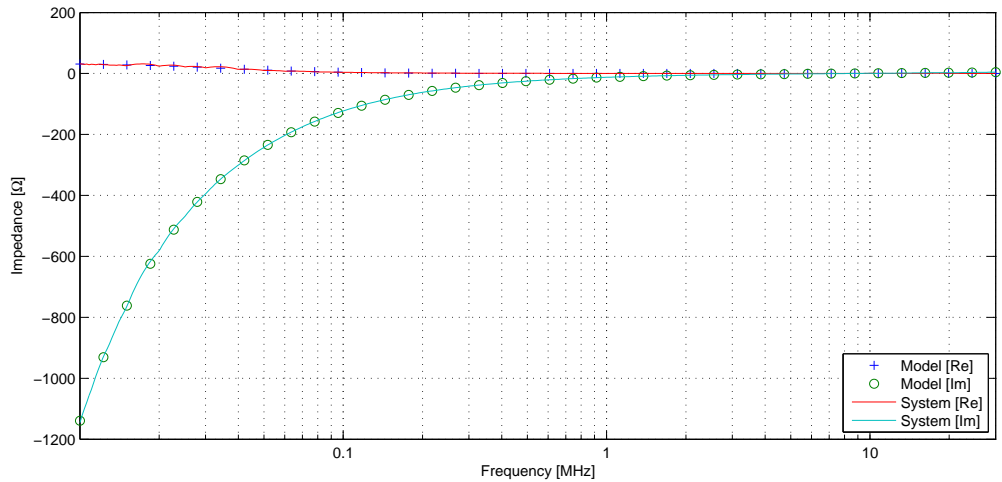


Figure 4.13: Matrix input CM: matching of the measured and simulated impedance

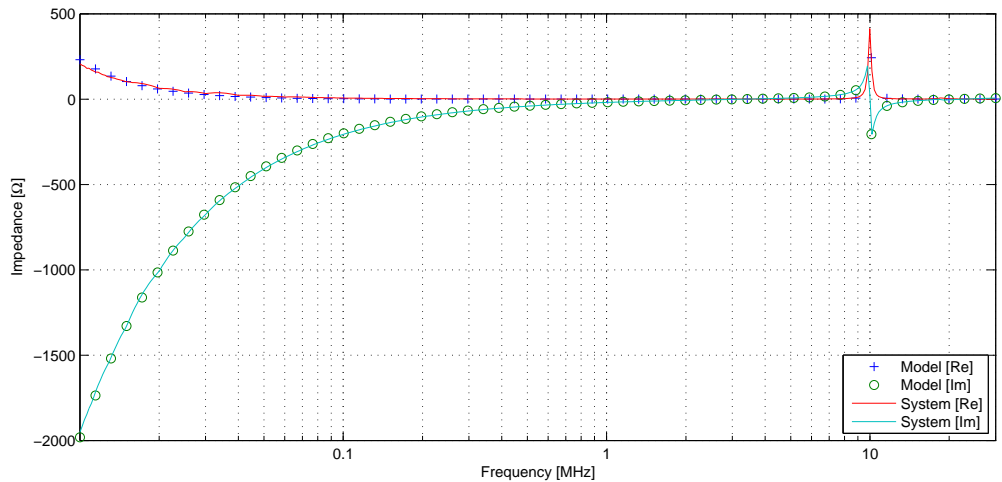


Figure 4.14: Matrix output CM: matching of the measured and simulated impedance

the PCB tracks. However for the other components the job was not as easy. Therefore a few different networks have been tried to match the reference impedance until a satisfactory match has been obtained. Considering that the final impedance is the parallel of the three parasitics, one for each phase, the GA algorithm was actually comparing the the reference with one third of the single phase parasitic impedance. Fig. 4.13 and 4.14 show the measured and the modelled CM impedance for the input and the output, obtained with the models in Fig. 4.11 and 4.12.

4.4.2 Input and output DM impedance characterization

Once the CM impedance network was identified, its components were included into the DM characterization. This is because the impedance measurement for the DM con-

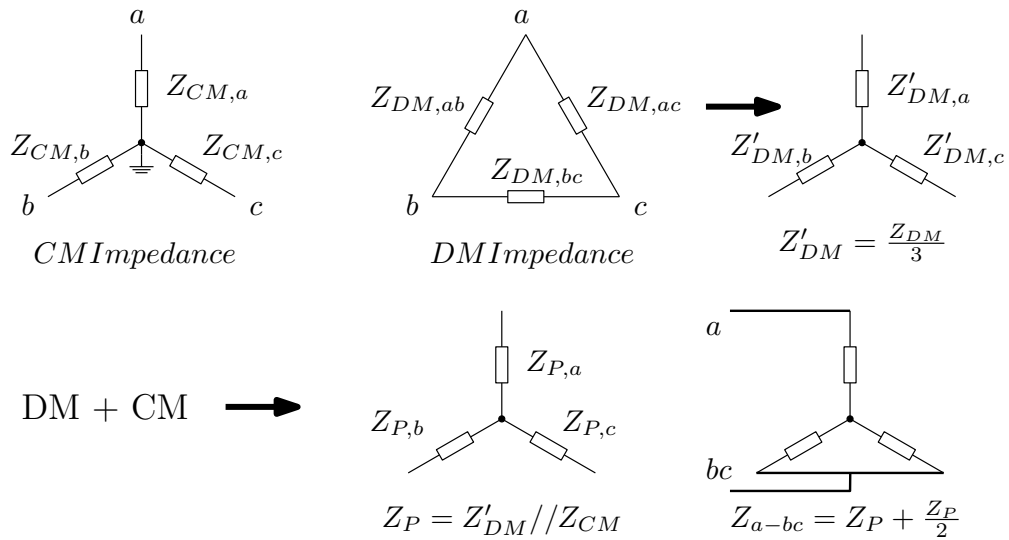


Figure 4.15: Procedure to calculate analytically the impedance across a-bc

figuration (for example measured between phase a and bc) includes the CM impedance too. To consider this into the DM impedance estimation, the CM extra impedance had to be added to the impedance calculation process. In order to do this, some transformations are needed to transform the DM impedance ($-dm$ components in the model) into star configuration, in a way so as to be able to calculate analytically the parallel value with the CM one, to get a final impedance value to be compared with the reference. Assuming a balanced system, Fig. 4.15 explains this process: the star equivalent value for the DM impedance is one third of the original (delta) value, and this will be in parallel with the CM single phase impedance. This value is the single phase equivalent star impedance value, and before being compared with the DM impedance value, it has to be multiplied by 1.5, considering the impedance a-bc, that is one phase plus the parallel of the other two. This final value was compared by the GA with the reference experimental impedance measurement for the DM configuration.

4.5 GA to model other components

4.5.1 Modelling of the LISN

The datasheet of the used Lisn, model: FCC-LISN-5-50-1-DEF STAN 59-41, provides its schematic as in Fig. 4.18. A detail is noticeable though: the inductor has multiple connections that are not further specified. On the datasheet a real impedance versus frequency is reported, so that graph has been imported in Matlab and a GA program has been used to evaluate the values of the 4 inductances, whose total value had to

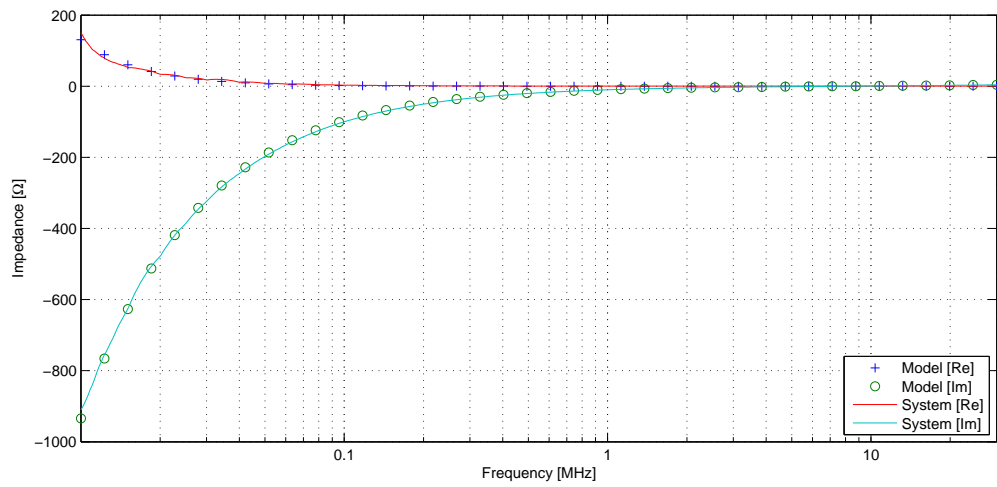


Figure 4.16: Matrix converter input DM: matching of the measured and simulated impedance

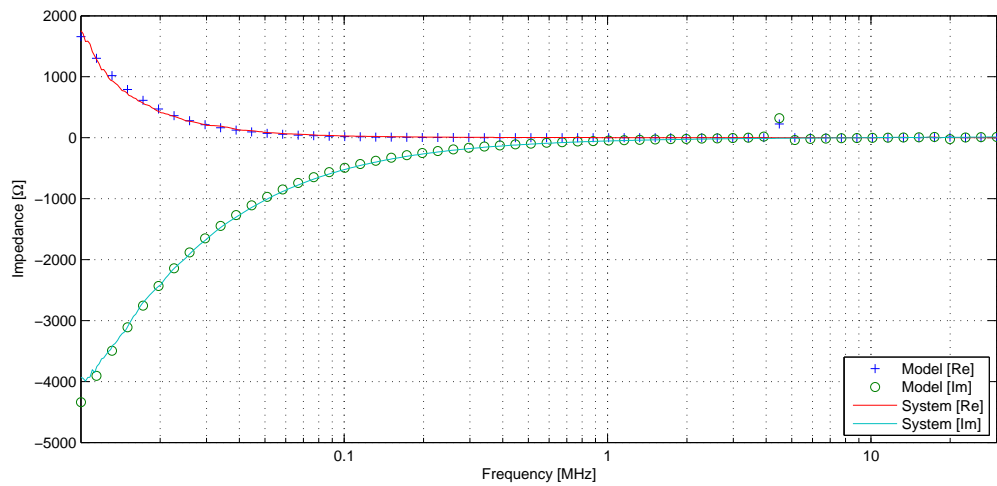


Figure 4.17: Matrix converter output DM: matching of the measured and simulated impedance

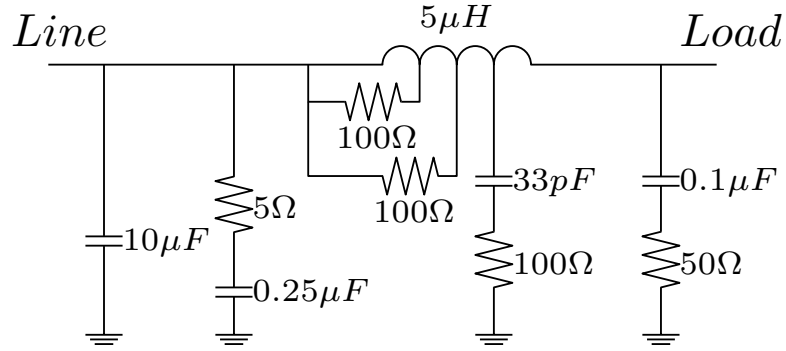


Figure 4.18: Lisen schematic

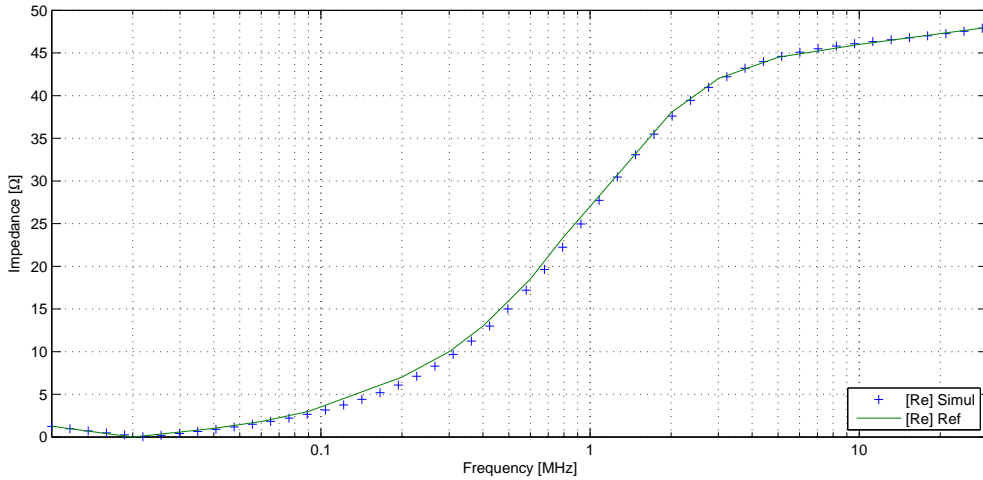


Figure 4.19: Lisen: matching of the reference and simulated impedance

match the 5mH. The result of the real part of the LISN impedance matching can be seen in Fig. 4.19, and the final values are reported in Table 4.6.

4.6 Cable model

The used cables have three conductors plus the earth, and they must be unshielded, according to aircraft specifications. Because the used cables are very short (1 and 2 meters) a geometrical approach for the HF modelling have been pursued, using the formulae in [29]; however for a general case of longer cables a full investigation would be needed.

Considering our case, for a multi-conductor cable with regular disposition of the wires, the specific capacitance and inductance, per unitary length, can be calculated with these

Parameter	Value
L_1 (Line)	0.1nH
L_2	1.9780 μ H
L_3	0.6753 μ H
L_4 (Load)	2.3466 μ H

Table 4.6: LISN main inductor values, in order from line side to load side

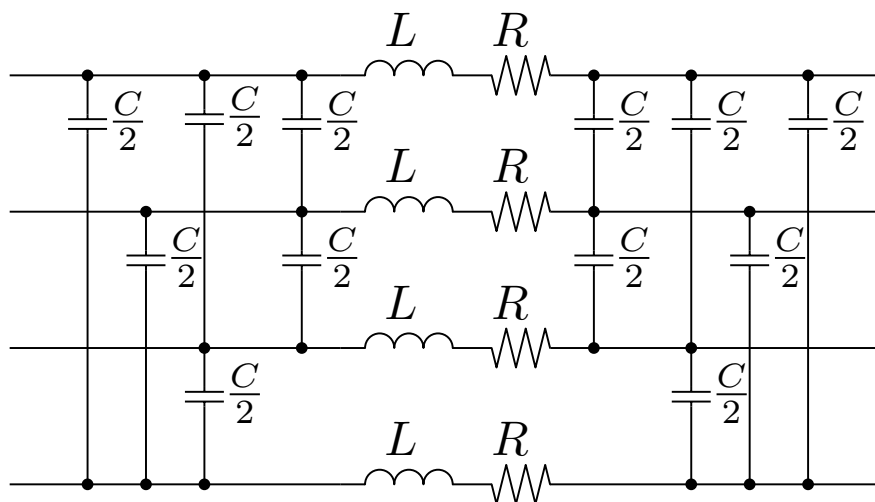


Figure 4.20: Cable model

formulae:

$$C_{cond} = \frac{2\pi\epsilon_0}{\ln\left(\frac{d_m}{r}\right)} [F/m] \quad (4.6.1)$$

$$L_{cond} = \frac{\mu_0}{2\pi} \ln\left(\frac{d_m}{r}\right) [H/m] \quad (4.6.2)$$

d_m is the geometric mean of the distances between the conductors and r is the radius of the conductor. A cable with four conductors, equally spaced, can be modelled with lumped parameters as in Fig. 4.20.

Using Rosen's theorem [46], the capacitance between two conductors a, b in a cable is so calculated:

$$C_{ab} = \frac{C_a C_b}{\sum C_k} \quad (4.6.3)$$

Therefore for a regular cable with n conductors, where all conductors have equal capacitance, 4.6.3 can be simplified as:

$$C_{cab} = \frac{C_{cond}}{n} \quad (4.6.4)$$

Assuming that the conductor are symmetrically arranged such that they lie at the corners of a square of side d , the mean geometric distance d_m is equal to:

$$d_m = d \cdot \sqrt[3]{1 \cdot \sqrt{2} \cdot 1} = d\sqrt[6]{2} \quad (4.6.5)$$

Tables 4.7 and 4.8 report the physical dimensions and the model parameters for the input and output cables used on the experimental setup.

Physical dimension	Measure	Model parameter	Value
Length	2 m	L	500 nH
Copper section	6 mm ²	C	22.2 pF
Insulation diameter	4.3 mm	R	5.6 mΩ

Table 4.7: Input cable, dimensions and model parameters

Physical dimension	Measure	Model parameter	Value
Length	1 m	L	255 nH
Copper section	4 mm ²	C	10.9 pF
Insulation diameter	3.6 mm	R	4.2 mΩ

Table 4.8: Output cable, dimensions and model parameters

EMI Measurements

5.1 Introduction

This chapter will describe in detail the procedures carried out to obtain the conducted EMI measurements for the matrix converter drive under test. The test procedures, environmental conditions and emissions limits are fully described in [1], in particular in Section 21. "*Emission of Radio Frequency Energy*" that is the part regarding this project. The relevant sub-parts of this section will be reported in 5.2, to provide a summary of the conditions that need to be fulfilled during the measurements.

In section 5.3 a guide will be provided on how to calibrate the current probe used with the spectrum analyser, a necessary procedure that is needed for every probe that will be utilized; without this all the measurements will be meaningless because the actual readings will be of the probe's output neglecting completely its conversion ratio; on top of this, probes in general are not supposed to have a constant gain, instead they have a profile that varies with frequency and this needs to be taken into account.

This is a long procedure and is not easy to find descriptions on how to do it, so this section is meant to be as a reference to engineers needing to perform EMI measurements in the future.

The last section 5.5 describes the experimental EMI measurements taken at the matrix converter input and output during normal drive operation, with some description on how these measurements have been taken. It will also include a comparison on the emissions produced by a two level inverter running at the same operating conditions, driving the same motor; a measurement of the common mode voltage measured for both converters will also be provided.

5.2 Requirements for conducted EMI

Requirements for the measuring setup are defined in [1], which regulates every aspect of the layout and interconnections of the Equipment Under Test (EUT). For the emissions of Radio Frequency Energy there are several categories in which equipments are divided in, according to the position within the aircraft, with different limits according to how sensible the location is. The category in which a matrix converter drive falls is "L", defined as in the following:

This category is defined for equipment and interconnected wiring located in areas far from aperture of the aircraft (such as windows) and far from radio receiver's antenna. This category may be suitable for equipment and associated interconnecting wiring located in the electronic bay of an aircraft.

The document defines also how the measurements needs to take place, how to interconnect the device and how to set-up the instrumentations. The settings defined for the interference measuring equipment specify that the peak detector function needs to be selected, with Impulse bandwidth (BWI) of 1kHz; it also cites that the time constant of the peak detector must be lower or equal to 1ms.

For the interconnections a Line Impedance Stabilization Networks (LISNs) must be used to feed the EUT, to have a fully characterized source impedance of 50Ω.

It defines the measurement layout, where the current probe needs to be inserted five centimetres from the EUT, as depicted in Fig. 5.1.

The maximum admissible conducted emissions limits, for the conditions described above, is within the range 150kHz–30MHz, are shown in Fig. 5.2.

5.3 Probe calibration

The current probe used is a FCC F-35A, which have an operation bandwidth of 100Hz - 100MHz. This specific probe has a typical transfer impedance of 0 dBΩ between 100kHz and 30MHz, as visible in its calibration curve in Fig. 5.3; this means that without calibration the error introduced will be negligible, but doing this will be a good practice and the procedure will be useful as a reference for other probes. The calibration consists in measuring the probe's output for a reference input signal in the bandwidth of interest to obtain experimentally the transfer impedance versus the frequency, either if the datasheet is not available or to make sure the probe is working properly. The instruments used during the procedure are a Signal Generator Agilent E8257C and a spectrum analyser Agilent MXA N9020A.

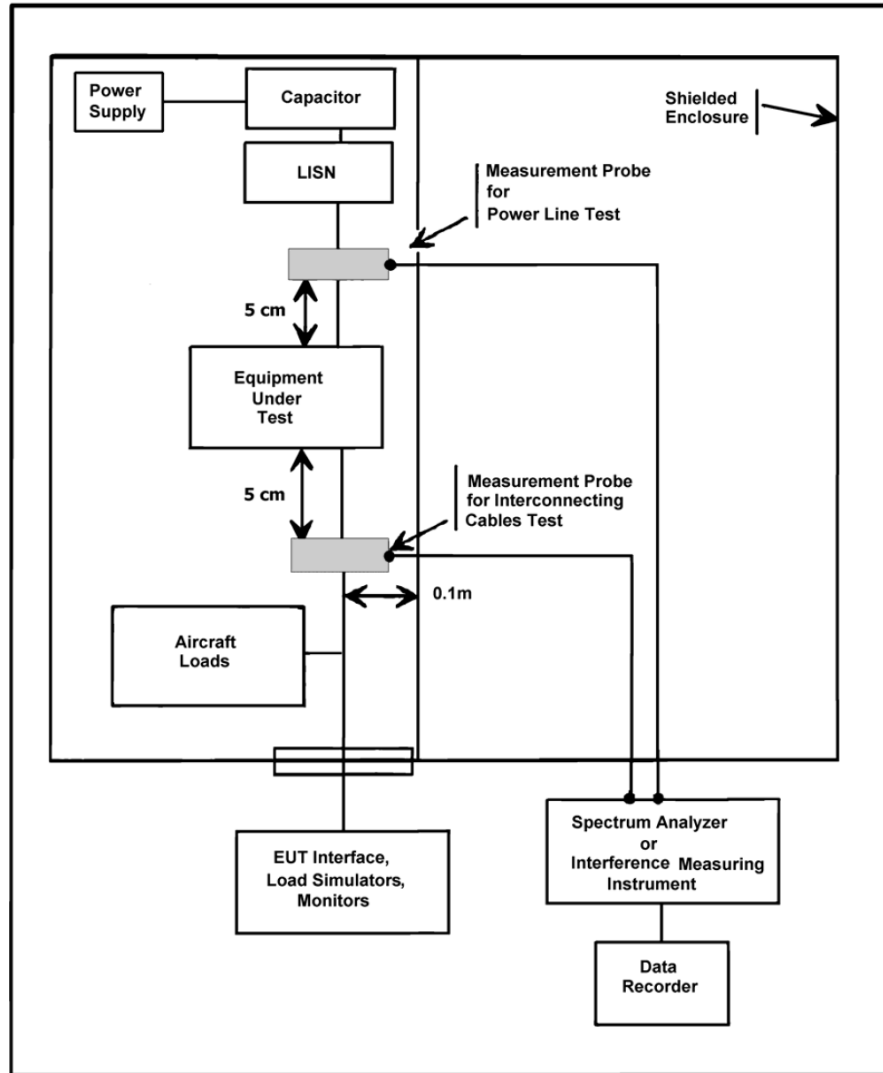


Figure 5.1: Typical Setup for Conducted RF Interference Test

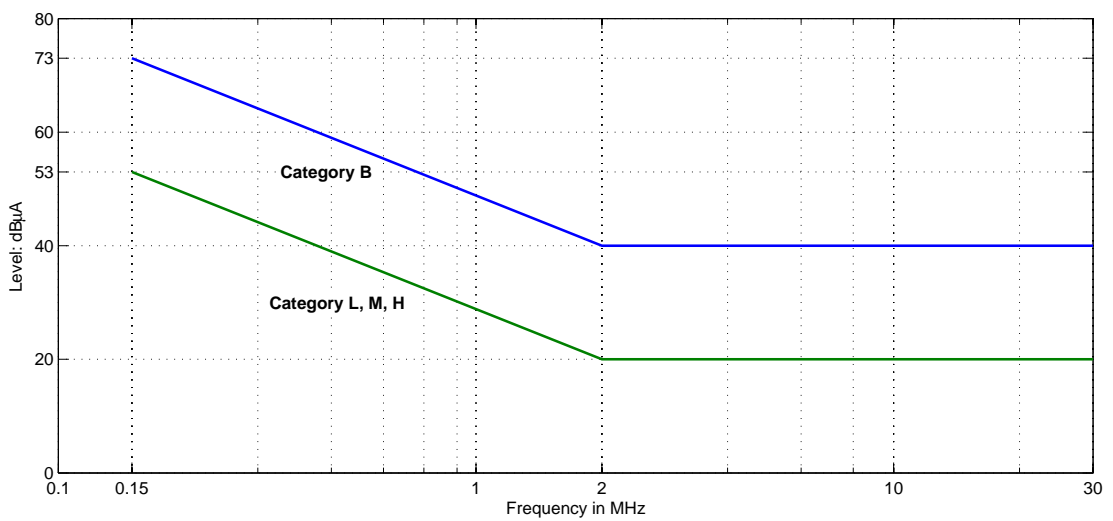


Figure 5.2: Maximum Level of Conducted RF Interference – Power Lines

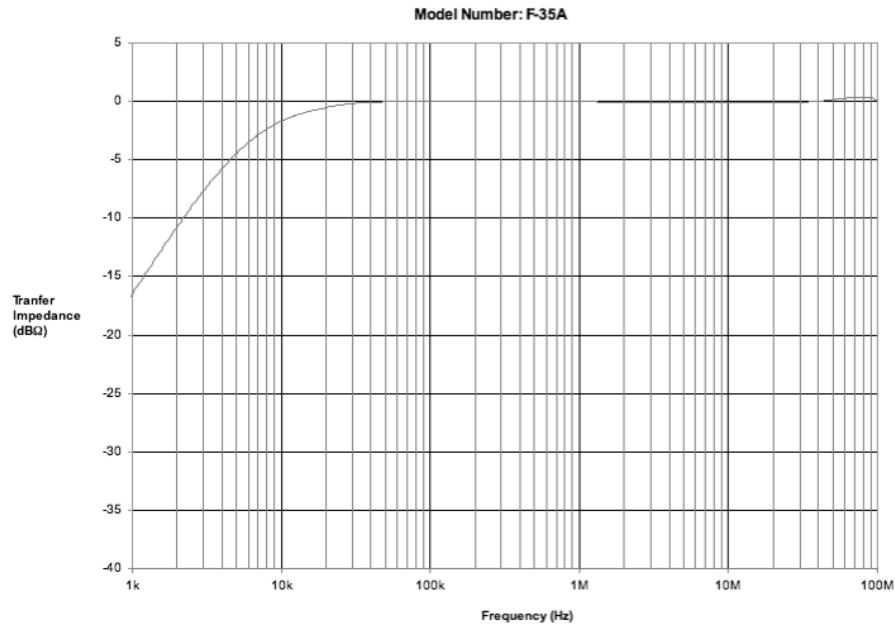


Figure 5.3: Calibration curve for current probe FCC F-35A

5.3.1 Calibration procedure

The current probe has a voltage output measured across the "50 Ohm input" of the Spectrum Analyser; to obtain the current measurement Ohm's law is applied, using the known transfer impedance:

$$I_p = E_S / Z_T$$

The same formula, applied to values in dB is:

$$I_p(\text{dB}\mu\text{A}) = E_S(\text{dB}\mu\text{V}) - Z_T(\text{dB}\Omega) \quad (5.3.1)$$

Therefore to get the current measurement in dB, from the voltage readings on the Spectrum Analyser, the Transfer Impedance Z_T needs to be subtracted. Because Z_T changes throughout the frequency, its behaviour needs to be recorded and used to obtain a precise measurement. In order to do this, pairs of Voltage and Current values will be recorded for all the frequency that will be used for the emissions measurements.

The first step is to measure the reference current injected by the Signal Generator into the 50Ω nominal load; the generator should inject a constant test reference current, but for such a wide range of frequencies this is unlikely to be verified, so in this measurement the actual reference current is recorded. For this measurement three connections are needed: a BNC cable must connect the "10MHz Out" on the Spectrum Analyser to the "10MHz In" of the Signal Generator; another BNC cable must connect the "Trigger Out" from the Signal Generator to the "Trigger In" of the Spectrum Analyser, this

will trigger the frequency measurement for every frequency step. A RF cable must be plugged from the output of Signal Generator into the Spectrum Analyser, to feed the signal into the measuring instrument.

Settings on the Spectrum Analyser

BW:	Res BW → 100kHz
AMPTD Yscale:	More → Y Axis unit → A
Trace/Detector:	Max Hold
Trigger:	External 1
FREQ Channel:	Start Freq → 100kHz Stop Freq → 30MHz
Sweep/Control:	Points → 29901
Input/Output:	RF Input → RF Coupling → DC

Settings on the Signal Generator

Sweep/List:	<ul style="list-style-type: none"> • Sweep Type → Step • Sweep Repeat → Cont • Configure Step Sweeps: <ul style="list-style-type: none"> – Freq Start → 100kHz – Freq Stop → 30MHz – # Points → 29901 – Step Dwell → 40 ms
Frequency:	100KHz
Amplitude:	-10dBm

Once the sweep on the Signal Generator will be complete, the Spectrum Analyser will have stored the reference, that will have to be exported to provide the vector of current vs. frequency values.

Once the reference is saved, the proper measurement for the probe's impedance has to take place. For this calibration the probe must be placed in the Current Probe Calibration Fixtures, as in Fig. 5.4; for this configuration four connections are needed: the usual two BNC for the 10MHz and the trigger signal, then two RF cables, one to connect the probe to the spectrum analyser and the other to connect the signal generator to the calibration Fixture (the metallic box visible in Fig. 5.4). Note: the other plug of the calibration fixture must have a 50Ω terminator to match the cable's impedance.

The settings on the instruments are the same as before, with the only exception for the Y scale on the spectrum analyser, this parameter should now be volts (V), to read the



Figure 5.4: Setup for current probe calibration

voltage output of the current transducer. Once this second sweep has been performed and the data exported, the probe's impedance can easily be computed for each frequency simply dividing the voltage by the current references. This will generate a list of impedance values, one for every frequency of the sweep. Calculating the logarithm of this values will provide the Z_{db} values, to be used with the formula 5.3.1 to translate the voltage reading from the spectrum analyser into proper current readings.

5.4 Experimental current measurements: CM & DM

This section deals with the EMI current measurements, showing how to perform the readings with the spectrum analyser for a two and a three wire system, with the assumption that the currents flow as illustrated in Fig. 5.5.

Regarding the former case, the CM and DM currents can be acquired as depicted in Fig. 5.6 [47, 48]. The CM configuration is clear because it has to measure the current that flows through the earth connection, and it comes from both the line wires. The DM configuration may seem odd but this is necessary to remove the CM component from the line current, and it can be explained with some algebra [49]. Considering that the line current comprises both CM and DM parts (Fig. 5.5) it is clear to see that $i_A = i_{DM} + \frac{i_{CM}}{2}$ and $i_B = -i_{DM} + \frac{i_{CM}}{2}$, hence the measurement will simply perform the following equation:

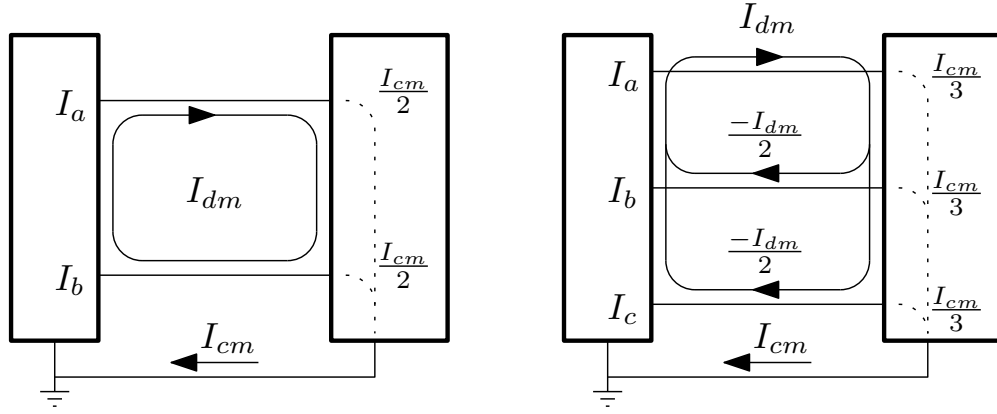


Figure 5.5: Path for common and differential mode currents for two and three wire systems

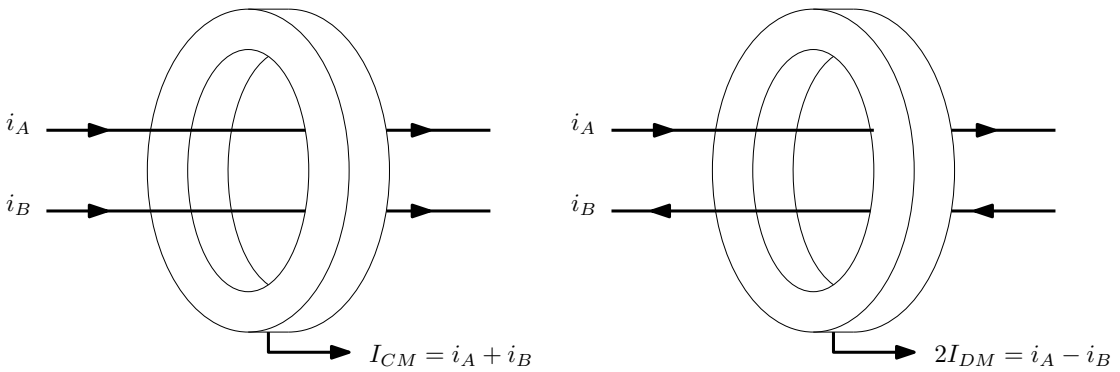


Figure 5.6: CM and DM current measurement for a two wire system

$$i_A - i_B = i_{DM} + \frac{i_{CM}}{2} + i_{DM} - \frac{i_{CM}}{2} = 2 \cdot I_{DM}$$

For a three phase system, like the case of the matrix converter under study, the arrangement for the CM is simple to understand: it has to include all the three wires. However, for the DM measurement (Fig. 5.7), there is a different arrangement. Looking again at Fig. 5.5 the three currents are so defined: $i_A = i_{DM} + \frac{i_{CM}}{3}$, $i_B = \frac{-i_{DM}}{2} + \frac{i_{CM}}{3}$ and $i_C = \frac{-i_{DM}}{2} + \frac{i_{CM}}{3}$.

This wiring layout will therefore represent:

$$2 \cdot i_A - i_B - i_C = 2 \cdot i_{DM} + 2 \cdot \frac{i_{CM}}{3} + \frac{i_{DM}}{2} - \frac{i_{CM}}{3} + \frac{i_{DM}}{2} - \frac{i_{CM}}{3} = 3 \cdot I_{DM}$$

Because of this configuration, to obtain the actual DM value, the measured values must be corrected dividing the value by 3 or, working in dB, subtracting 9.54dB (obtained simply with the usual formula $20 \cdot \log_{10}(3)$).

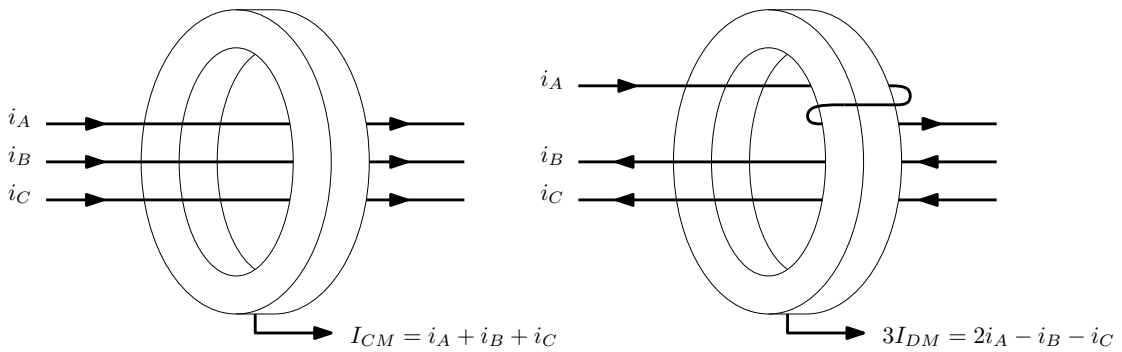


Figure 5.7: CM and DM current measurement for a three wire system

Settings on the Spectrum Analyser

BW: Res BW \rightarrow 1kHz
 AMPTD Yscale: More \rightarrow Y Axis unit \rightarrow More \rightarrow dB μ V
 Trace/Detector: More \rightarrow Detector \rightarrow Peak
 FREQ Channel: Start Freq \rightarrow 100kHz
 Stop Freq \rightarrow 30MHz
 Sweep/Control: Points \rightarrow 29901
 Input/Output: RF Input \rightarrow RF Coupling \rightarrow DC

Note: these and all the aforementioned settings for the instruments presuppose a start from the default settings present after the power-up sequence.

5.5 Actual measurements

The measurement at the input are in Fig. 5.8 and 5.9 for the CM and DM respectively. It is possible to see the limit for the emission stated in the aviation standard DO-160 is several tenths of dB lower than the real emission in the CM case, this will lead to several problems encountered during the filter design process.

Fig. 5.10 and 5.11 represent the emission at the output of the converter on the motor side. In this case both CM and DM emissions are far above the limit, leading to a very demanding filter design.

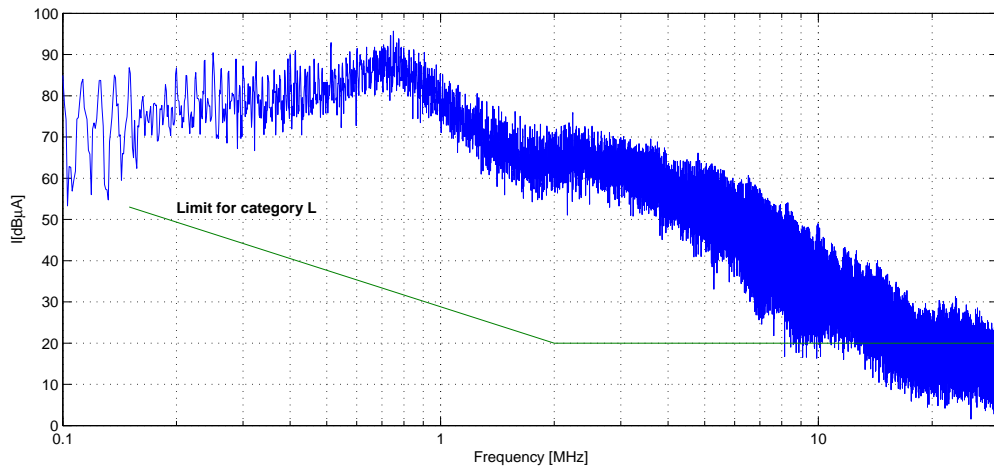


Figure 5.8: CM current measurement for the Matrix converter input

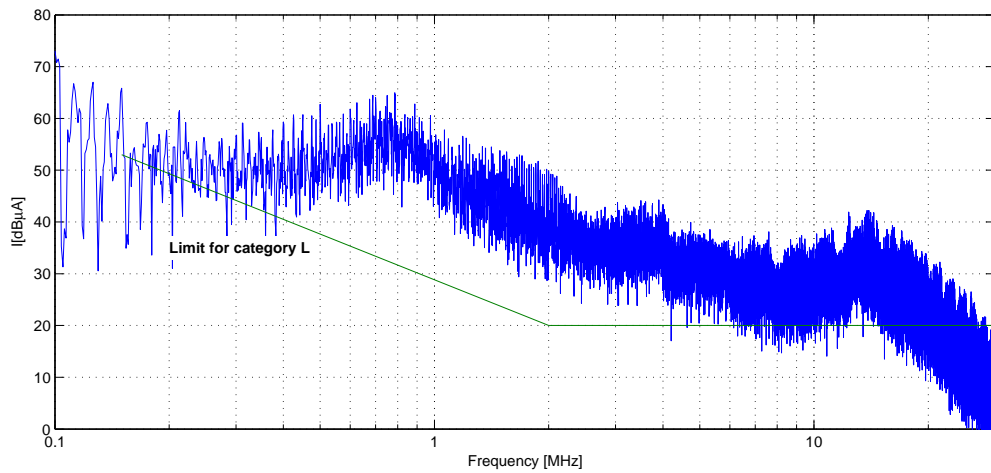


Figure 5.9: DM current measurement for the Matrix converter input

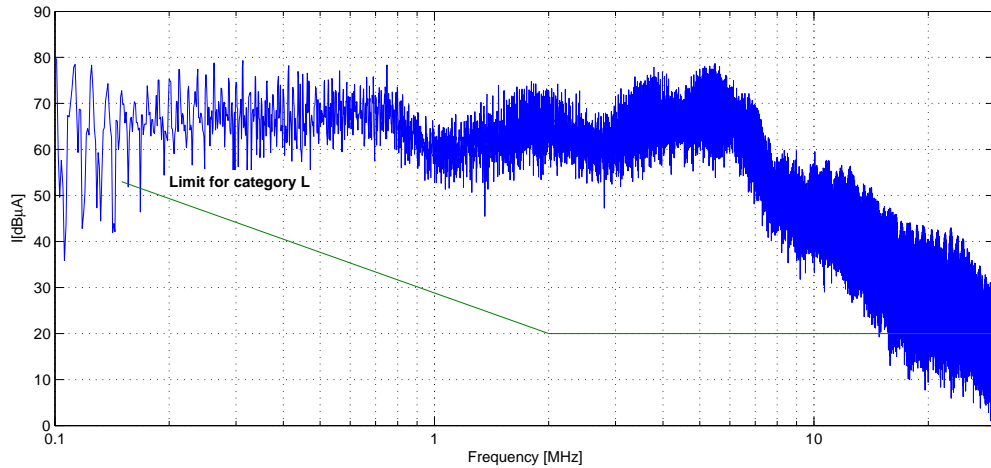


Figure 5.10: CM current measurement for the Matrix converter output, motor side

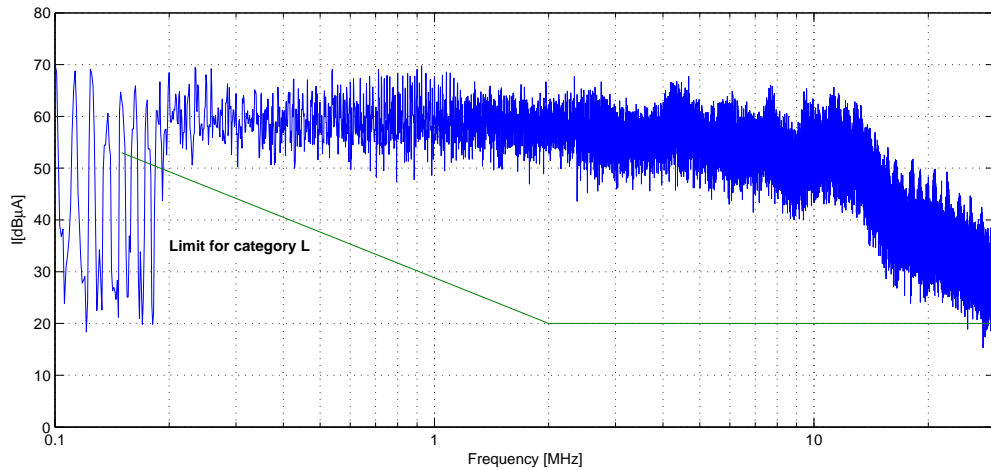


Figure 5.11: DM current measurement for the Matrix converter output, motor side

The same measurements have been performed to verify how the modulation index q will affect the emissions. Fig. 5.12 reports the output current of the Matrix converter for three different values of the modulation index: 0.6, 0.7 and 0.8; in the same figure it is possible to verify that the current increases by roughly 10% at each step.

Fig. 5.13 and 5.14 show the emissions at the Matrix converter input, where it is clear that there is no appreciable influence on the emissions by the value of the modulation index.

In Fig. 5.15 and 5.16 it is possible to see the same effect on the output emissions: again there is no influence, thus justifying the choice of an arbitrary value for the modulation index that has been fixed at 0.7 for all the emission measurements performed in this work.

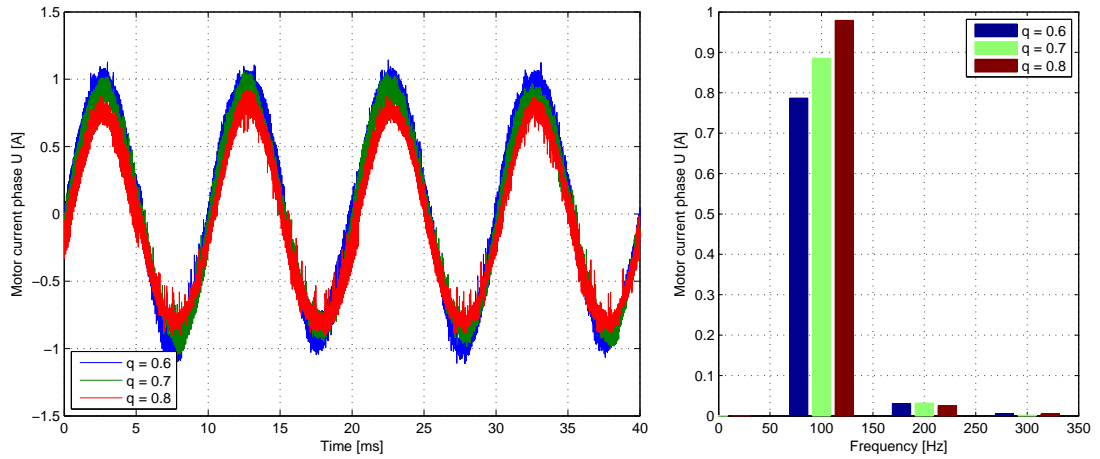


Figure 5.12: Output current for different values of modulation index q

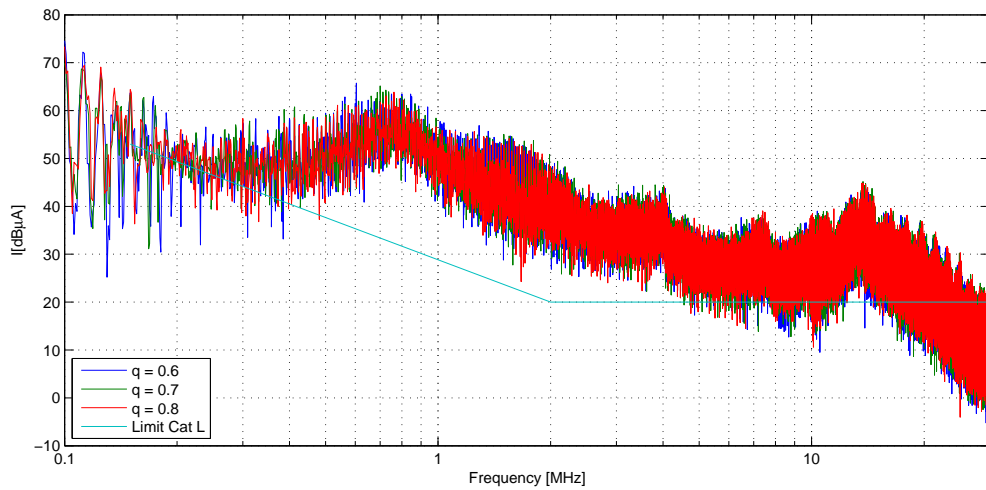


Figure 5.13: DM EMI at Matrix converter input varying q

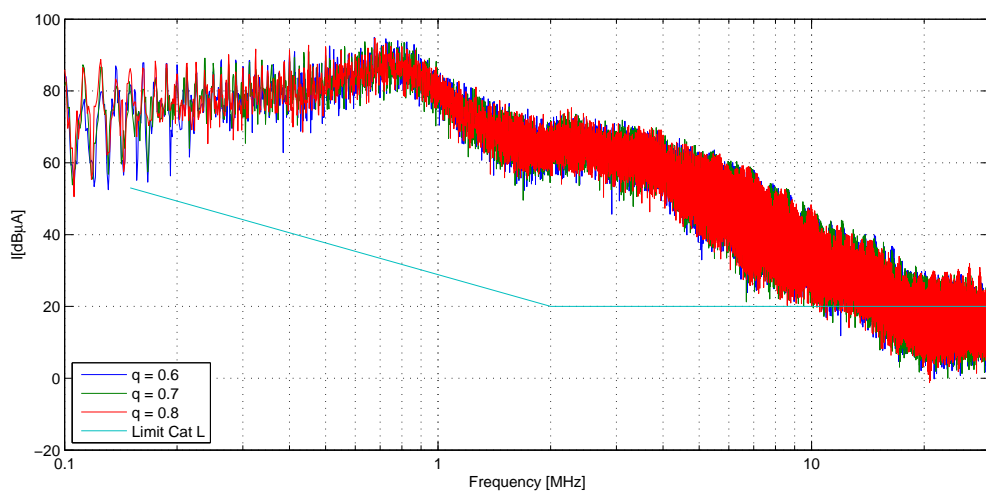


Figure 5.14: CM EMI at Matrix converter input varying q

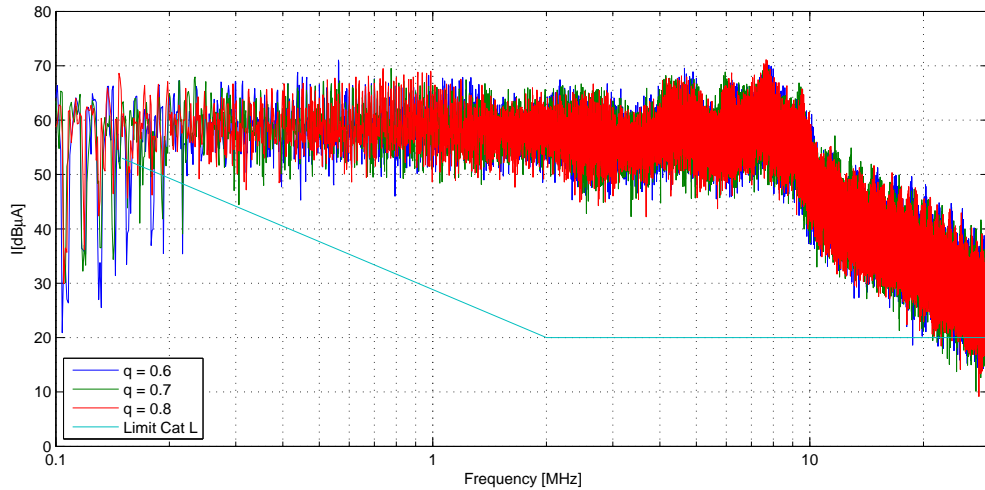


Figure 5.15: DM EMI at Matrix converter output varying q

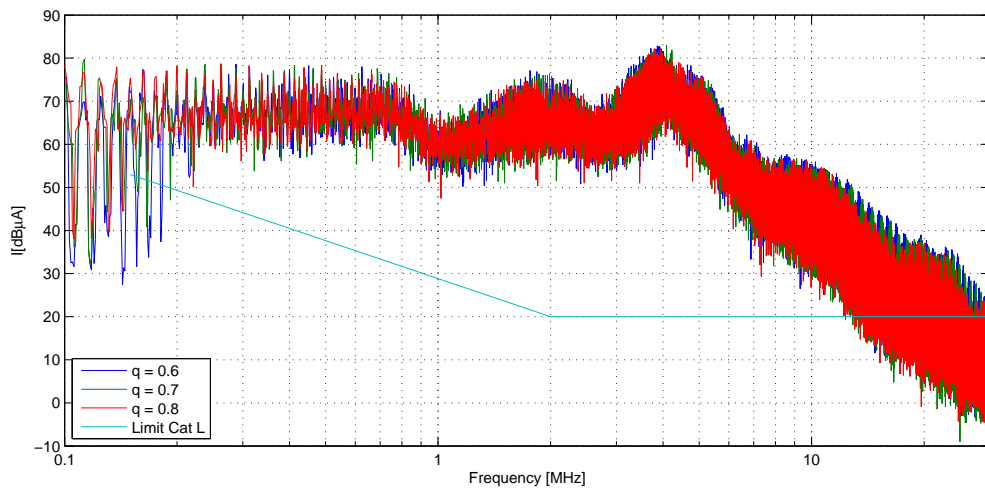


Figure 5.16: CM EMI at Matrix converter output varying q

5.5.1 EMI Comparison with a two level inverter

It could be interesting to compare the EMI emissions of the Matrix Converter with the ones of a traditional Two Level Converter. In order to do so, the same motor has been connected to a 15kW two level inverter switching at 12.5kHz (same as the matrix converter) with symmetric space vector modulation. The supply voltage is once again $240V_{rms}$ at 50Hz, the modulation index is 0.7 and the output frequency is 100Hz. The same EMI measurements have been performed, CM and DM, both at the input and at the output, and they are reported in the following figures. Fig. 5.17 and 5.18 report the emissions measured at the input while Fig. 5.19 and 5.20 show the emissions measured at the converter output.

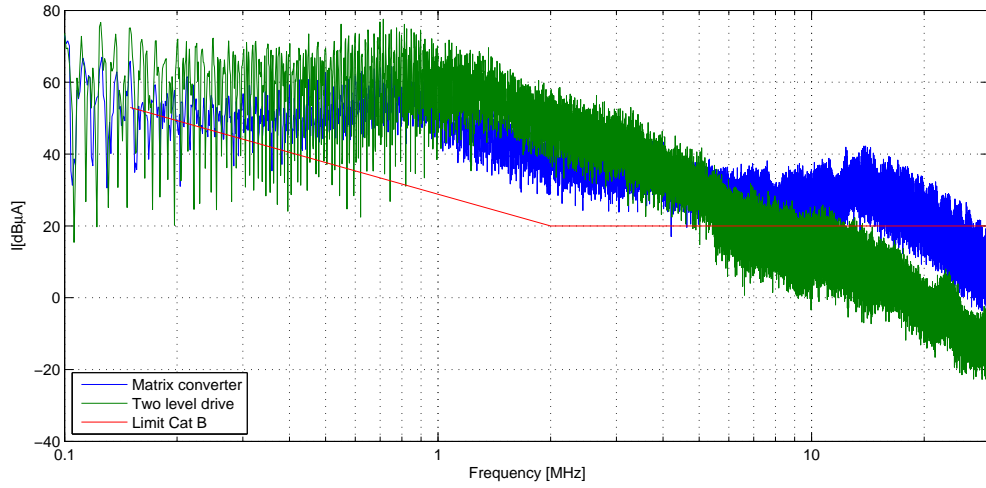


Figure 5.17: Input DM EMI comparison for Matrix and Two-level converters

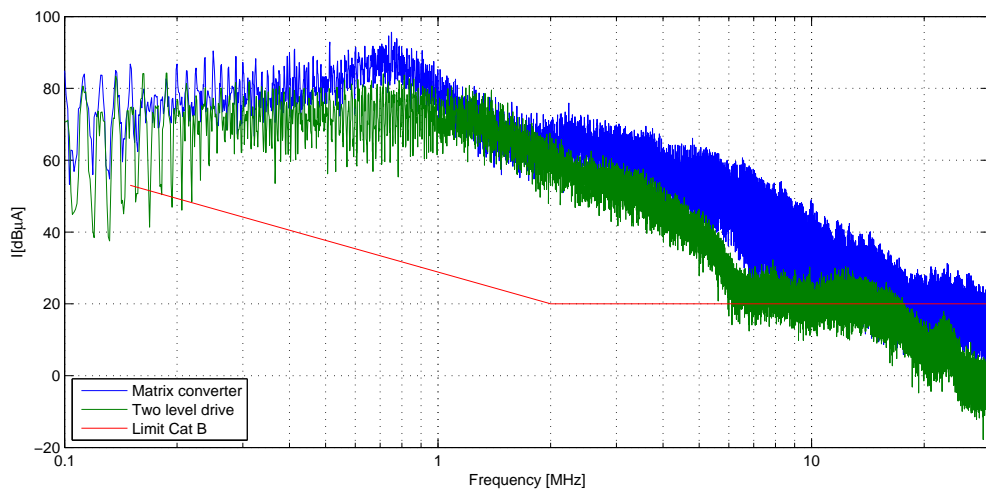


Figure 5.18: Input CM EMI comparison for Matrix and Two-level converters

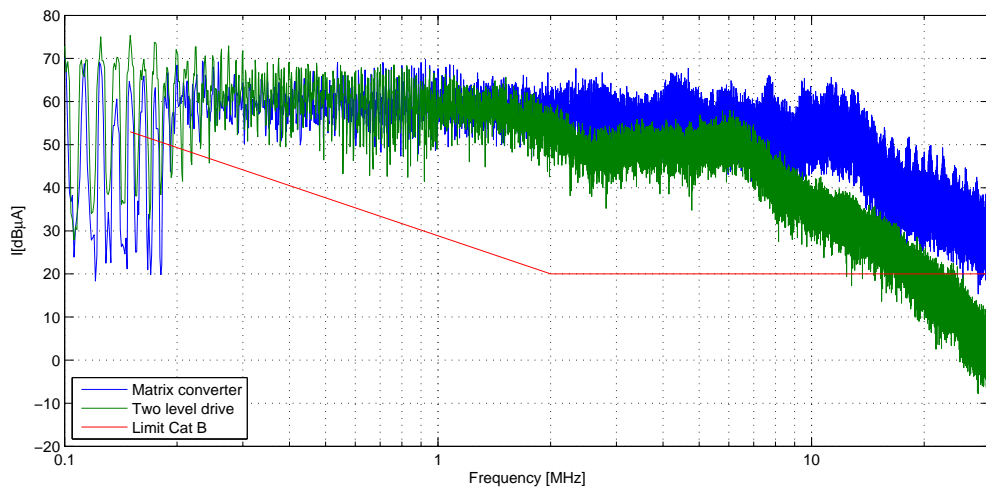


Figure 5.19: Output DM EMI comparison for Matrix and Two-level converters

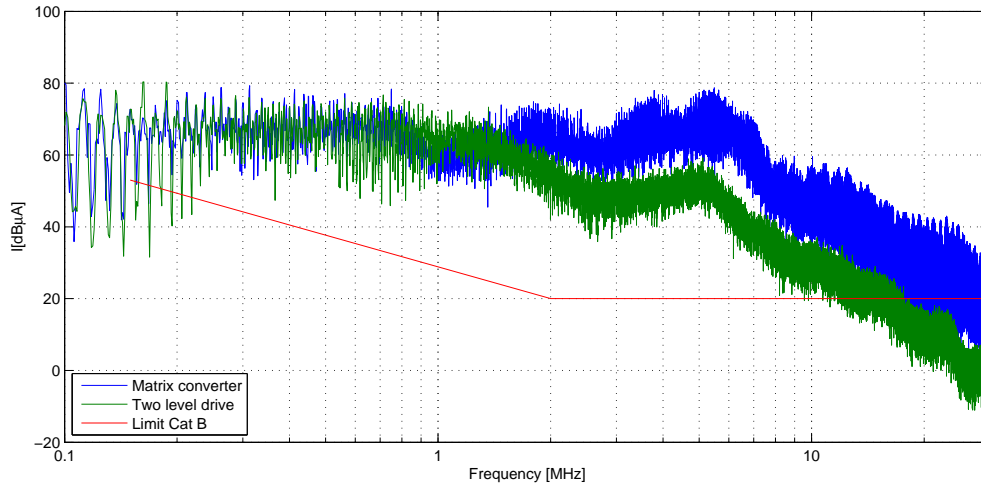


Figure 5.20: Output CM EMI comparison for Matrix and Two-level converters

Common mode voltage

Two more figures will be added, to fully represent the EMI measurements for the converter. A comparison of the common mode voltage will be reported for both converters, running with the same conditions as described before.

The common mode voltage is described as the voltage across the star point and the ground[50] and usually this, for a general balanced sinusoidal three phase load, it is zero. However, when a converter is added to the system, this is not true any more because of the coupling of the switched currents/voltages with the various parasitics in the system.

The two CM voltage measurements therefore has been measured and reported in 5.21 regarding the matrix converter and in 5.22 for the two level converter.

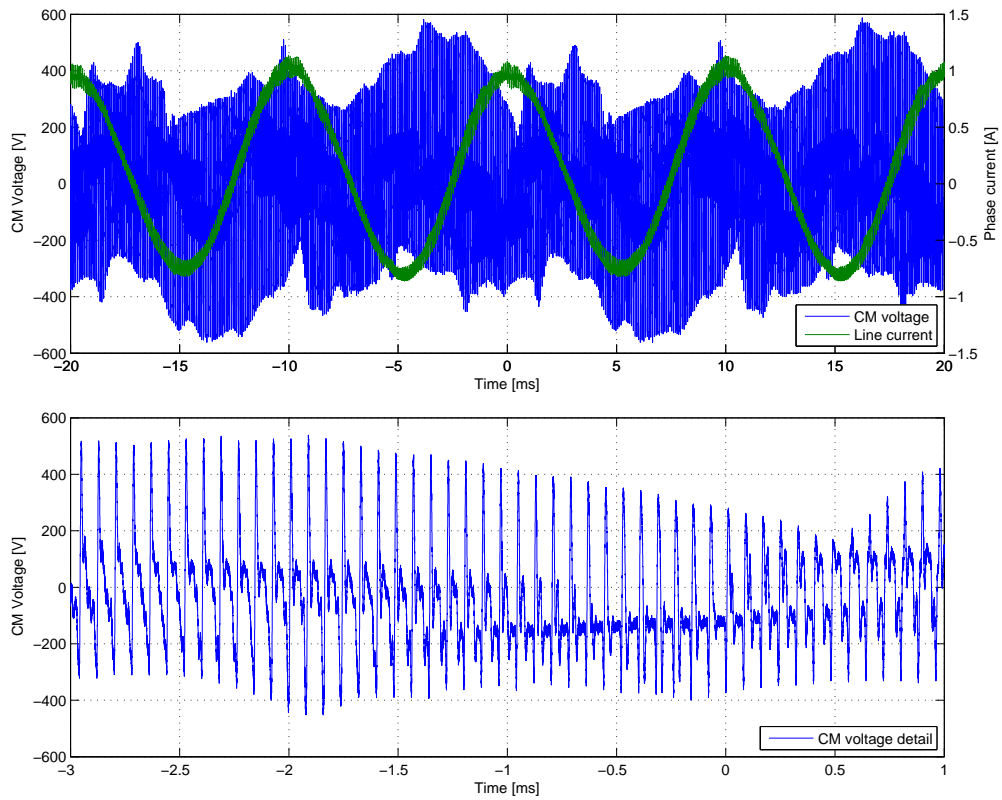


Figure 5.21: CM Voltage measurement for Matrix converter

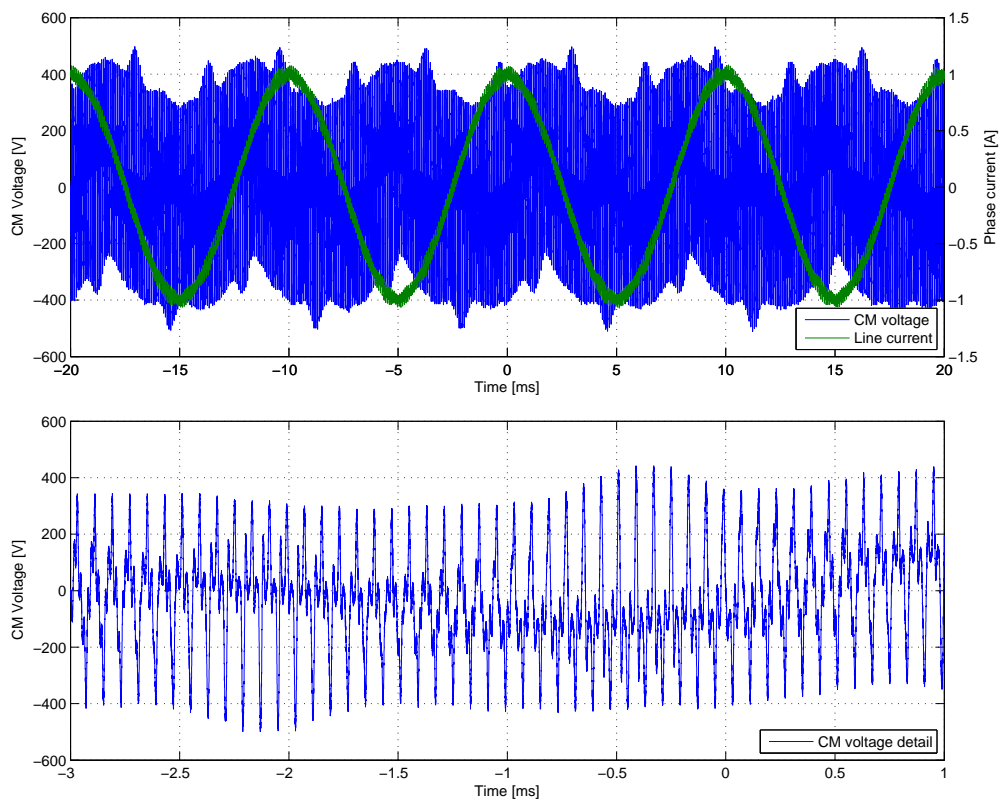


Figure 5.22: CM Voltage measurement for Two-level converter

Simulations of input and output system EMI

6.1 Introduction

This chapter will describe the simulation tools used for the system EMI prediction, starting with a brief description on how to create an external library file (DLL) to be used within Saber Simulator allowing to directly employ the DSP C code. A second paragraph will deal with a test procedure used to validate the simulations against spectrum analyser measurements, comparing the measurement and the simulation of the spectrum of a canonical saw tooth reference signal. Some simplified models have been tested to predict the emissions as in [51, 52], but the results were not satisfactory; therefore full simulations in the time-domain have been preferred. Description of the various models created for the time-domain simulations used to estimate the EM emissions will follow, for both the Matrix converter and the IM, input and output interferences. The results will then be compared with the actual measurements obtained in the previous chapter, to prove the validity of the used models.

6.2 Implementation of Matrix converter Modulation in Saber simulator

The chosen simulation tool is Saber because it allows more detailed component's parametrization compared to other circuit simulators, like Simulink or PSpice; so a circuit model has been created for the power components in the Saber environment, where the switches are triggered by a control block. To simulate accurately the behaviour of the Matrix converter cyclic Venturini modulation technique used within the DSP in

the practical rig (described in section 2.3) and possibly reduce the simulation time, a particular feature of Saber has been used: an external DLL (Dynamic Link Library) has been created in C Language and embedded within the simulation, to control the IGBTs. Usually the native Saber MAST language is used for the simulations, but that would mean to completely re-write the whole code written for the experimental DSP controller again for the simulator as well. Furthermore that code, because it would be in MAST language, before being executed will have to be interpreted by the simulator, and this process implies more effort for the processor, hence a longer simulation time. The DLL approach, instead, will provide a compiled "ready to use" code, which is thus more time efficient because it will be already in machine-language, directly executable by the CPU. The controller's code, as it was written for the DSP, has been compiled in such DLL with just few modifications for the interface with the simulator. The modifications in the C code, are reported in the following:

- The inclusion of saber's header file, `saberApi.h`, that defines all the communication variables between the library and the simulator.
- The definition of all the input/output variables with the pre-defined variables `in[]` and `out[]`, for example `#define time inp[0]` will declare that the first parameter passed from the simulator will be the simulation time.
- The routine has been declared as such: `SABER_FOREIGN_ROUTINE(VENTREAL) {...` all in uppercase, where the name "Ventreal" is the name of the DLL file.

Apart from these amendments, the rest can be copy-pasted directly out of the modulation DSP's source code straight into the C code to be compiled to obtain the final DLL file; this code is included in Appendix B.1.

To use it within the MAST code of the converter's, the declaration for the external DLL must be stated as such: `"foreign ventreal"` and will be used as a function. In the case of this work the following line is used to invoke the external library:

```
(T11,T12,T21,T22,T31,T32) = ventreal(time, V(VA), V(VB), V(VC),
                                V(Vra), V(Vrb), V(Vrc), q)
```

It is clear to understand which are the input variables: the simulation time "time", the input voltages "V(VA) V(VB) V(VC)", the reference for the output voltages "V(Vra) V(Vrb) V(Vrc)", and the last is the modulation index "q". The library, starting from these values, will calculate the timings for all the switches and then pass them back to the simulator. Fig. 6.1 shows a direct comparison between the Matrix converter output voltage simulated with such DLL and the output experimentally measured. The input voltage is the standard mains, 230V at 50Hz, and the output frequency is set at 100Hz.

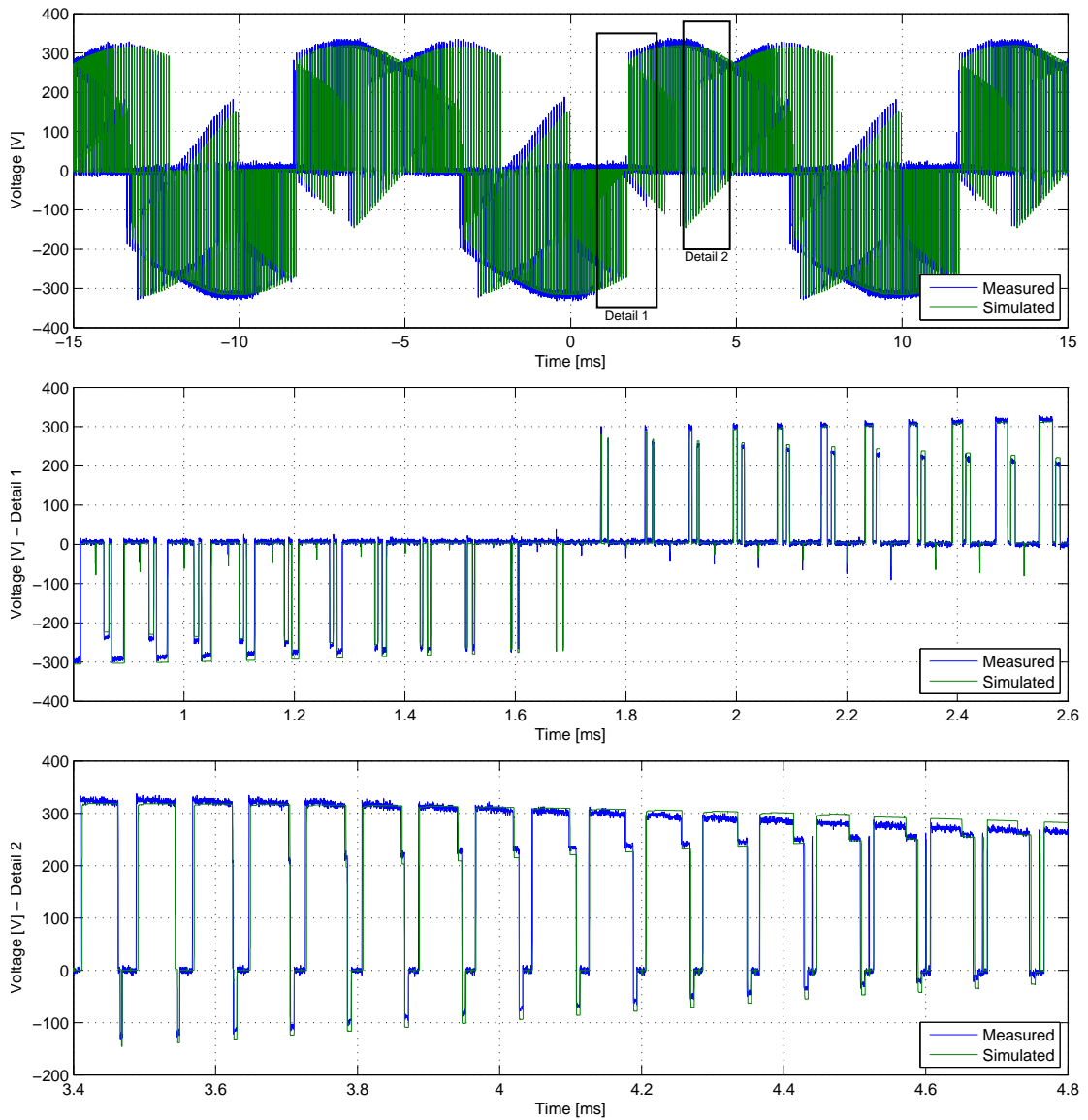


Figure 6.1: Output V_{ab} simulation/measurement comparison

It is possible to see that the figure contains three periods of the output voltage. There are two magnifications of different parts of the full waveform to highlight the good matching between the two curves.

The complete code of the MAST script to use the DLL within Saber is illustrated in the Appendix B.2.

6.3 Saber frequency analysis validation

This validation can be achieved by matching the Fourier transform obtained with Saber and the spectrum analyser measurement of a sample signal that has been acquired with

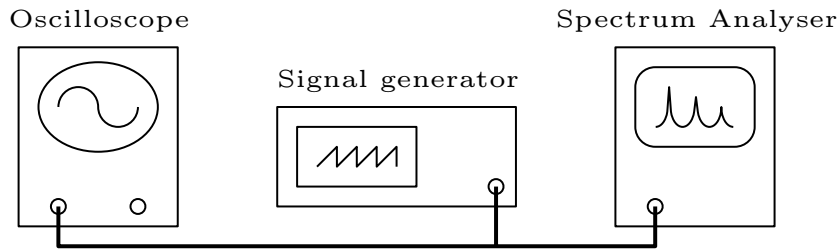


Figure 6.2: Experimental setup for spectrum measurements validation

both methods and then compared. A sawtooth signal at 500kHz has been used for this aim with the load provided by the internal 50Ω input impedance of the spectrum analyser; a digital oscilloscope with high sampling rate to save the input signal in the time domain was connected in parallel. This experimental setup is depicted in Fig. 6.2. The recorded signal has been exported and successively used as a voltage source for a time transient simulation in Saber, where the Saber FFT operator have been successively applied. This signal and the one saved with the spectrum analyser are compared in Fig. 6.3, after a scaling function had been applied to the FFT signal to make it consistent with the one of the spectrum:

$$V[dB\mu V] = 20 \cdot \log_{10}(V[V]) + 120 - 3 \quad (6.3.1)$$

This formula relates the voltage simulation's values, expressed in V , to the measured one that are expressed in $dB\mu V$: it calculates the values in dB, then it adds the 120 term to match the μV scale ($120 = 20 \cdot \log_{10}(1000)$), and finally it removes the 3dB term to match the rms value measured (this is because the FFT operator will provide the peak value). In Fig. 6.3 it is possible to see the matching of the peaks in the spectrum of the two signals, the one measured and the one simulated, for the fundamental (500kHz) and few harmonics.

6.4 LF motor model

To simulate the whole drive system and check if the system normal operation and stability is ensured once the filter is applied, a LF model for the motor is also needed. To simplify the circuit and speed-up the simulation a simple RL circuit has been chosen, since no speed or position control are implemented, we need now to estimate the values of R and L that better represents the current dynamics of the motor in the experimental rig. To do so a sinusoidal voltage at 100Hz and $168V_{rms}$, generated with a programmable power supply (Chroma 61511, 12kVA 15Hz-1.5kHz three-phase output), has been applied to the IM motor to simulate the converter's output, and stator

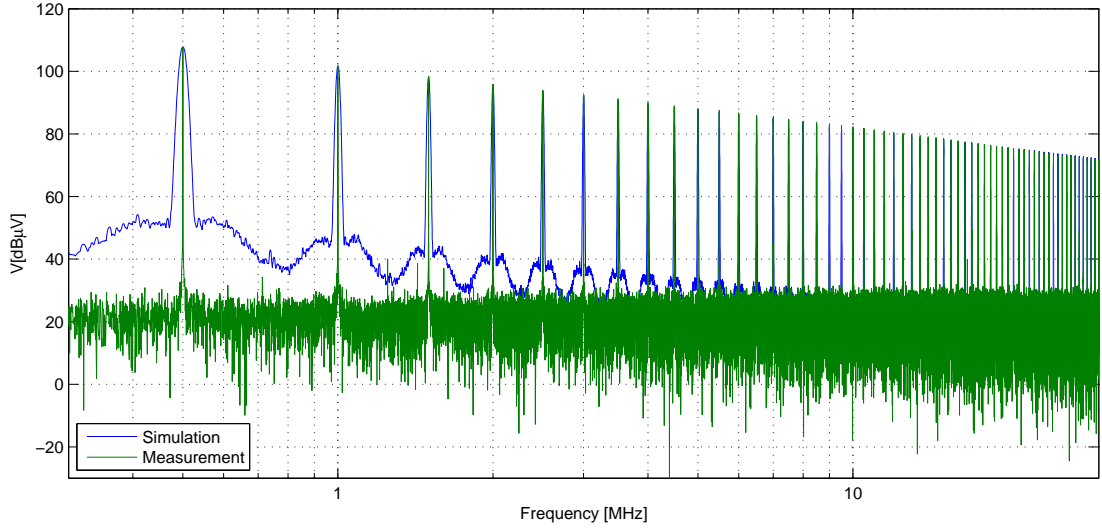


Figure 6.3: Output V_{ab} simulation/measurement comparison

voltage and current have been measured (Fig. 6.4 shows the measurements on phase a). Applying the FFT operator to the sampled values measured with a scope (WavePro 715Zi sampling 500ms at 500kHz), the amplitude of the fundamental frequency with its phase has been obtained. The model's R/L parameters can be obtained from the measured amplitudes:

$$R_L = \frac{|V|}{|I|} \cdot \cos(\phi_V - \phi_I) \quad (6.4.1)$$

$$X_L = \frac{|V|}{|I|} \cdot \sin(\phi_V - \phi_I) \quad (6.4.2)$$

In order to double check the phase offset between the two current and voltage signals, the cross-correlation operator has been used. This operator is proportional to the overlapping between the two signals and, for real values, it is expressed by the formula 6.4.3.

$$c(m) = \sum_{n=0}^{N-m-1} x_{n+m}y_n, \quad m = -2N + 1 \dots 2N - 1 \quad (6.4.3)$$

The output is a vector as long as the sum of the lengths of the two input signals, voltage and current in this case, and its peaks are located when the two signal match the most. Since both voltage and current are sine waves, the peaks will be periodic, and peak when the two signals are exactly in phase; this can be seen in Fig. 6.5. At the positive peak the overlapping is at the maximum, so to obtain the phase offset the time shift m must simply be divided by the periodicity of the signal and multiplied by 2π . The values obtained with both methods are compared and contrasted in Table 6.1, where we can observe the reliability of the measurements.

	FFT		Cross-correlation	
	R ($m\Omega$)	L (mH)	R ($m\Omega$)	L (mH)
Phase a	73.58	406.5	73.51	406.5
Phase b	66.47	403.8	66.181	403.9
Phase c	70.72	409.2	70.84	409.1

Table 6.1: Comparison of LF motor parameters obtained with FFT and correlation

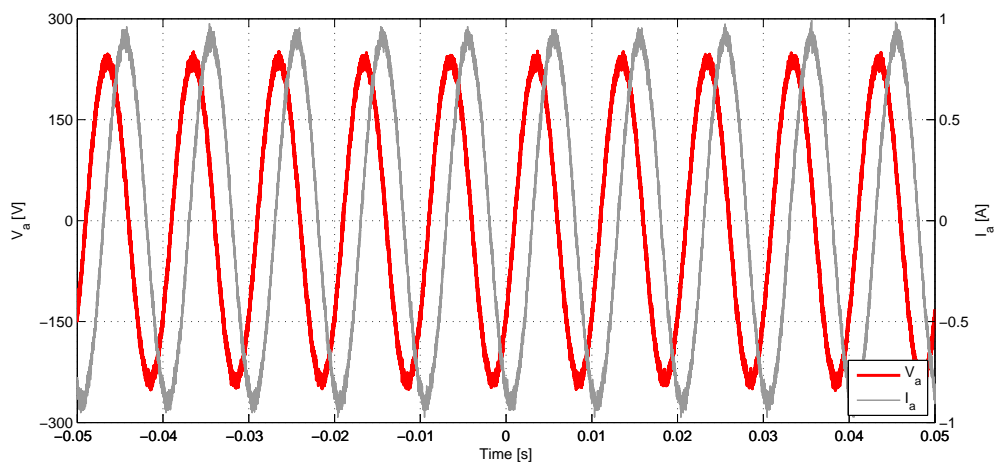


Figure 6.4: Measured voltage and current at the motor

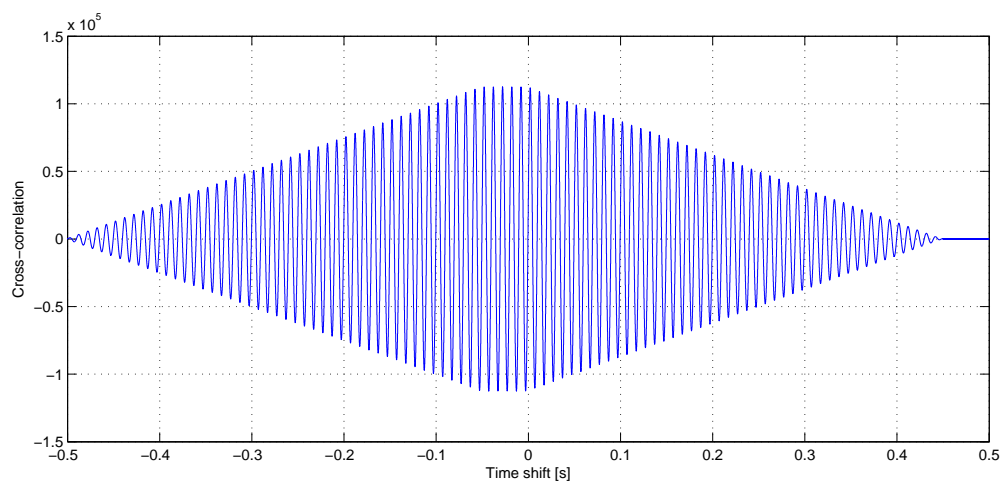


Figure 6.5: Cross-correlation between voltage and current

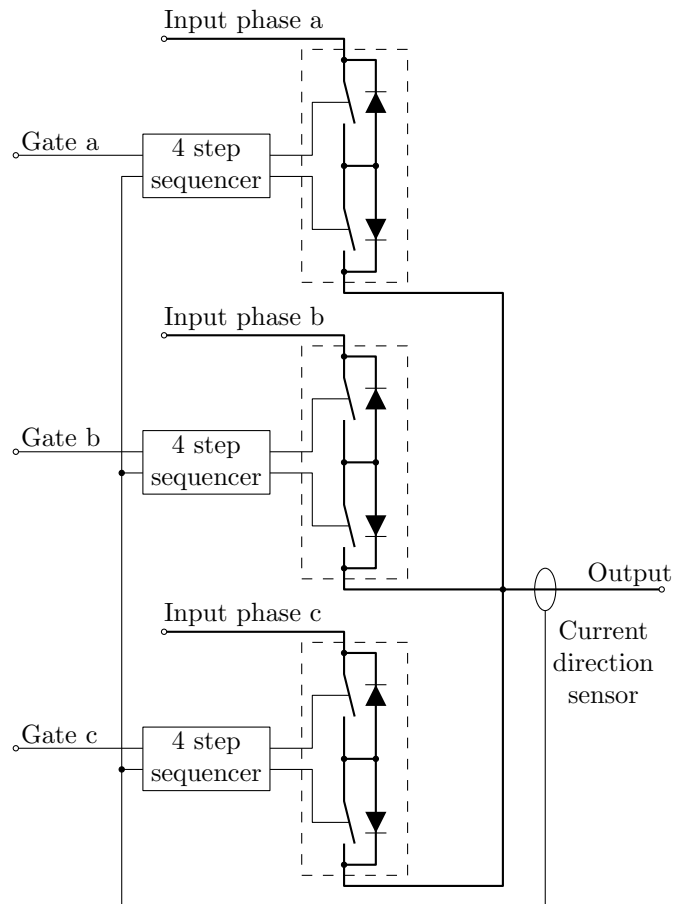


Figure 6.6: Matrix ideal switch model for one output phase

6.5 Complete Matrix converter drive HF model

For the time domain simulation all the developed HF models have been placed and composed in the final model, Fig. 6.7, starting from the LISN, then the input cable, the matrix converter, the output cable and the motor. To model the matrix converter circuit, for each output phase ideal switches have been used as represented in Fig. 6.6, while the parasitics have been grouped in the two sub-circuits *MtrxIn* and *MtrxOut* using the models already introduced in Fig. 4.11 and 4.12. These two blocks have been modelled to match the actual impedance measurements of the converter taken on both sides, when the IGBTs are open.

Fig. 6.7 shows the complete Matrix converter drive model, created within Saber simulator. In this complete model it is also visible a block for the input filter (ETS N1825) as well, because it is part of the experimental setup needed for the measurements; therefore this last component has been included too. It is a simple LC filter, whose parameters are given in the datasheet (Fig. 6.8). The last component is an inductor of 30nH

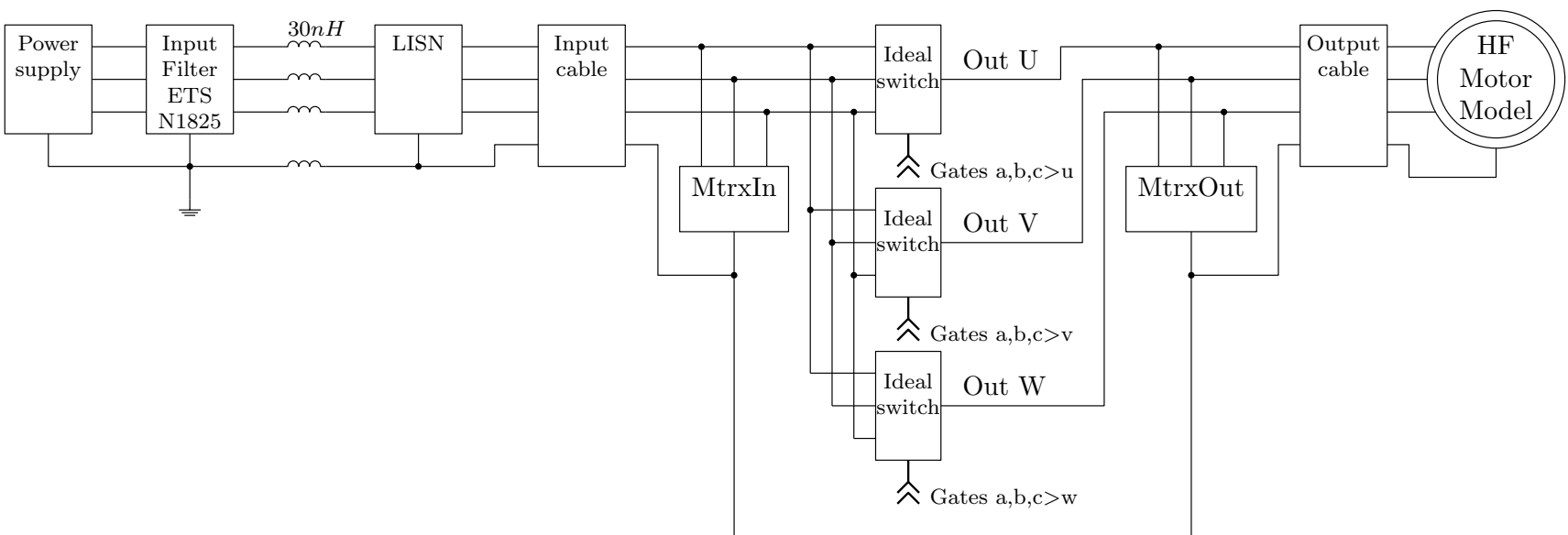


Figure 6.7: Complete HF model

Electrical Specifications

PART #	Current Max	# of Lines	Voltage drop on full load/line	DC resistance per line	Total series inductance/line	Total shunt capacitance/line	Case temp. rise on full load	Max. recommended case temp. on full load	Full load dissipation
N1820	6 amps	2	1 V	100 mΩ	1680 μH	1.5 μF	+10 °C	+70 °C	12 W
N1821	6 amps	4	1 V	100 mΩ	1680 μH	1.5 μF	+10 °C	+70 °C	24 W
N1822	32 amps	2	0.4 V	15 mΩ	177 μH	8.5 μF	+12 °C	+70 °C	100 W
N1823	32 amps	4	0.4 V	15 mΩ	177 μH	8.5 μF	+12 °C	+70 °C	200 W
N1824	63 amps	2	0.3 V	3 mΩ	25.5 μH	8.5 μF	+12 °C	+70 °C	60 W
N1825	63 amps	4	0.3 V	3 mΩ	25.5 μH	8.5 μF	+12 °C	+70 °C	120 W
N1826	100 amps	2	0.5 V	2 mΩ	37 μH	8.5 μF	+25 °C	+70 °C	120 W
N1827	100 amps	4	0.5 V	2 mΩ	37 μH	8.5 μF	+25 °C	+70 °C	240 W

Voltage Frequency Max-
 2 Line Filters = 250 V- DC/50/60 Hz- 120 V-400 Hz
 4 Line Filters = 440/250 V- DC/50/60 Hz- 220/120 V- 400 Hz

Add TS to the end of the part number for 250 V with transient suppressors
 Add HVTS to the end of the part number for 400 V with transient suppressors

Figure 6.8: Datasheet of input filter ETS N1825

to represent the cable that goes from the filter to the lisen. This impedance is estimated using the 50nH/m figure given in [10].

Using this model it is possible to produce a time simulation generating the currents in time domain for every section of the circuit, which will be used for the emission's estimations.

6.6 Output EMI simulations

To estimate the output common mode EMI emission (CM) of the matrix converter the ground current on the motor cable has been taken into consideration. A time transient simulation has been performed and the FFT operator has been applied to 1ms of the simulation result, performed in an interval where the initial transient was over and the values assumed the periodic behaviour. The result is a vector of complex values, the size of which will be the same as the number of samples in the input data; the relationship between the used simulation length in seconds l_s and the number of point in which it will be subdivided n_{pt} versus the frequency step Δf and the maximum frequency of the calculated spectrum f_{max} are so calculated:

$$F_{max} = \frac{F_s}{2} \quad (6.6.1)$$

$$\Delta f = \frac{1}{l_s} \quad (6.6.2)$$

The formula 6.3.1 will have to be applied to the modulo of the obtained values in order to match the units of the simulations with the units of the emission measurements; the

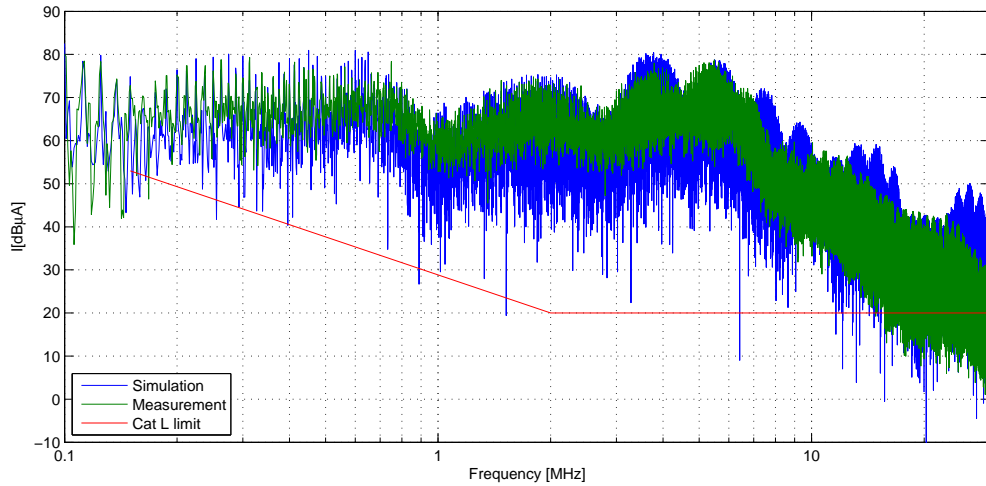


Figure 6.9: CM Conducted EMI, output

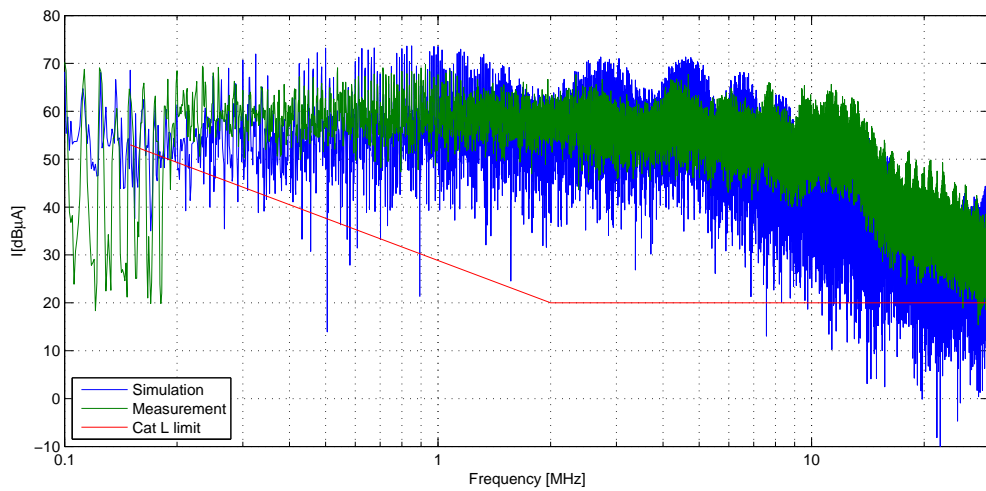


Figure 6.10: DM Conducted EMI, output

result can be seen in Fig. 6.9.

To correctly obtain the estimation of the differential mode emissions some algebra needs to be applied to the current measurements to remove the CM values. It simply mimics the configuration for the DM measurement: $I_{DM} = (2 \cdot I_a - I_b - I_c)/3$. This time dependent value is fed to the FFT to obtain the desired frequency-domain signal. Fig. 6.10 compares the simulations with the measurements. It can be observed that both CM and DM emissions are largely over the limits (red line) imposed by the relevant standards.

6.7 Input EMI simulations

To simulate the input currents the data generated in section 6.5 has again been used, with the same procedure as for the output, to generate the spectrum signal. Fig. 6.11 and 6.12 show the EMI emission at the input of the Matrix converter. Here there is a good match for the common mode experimental and simulated results; the differential mode though, presents a discrepancy in the range 0.5–2MHz where a mild resonant peak is observable in the experimental results. Various attempt have been made to create a more accurate DM model, removing for instance the CM components from the model, but it did not provide sufficiently good results.

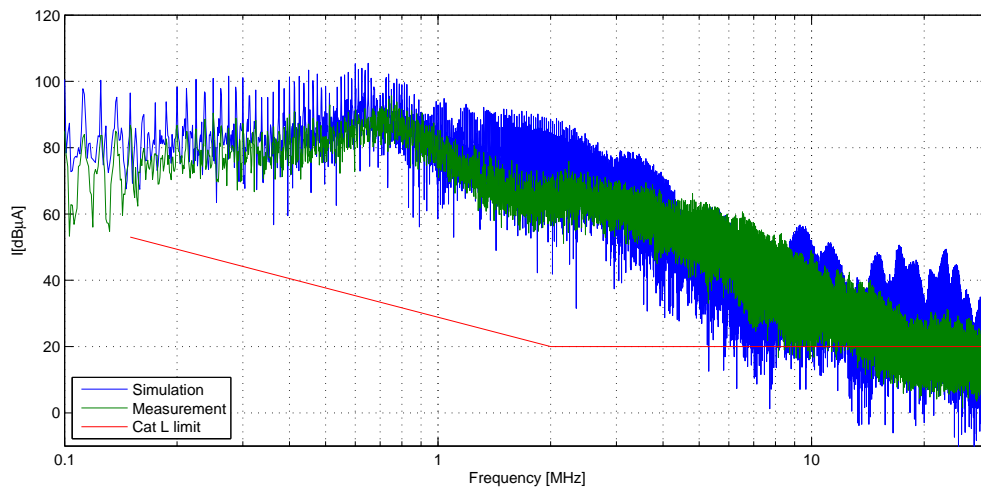


Figure 6.11: CM Conducted EMI, input

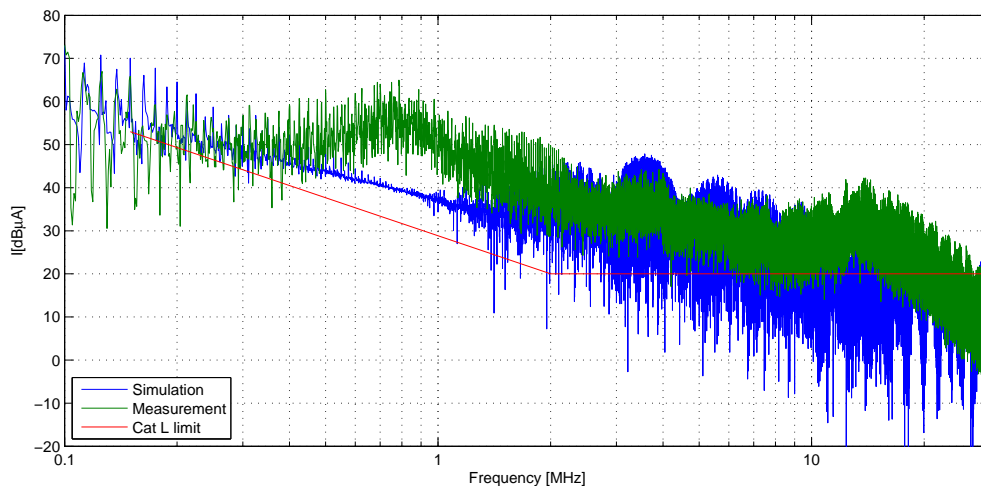


Figure 6.12: DM Conducted EMI, Input

Filter Design and realization

7.1 Introduction

This chapter will describe the design of the input and output EMI filters including the design methodology followed. This comprises: identifying the attenuation required at the frequencies of interest from the emission measurements, choose the filter topology and calculate the filter's components. The description will start with the output filter, suggesting at first a solution with ferrite inductors; however experimental measurements will show some flaws of this design and a final version with alloy cores will be illustrated. HF models for the components used will be proposed as well, showing a precise impedance matching with the experimental one. The last part will describe, with the same procedure, the input filter design that has just been parametrized and simulated.

7.2 Output filter: identification of the attenuation required

For the filter design the initial focus was on the output filter, where the emissions to be reduced can be seen in Chapter 5, Fig. 5.10 for the CM and 5.11 for the DM. The most common topologies to be employed for EMI filters are summarized in Table 7.1; among those, the chosen filter topology is a L configuration because it will minimize the capacitance toward ground, important detail for aircraft specifications, and will minimize the number of inductors, hence reducing the total weight of the filter, which is another important requirement for aircraft systems. Another reason to choose the L filter is the need to avoid capacitance directly connected to the output of the switches. In fact the presence of a capacitive load will cause a massive inrush current at every commutation, a condition absolutely to avoid. The filter design procedure, as in [9], is

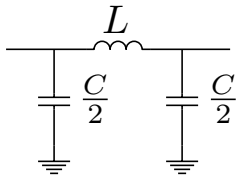
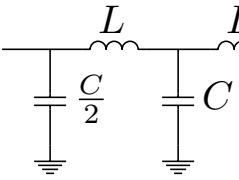
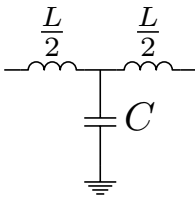
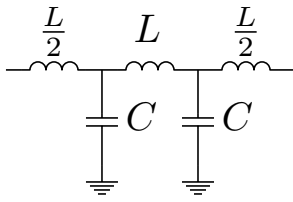
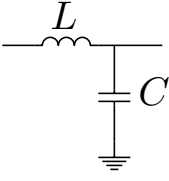
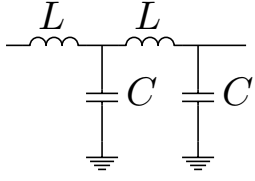
Type	Single Stage	Double stage
π	 <p>Attenuation = 60 dB/dec</p>	 <p>Attenuation = 100 dB/dec</p>
T	 <p>Attenuation = 60 dB/dec</p>	 <p>Attenuation = 100 dB/dec</p>
L	 <p>Attenuation = 40 dB/dec</p>	 <p>Attenuation = 80 dB/dec</p>

Table 7.1: Type of filters for EMI applications [9]

an iterative one: it starts identifying crucial points on the emission experimental measurements, i.e. those with higher emissions or the emissions at the lowest frequency. The relative attenuations Att and frequencies f_a are then collected. For each pair of points, for a given filter topology, it is possible to extrapolate the filter's cut-off frequency that will provide the required attenuation with the formula:

$$f_0 = \frac{f_a}{10^{\frac{Ad}{Att}}} \tag{7.2.1}$$

where Ad is the nominal attenuation for that particular filter.

The first step consists in designing the DM filter. Adding it to the system will attenuate part of the CM emissions too because it will intrinsically add some inductance on the common mode path; therefore the design of the CM filter needs to consider the inductors already present, in order to obtain the desired attenuation, thus saving size and weight.

Table 7.2 reports a list of frequencies chosen on the measured EM emission graph, with the relative attenuation to bring the emissions below the limits imposed by the

Frequency [kHz]	Attenuation required [dB]	Resulting f_0 [kHz]
200	25	47
250	28	50
400	30	71
1000	40	100
2500	50	141

Table 7.2: Attenuation for crucial points in DM output emissions

standards in the whole range of interest of frequency. The third column reports the calculated required cut-off frequency for a single stage L filter (40dB/dec) using the expression in 7.2.1. It is clear that the more demanding case is at 200kHz where the filter cut-off frequency is needed to be at 47kHz. If this frequency happened to be too low (hence the need of an excessively big inductor or capacitor, each other related by the expression 7.2.2), the filter choice would have been a double stage L filter, with 80 dB/dec of attenuation, leading to a less demanding cut-off frequency.

$$f_0 = \frac{1}{2\pi\sqrt{L \cdot C}} \quad (7.2.2)$$

Once the filter type and its cut-off frequency have been determined, a crude estimation for the filtered emissions, assuming ideal conditions, is quite simple, and this calculation is graphically reported in Fig. 7.1, by just adding the 40dB/dec attenuation after the filter's resonance frequency. This simple procedure will provide an immediate visualization showing whether the filter will attenuate enough throughout the spectrum, to make sure there will be no peaks above the limits, otherwise it will have to be re-designed accordingly.

7.3 Design of filter components

In aircraft applications the capacitance values in filtering systems have some restrictions; for example the 787 power quality specification limits the total line-to-line capacitance for an EMI filter to be $5\mu F$, for power levels above 10kW, and the total line-to-ground capacitance to be $20nF$. A large capacitance can also unbalance the system if a substantial value is used on the output of a power converter with switching components. Considering this, for the DM filter the inductance has been chosen to be close to $1mH$ so as not to produce a significant voltage drop on it. Using this value with the expression 7.3.2 and rounding the capacitor to a commercial value, the figure of $10nF$ was found, leading to a final value for the inductance, with the equation 7.3.1 of $1.1mH$.

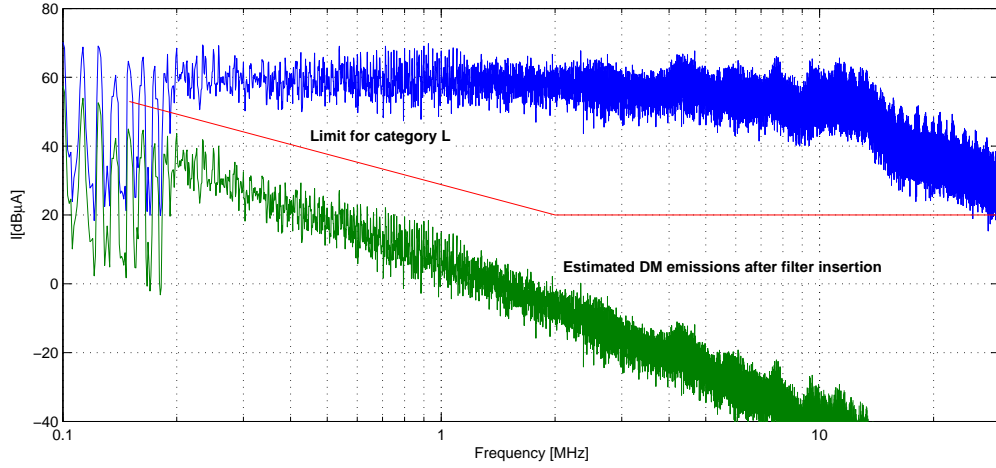


Figure 7.1: Output DM filter design

$$L = \frac{1}{(2\pi f_0)^2 \cdot C} \quad (7.3.1)$$

$$C = \frac{1}{(2\pi f_0)^2 \cdot L} \quad (7.3.2)$$

The filter so designed, however, presented some flaws that will later on be reported and the final filter design will be eventually described.

7.3.1 DM inductor design with Ferrites

To build the DM inductors the choice went initially for ferrite cores, because of their capabilities of handling high frequencies, and this section will provide the reasons and reference about their choice. Each manufacturer has several different materials specifically designed for EMI filtering; unfortunately these have proven not to be all easily obtainable as it may seem looking at catalogues. This is because distributors have only a limited set of materials and toroids available, and usually the available ones are not the best ones for an EMI application, but just the ones more requested for general application. Some attempts were made to obtain materials properly suited for high frequency, like Ferroxcube 3S4 cores, but the available size was not a fit for the needed current level and attenuation.

Having the restriction to choose only from off-the-shelf components that were available from distributors, a very narrow span of materials was therefore possible: it mainly consisted of N30 for Epcos, 3E27 for Ferroxcube and J material for Magnetics. Among these the worst is probably the Epcos 3E27, of which the permeability drops sharply just after 300kHz, that will not provide a sufficient attenuation for the high frequen-

cies. In Fig. 7.2 and 7.3 it is possible to see and compare the permeability of these materials.

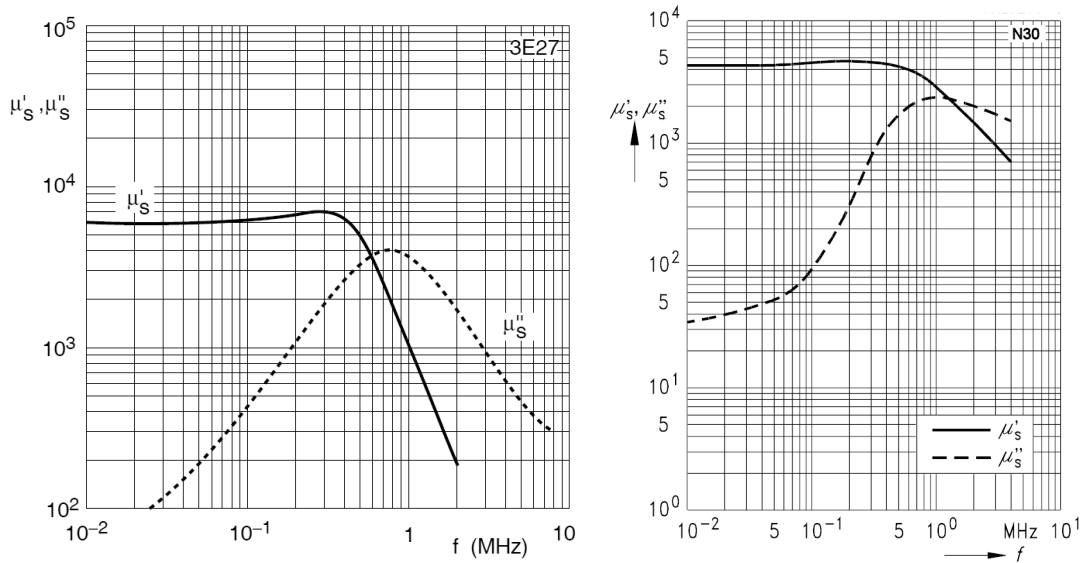


Figure 7.2: Permeability of Ferroxcube 3E27[5] and Epcos N30[6] materials

To design the inductors there are two main aspects to be taken under consideration: the Inductance factor A_l that will determine the number of turns needed to reach the desired inductance and the maximum magnetic field strength allowed before having saturation. Avoiding saturation in inductors is an important issue, if not observed the component inductance will drop significantly, thus losing the filtering capabilities. The allowed maximum field density changes from material to material, and it can be obtained from the relative datasheet on the B/H curve; in ferrites it varies significantly, for example for an EPCOS ferrite N30 its 100A/m (Fig. 7.4), for a N87 ferrite is 250A/m, for harder ferrites it can even be greater than 2000 A/m.

Because of the limited number of ferrites available, a collection of the data for the available ones was carried out to populate a table with the useful parameters, to guide the

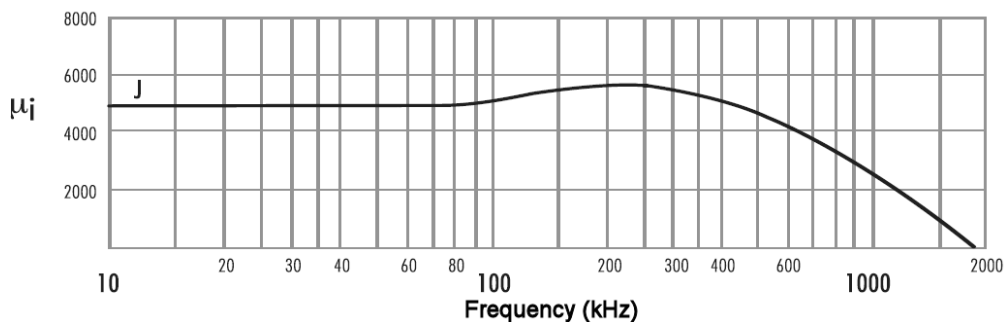


Figure 7.3: Permeability of Magnetics J material[7]

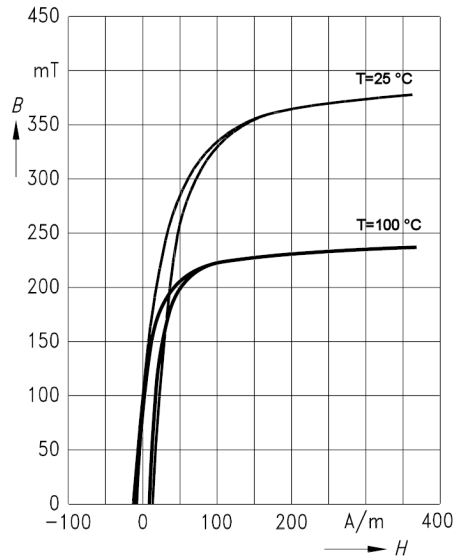


Figure 7.4: B/H curve for material N30[6]

choice of the best toroid, as reported in Table 7.3. To determine the maximum number of turns Ampere's circuital law has been used, combining the maximum magnetic field strength and the peak current as in Eq. 7.3.3.

Without loss of generality a peak current of 1A was assumed because it correspond to the peak current measured on the motor's phases, as can be seen in Fig. 6.4. The inductance value can simply be calculated with the formula 7.3.4, that uses the inductance factor and the number of turns.

$$N_{max} = \frac{H_{max} \cdot l_e}{I_{max}} \quad (7.3.3)$$

$$L = A_l \cdot N^2 \quad (7.3.4)$$

To locate the best choice for the toroid, a value close to the desired one has to be looked for on the last column; this will lead to identifying a core that is the lightest possible to realize the designed value, being the weight is one of the more critical parameters for aircraft applications.

The design of the DM filter requires an inductor of 1.1mH, so a Magnetics core ZJ-47313-TC has been chosen, with 12 turns.

7.3.2 DM filter Capacitors choice

The ideal choice for the capacitors in EMI filter application would be the feed-through type, because they present the lowest series resistance and inductance possible. How-

Code	Material	A_l [nH]	l_e [mm]	H_{max} [A/m]	N_{max}	L_{max} [μ H]
B64290L22X830	N30	5000	103	100	10	500
B64290L40X830	N30	5400	152.4	100	15	1215
B64290A84X830	N30	5500	255.3	100	25	3437
B64290L0659X830	N30	7000	96.29	100	9	567
TX55/32/18-3E27	3E27	10620	132	150	19	3833
TX80/40/15-3E27	3E27	11400	174	150	26	7706
TX63/38/25-3E27	3E27	13900	152	150	22	6727
0J49740TC	J	6955	381.5	79.5	30	6259
ZJ44925TC	J	7435	123	79.5	4	119
ZJ47313TC	J	8140	165	79.5	13	1375
0J49725TC	J	9346	259.31	79.5	20	3738

Table 7.3: List of toroids available with magnetic characteristics for $I_{peak}=1A$

ever, once again, obtaining these kind of components was extremely difficult: it is rare to find a manufacturer willing to sell just few of them, giving a long waiting time. Therefore another solution had to be found.

From a detailed literature survey it becomes clear that many EMI filtering solutions use X and Y type capacitors, as in [53] or [54] for example. This is a type of film capacitor that is a cheap and largely available substitute for the feed-through type, and is specifically designed to be used in line-to-line (X) or line-to-ground (Y) connections. Because these capacitors will be directly connected to line, they are exposed to over-voltages and transients that could damage them; for this reason they have to comply with requirements of several safety standards. EPCOS, that is one of the main producer of this type of capacitors, has collected some of these standards in [55], where it is clear that they need to sustain high voltage pulses so as to limit the risk of fire or electrical shock for the user. In more detail, X capacitors have lower voltage restrictions (up to 4kV) because a fault will be contained inside the device, instead the Y capacitor type has to withstand higher voltages (up to 8kV) because a fault could result in an electrical shock to the user. Furthermore, each X and Y category is sub-divided into classes: X1 to X3 and Y1 to Y4 respectively, according to the application where the peak values of surge values are less and less demanding. The chosen capacitor for the DM filter is a 10nF Y2 capacitor (Epcos B32022A3103M).

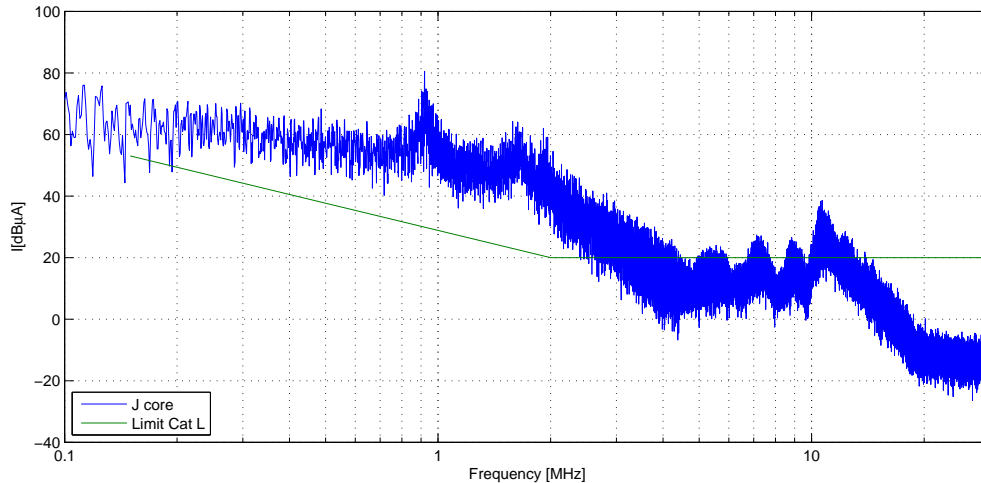


Figure 7.5: Emission with DM filter using J material

7.4 DM output filter implementation

The DM filter with the aforementioned components has been built according to the design methodology explained in section 7.3.1, however it presented immediately two critical issues. First of all, even if a certain amount of attenuation has been introduced by the filter, the DM output EMI, as shown in Fig. 7.5, still did not meet the standards limitation; furthermore the converter output current showed a clear indication of extreme distortion and presence of high frequency interference. After detailed investigation the problem was found in the ferrite toroid, that was not behaving as expected because the filter capacitors caused large current transients, that caused saturation on the cores with loss of their filtering capability. Therefore these inductors have been replaced by another type of inductor, made of an amorphous alloy, with roughly the same value (1.4mH) and the obtained output currents and DM emissions have been compared.

Fig. 7.6 shows the HF emissions of the same output current when the DM filter has the inductors made of the J ferrite and when they are made of the AMCC amorphous alloy. There is a clear lack of attenuation for the ferrites at high frequency, but what is more important, can be observed in Fig. 7.7 and 7.8. The output current waveform has peaks that are extremely high when the ferrite solution is adopted, indicating that it is not properly working, and this can be due only to saturation. Because of the advantages of the new adopted material, later described, the ferrites have been ruled out for the construction of the DM inductor.

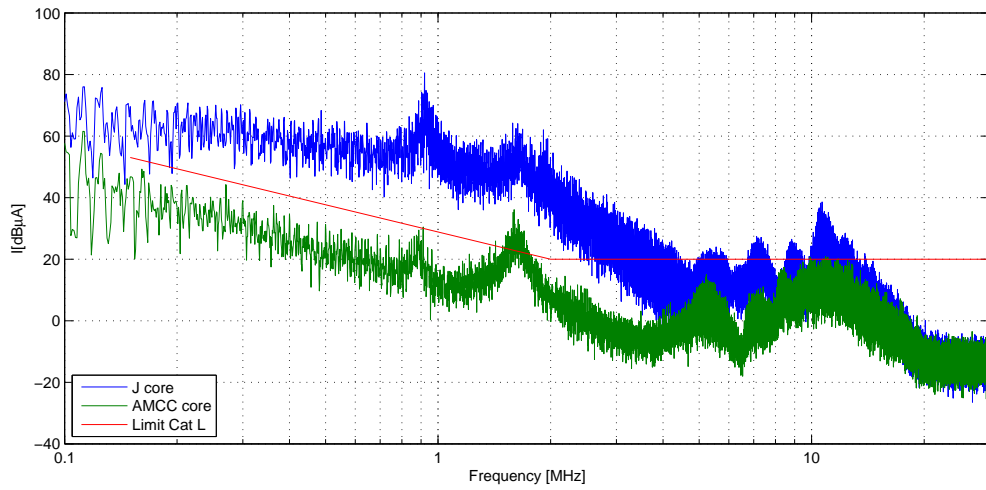


Figure 7.6: Comparison of DM emissions with filter made of J or AMCC material

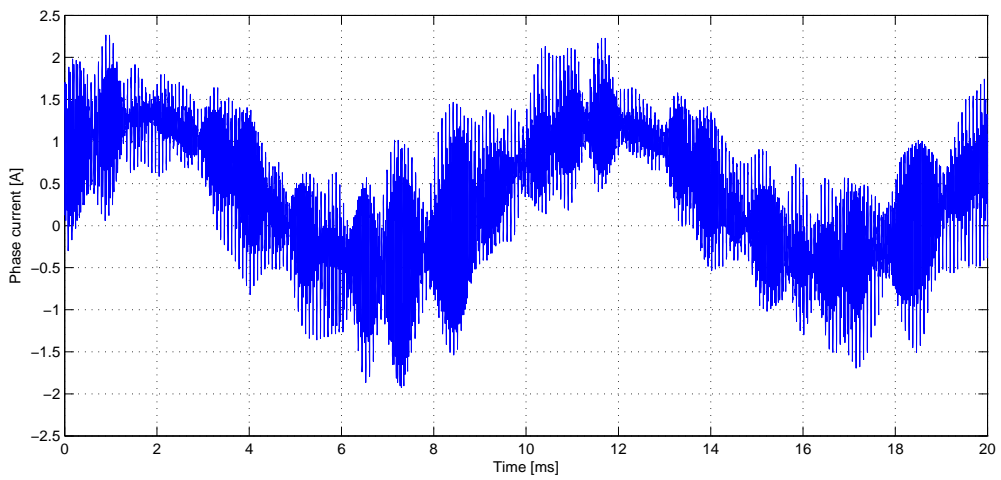


Figure 7.7: Output current after DM filter insertion, inductor with AMCC alloy

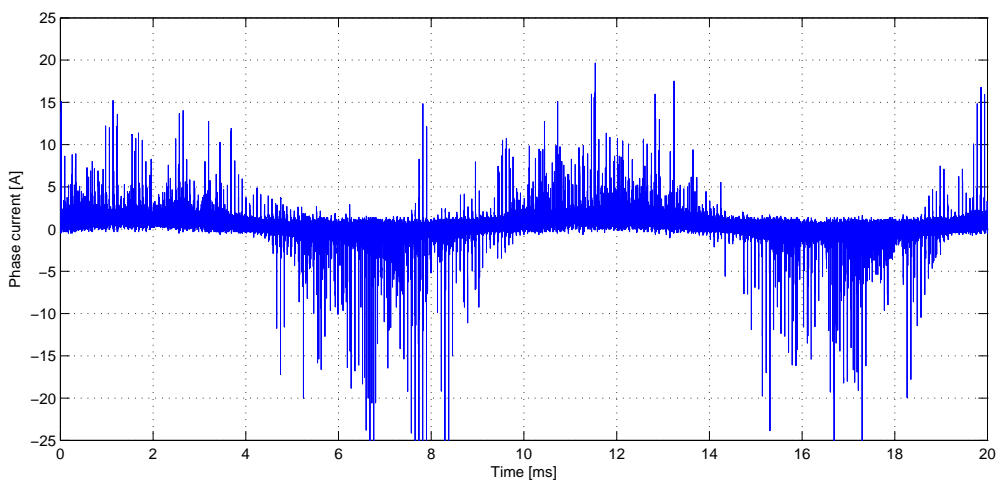


Figure 7.8: Output current after DM filter insertion, inductor with J ferrite

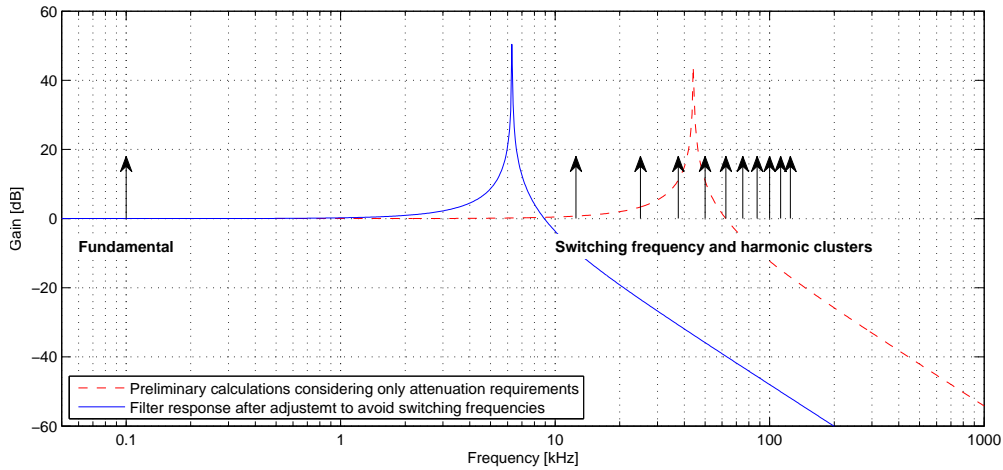


Figure 7.9: Bode plot of output DM filter

7.4.1 Frequency positioning of the DM filter resonance

Apart from the saturation in the ferrite core, that voids the effect of the inductor creating high spikes of current, there is another issue with the aforementioned filter: the dashed line in Fig. 7.9 illustrate the bode plot for its frequency response. It is visible from the positioning of the system's frequencies, in particular it is clear that the effect that the filter would have on the second and third harmonic clusters of the switching frequency: they will get a massive amplification. This would introduce a heavy resonating current on the output of the converter, causing stability problems and endangering the lifespan of the IGBT modules.

Therefore the resonance of the filter must be shifted to where it creates no harm, removing any harmonic into its high-gain band. The continuous line in Fig. 7.9 reports the frequency response of a new filter design with a resonance at 6.3kHz, and with the aforementioned design guidelines it has been built with an inductor of 9.4mH and a capacitor of 68nF.

7.4.2 Powerlite C material

The Powerlite C material[8] was the one used for the final DM inductor construction. It is produced by MetGlass, manufactured with iron based amorphous alloy. It consists of a stack of micro-thin ribbon of material, to reduce the losses, plus it can withstand higher temperatures, compared with ferrites: temperatures can reach 140 °C without any significant drop in the material permeability, as visible in Fig. 7.10.

The company provides a powerful design tool to properly realize the inductor: it certainly

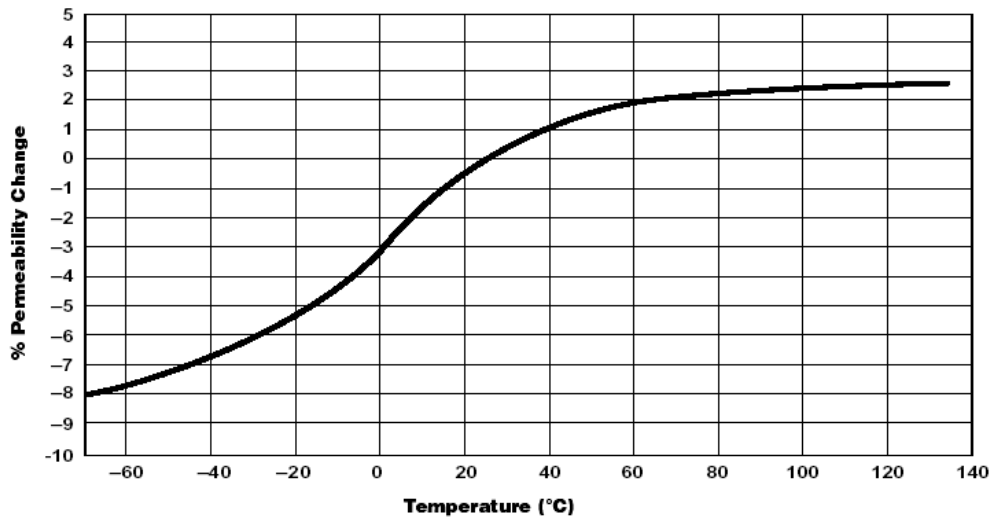


Figure 7.10: Permeability vs. Temperature for Powerlite C-cores[8]

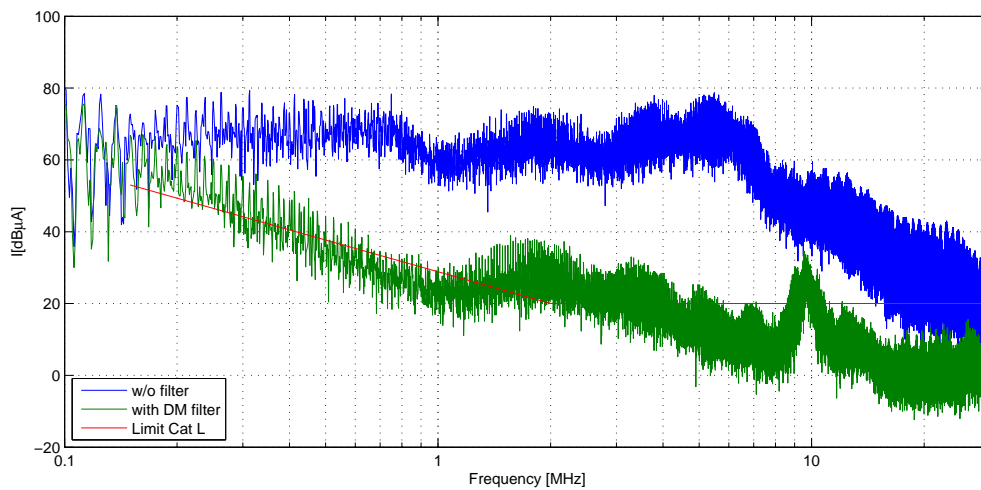


Figure 7.11: Output CM emissions after DM filter insertion

requires the desired inductance and peak current, but it is also able to fully consider harmonic content while calculating the losses to properly size the needed core. As regards the inductor winding, a solution for a single layer winding has been chosen, using both sides of the C core, to thus reduce to a minimum the parasitic inter-winding capacitance and allow the inductor to perform at the highest possible frequency. To reach the final inductance value, for practical convenience, two cores have been used and connected in series, AMCC 6.3 and AMCC 16A, producing finally the required inductance. The total weight for the cores was only 400g per phase.

Frequency [kHz]	Attenuation required [dB]	Resulting f_0 [kHz]
150	25	36
230	28	46
300	10	170

Table 7.4: Attenuation for crucial points in CM output emissions

7.5 CM output filter implementation

The DM filter, once inserted into the system, will provide on its own a CM inductance, that may or may not be enough to be used for the CM emissions filtering. The actual inductance that couples with the path of CM currents is the parallel of the three DM inductors, which is approximately 3mH. To see if this value will be enough, a CM filter design procedure has been followed, in the same way as for the DM filter. Table 7.4 represents the attenuation required according to standards for crucial frequency points in Fig. 5.10, considering 10dB margin. Considering 3mH for the inductance, using expression 7.3.2, and designing the filter to attenuate 25dB at 150kHz, the required capacitance is 6.7nF. Therefore a commercial value of 10nF was used, which is below the 20nF limit of the 787 power-quality standard. This capacitor has been connected in the central point of the three DM capacitors in order to limit the number of capacitors connected from line to ground and to keep the capacitance connected on the three phases as low as possible. The actual capacitance that the CM currents will cross is composed of the parallel of the three 68nF DM capacitors in series with the single 10nF CM capacitor and this value is actually 9.5nF. This because the CM capacitor is much smaller compared to the value of 204nF resulting from the parallel of the DM capacitors, so the actual DM capacitors will not affect much the total CM capacitance value. Other than the estimation method used in Fig. 7.1, the emissions can be estimated more accurately adding the actual Filter's frequency response, calculated with Matlab "tf" function for the actual values of L and C, to the emissions before the filter insertion. Fig. 7.12 represents the results obtained using this method compared with the actual emissions measured once the complete filter has been inserted in the circuit. It can be seen that the estimation is very accurate for frequencies up to 1MHz; after that limit the filter attenuation remains constant rather than keep rolling-off, with a resulting emission behaviour parallel to the original without filter, roughly 70dB lower.

As it is possible to notice in Fig. 7.13, the total output DM emissions after filter insertion presents a range of frequency around 10MHz in which a resonant peak still brings the EMI above the limit. To reduce the peak, some ferrite tubes made of material Fer-

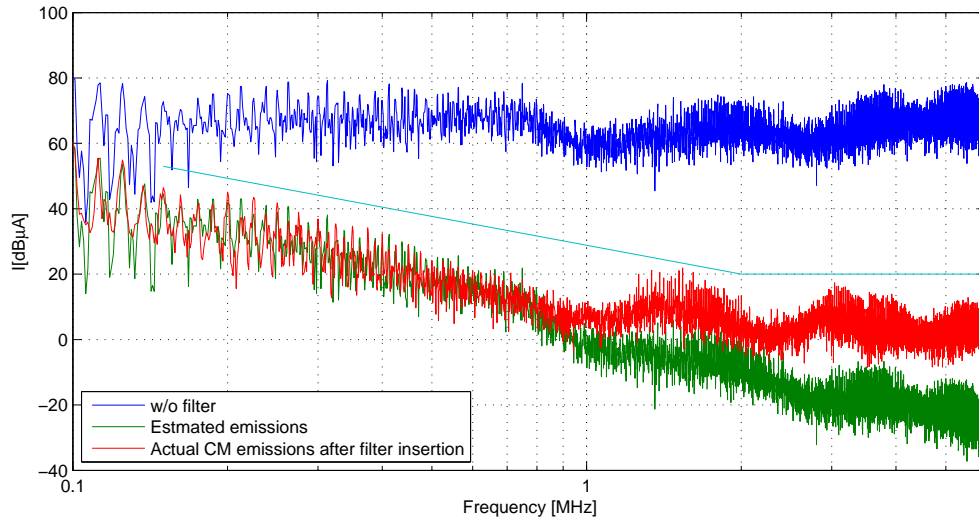


Figure 7.12: Output CM emissions after DM filter insertion

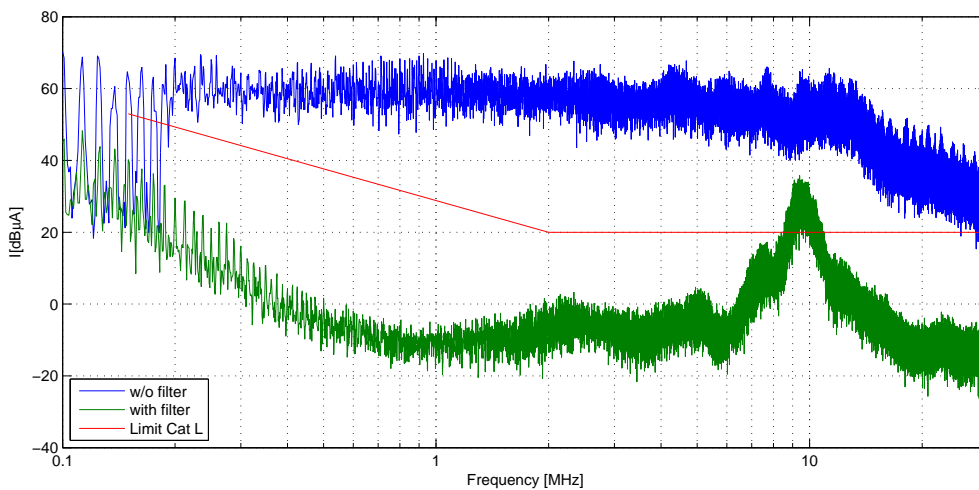


Figure 7.13: Output DM emissions after DM filter insertion

roxcube 3S4, a material designed to properly handle frequencies higher than 100 MHz, have been inserted on the output three-phase conductors; once again the saturation has been checked showing that only one turn was allowed. So two tubes CST 17/9.5/29-3S4 have been used for each phase for a DM configuration, plus a single one across all the conductors to reduce the CM emissions too.

The final schematic of the filter can be seen in Fig. 7.14, where the ferrite beads are highlighted, while Table 7.5 report the complete list of used components.

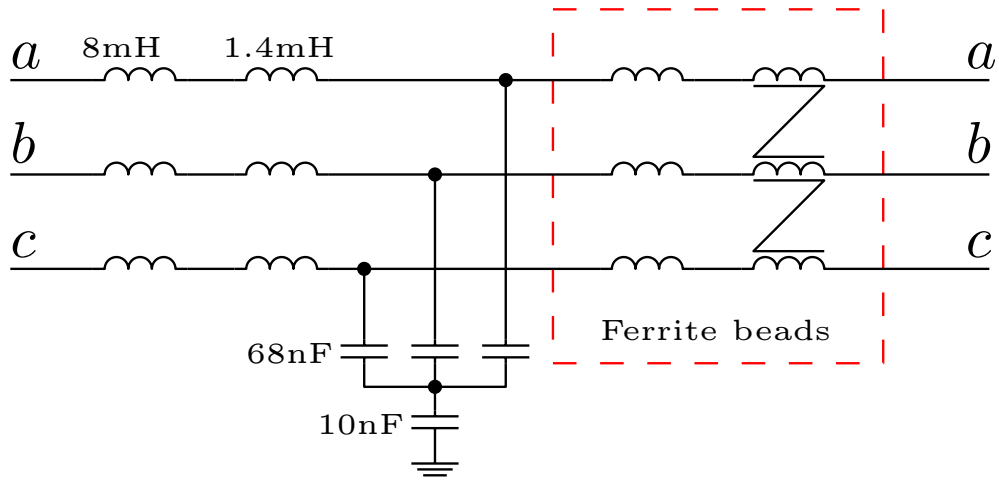


Figure 7.14: Schematic of the output filter

Differential Mode	3 × AMCC 6.3 (40 turns)	1.4mH
	3 × AMCC 16A (92 turns)	8mH
	3 × B32023A3683M	68nF
	6 × CST 17/9.5/29-3S4	
Common Mode	1 × B32022A3103M	10nF
	1 × CST 17/9.5/29-3S4	

Table 7.5: List of material for EMI output filter

7.6 HF Modelling the output filter

Once the actual inductors have been built, they have been modelled to create an HF component useful for simulations. Because the filter inductor has been experimentally implemented by means of two single inductors in series, starting from the model in [56], a final circuit model like the one in Fig. 7.15 has been used. The same parametrization procedure used for the other system's parts has been here used: a GA fitting of the simulation model to match the experimental impedance measurement. For the DM inductor the procedure is quite straightforward because the experimental impedance measurement needed for the model fitting is a simple measurement between the two terminals.

Once the real inductor was available and the filter implemented, proper HF modelling followed, giving for the model in Fig. 7.15 the values in Table 7.6. Figure 7.16 shows the matching for one inductor, while Figure 7.17 reports the magnitude of the impedance for all the three DM inductors. In the latter figure it is possible to see a difference in the impedance profile, this is due to two inevitable factors: the inaccuracies during the core fabrication process and the differences in thickness of the air-gap due to the manual assembly.

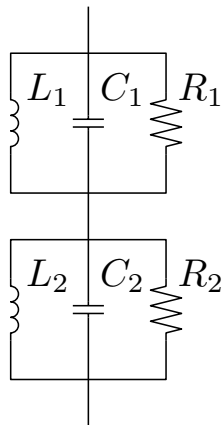


Figure 7.15: Inductor model

Parameter	Phase U	Phase V	Phase W
L1 [mH]	9.23	8.3	8.66
L2 [mH]	0.52	0.83	0.58
R1 [kΩ]	93	72	88
R2 [kΩ]	1.3	8.0	4.3
C1 [pF]	31.8	38.3	27.7
C2 [pF]	110	76.2	117

Table 7.6: Model parameters

Regarding the further inductive component of the output filter, the ferrite tubes, the impedance of the wire inside it has been measured. To obtain a HF simulation model of this impedance, after few trial and error attempts using different circuit topologies, the network as in Fig. 7.18 has been selected to better match the measured impedance. Table 7.7 reports the model parameters (obtained still with the same GA procedure) and Fig. 7.19 shows the impedance matching obtained with such model.

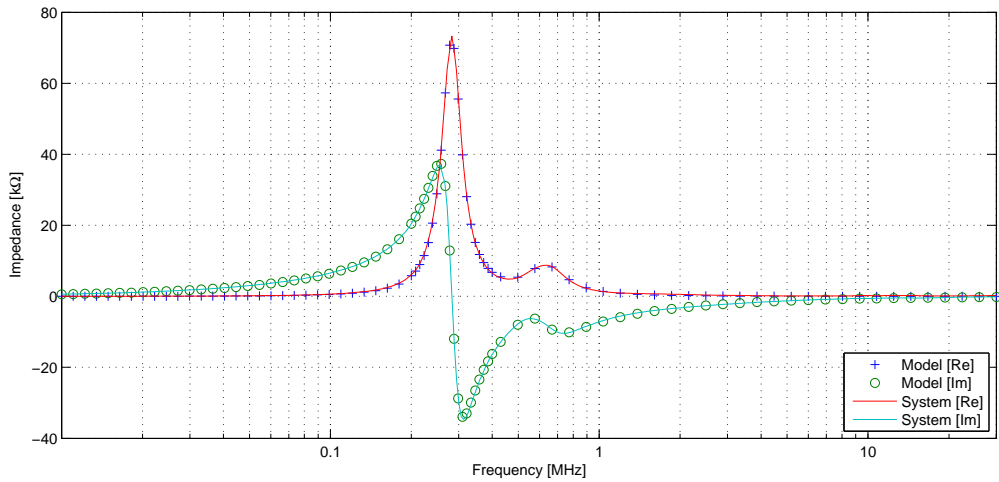


Figure 7.16: DM Inductor: matching of the measured and simulated impedance

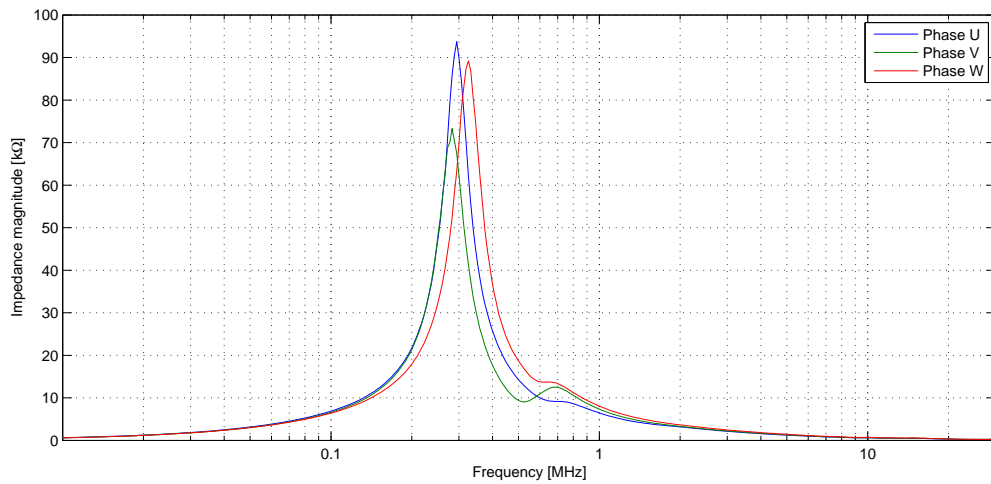


Figure 7.17: DM Inductor: matching of the measured and simulated impedance

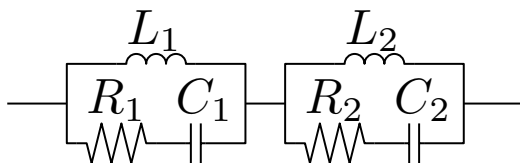


Figure 7.18: Ferrite tube model

Parameter	Value
L1 [μH]	4.71
L2 [μH]	0.55
R1 [Ω]	72
R2 [Ω]	123
C1 [μF]	355
C2 [μF]	110

Table 7.7: Model parameters

Once the inductors have been modelled it's the turn of the capacitors. They have a quite easy measured experimentally impedance to match, as it can be seen in Fig. 7.20 and 7.21. The model is just a capacitor in series to an inductor, and the values for the

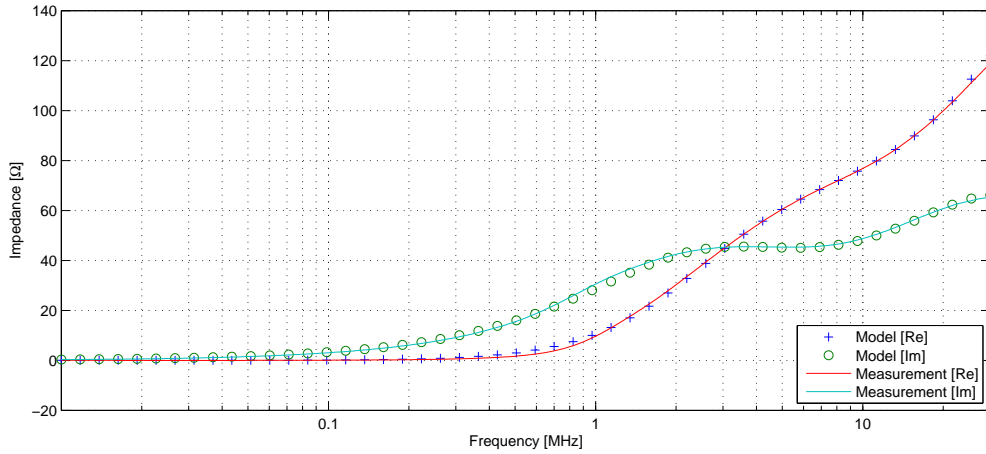


Figure 7.19: Ferrite tube: matching of the measured and simulated impedance

CM are $C = 10\text{nF}$ and $L = 23.7\text{nH}$, while for the DM they are $C = 64\text{nF}$ and $L = 21\text{nH}$, still obtained with the same procedure.

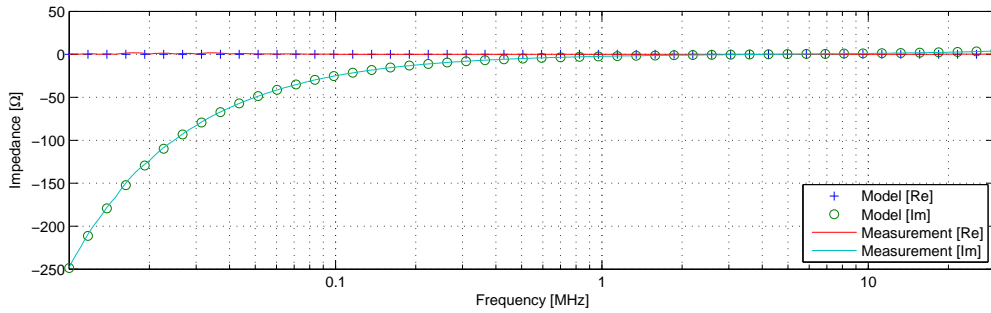


Figure 7.20: DM output filter: matching of the measured and simulated impedance

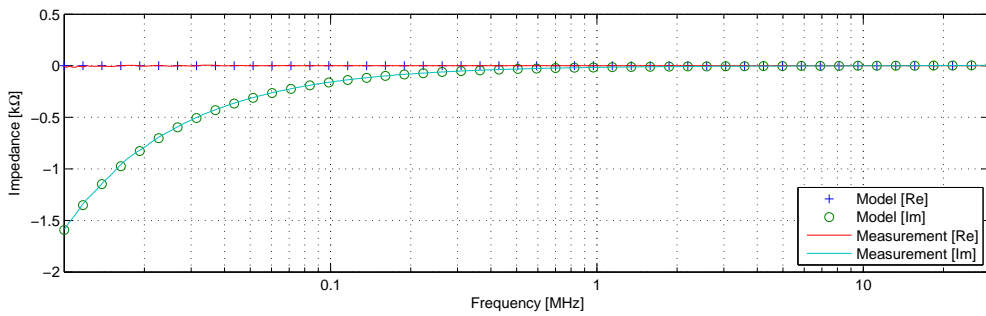


Figure 7.21: CM output filter: matching of the measured and simulated impedance

7.7 Input DM and CM filter design

Following the same procedure as for the output filter, the attenuation required at relevant frequencies by the input EMI filter can be identified from the measured emissions

Frequency [kHz]	Attenuation required [dB]	Resulting f_0 [kHz]
200	20	63
300	25	71
700	35	93
1000	35	133

Table 7.8: Attenuation for crucial points in DM input emissions

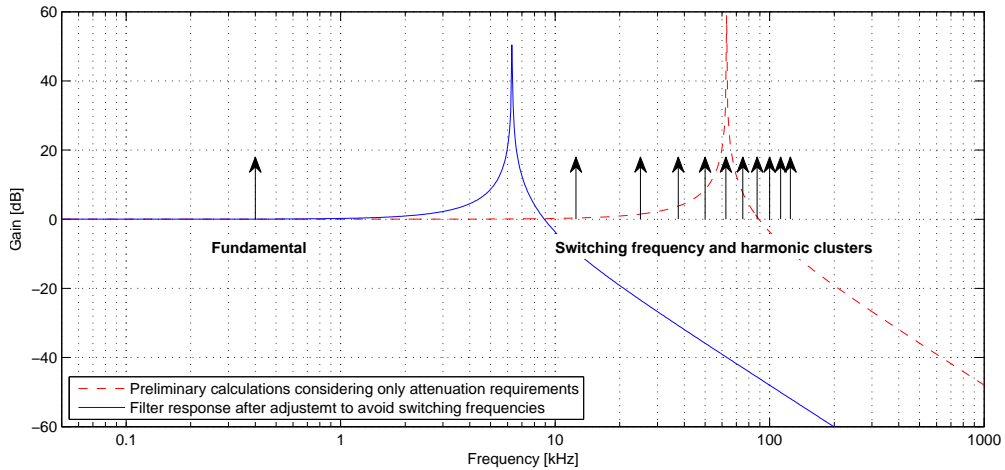


Figure 7.22: Bode plot of input DM filter

in Fig. 5.8 and 5.9. The same table, with these attenuations and resulting filter cut-off frequencies calculated again with expression 7.2.1, has been filled in for specific relevant frequencies, resulting in Table 7.8.

The filter resonance frequency has been chosen at 65kHz and once again, as it can be seen in Fig. 7.22, it falls between the 5th and 7th switching frequency harmonic clusters. This time, though, the fundamental frequency of 400Hz of the aircraft grid is much closer to the switching harmonic clusters, so more care must be taken when positioning the filter cut-off frequency as more switching harmonics can be easily amplified and could create problems this time too. Following the design guidelines used for the output filter, the same filter values can be used: 9.4mH for the inductors and 68nF for the capacitors. Fig. 7.23 emulates the insertion of the designed input DM filter by adding the filter response to the measured DM emissions, as it has been done in the previous chapter for the common mode output emissions, providing an indication on how the filter should perform. Because in the output filter emissions measurements it has been noted that the filter will not attenuate after roughly 1Mhz, this behaviour has been included in the calculations, keeping constant the attenuation for frequencies after that point, to provide a more accurate emissions estimation. This filter has not been

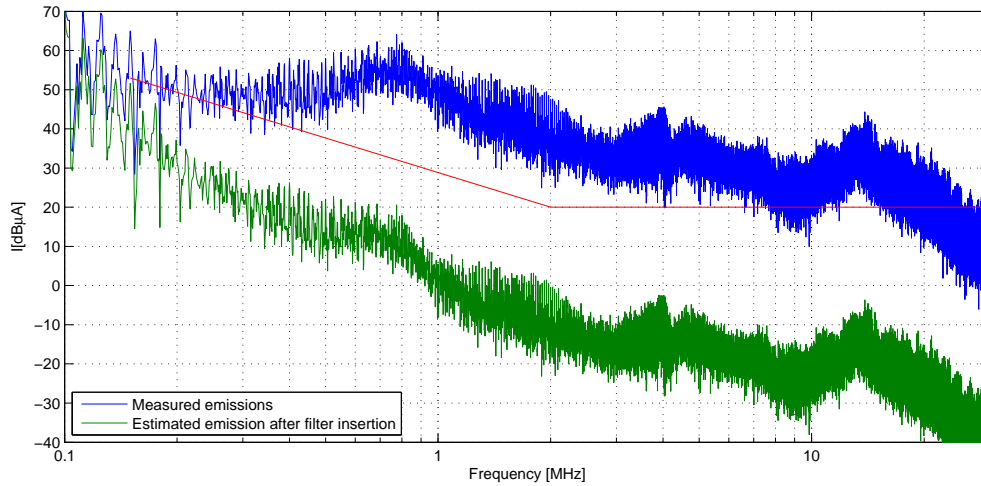


Figure 7.23: Input DM emissions estimation after DM filter insertion

Frequency [kHz]	Attenuation required [dB]	Resulting f_0 [kHz]
200	45	15
300	50	17
700	70	12
1000	65	24
2000	60	63

Table 7.9: Attenuation for crucial points in CM input emissions

implemented because of the limited time available, leaving this task for future developments. However the same procedure for the output filter can be followed, because the results are expected to be roughly the same.

For the input CM filter the attenuation required by the standards at the input emissions is larger compared to the one required for the output, as visible in Fig. 5.8; considering again the DM inductors to be included in the CM filter design, it is possible to populate the table in 7.9 with the frequencies, attenuation and capacitance required assuming a fixed value for the inductors. It is clear that 700kHz is the critical point, where the required attenuation is at its maximum, and the resulting required CM capacitor is 55nF. Again this value will be the result of the DM capacitors combined with the CM one. Using a 68nF capacitor connected on the central connection of the DM ones, the resulting total capacitance on the CM path would be 51nF. Considering the 10dB margin used while filling in the table for the attenuation requirements, this value is clearly acceptable, leading to the smallest capacitance value possible for a single stage CM filter.

Fig. 7.25 shows the schematic of the designed input filter, while Fig. 7.24 shows the expected input CM emissions after its insertion, demonstrating the filtering effectiveness.

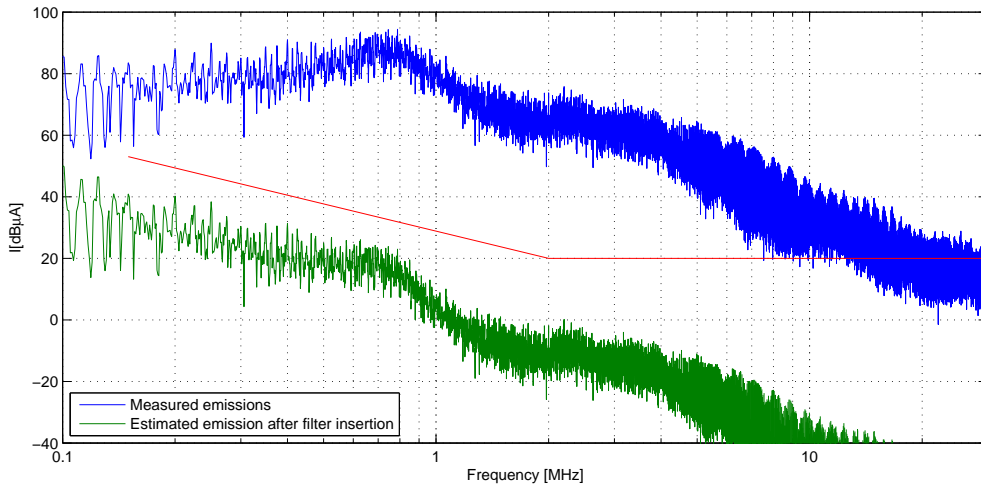


Figure 7.24: Input CM emissions estimation after filter insertion

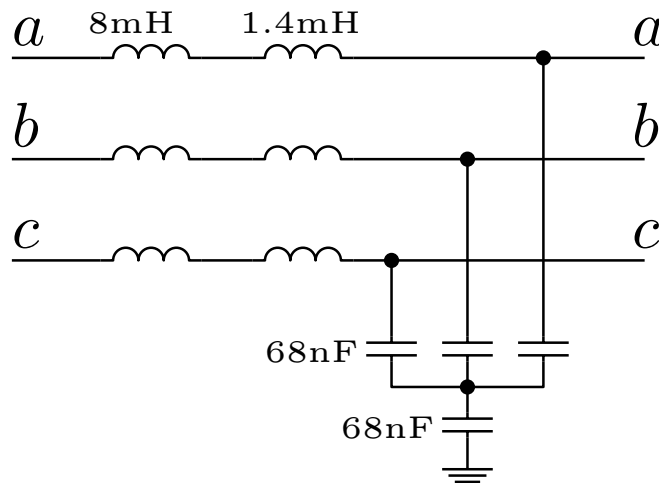


Figure 7.25: Schematic of the input filter

Filter realization and experimental results

8.1 Introduction

This last chapter shows and describes the final assembly of the output filter, providing the experimental layout followed by various experimental emission measurements to prove the effectiveness of the output EMI filtering. Different measurements for two running conditions supplying 50Hz and 100Hz output will be shown, comparing the emissions before and after the filter insertion to verify its attenuation; the experimental results will be provided not just for a standard aircraft supply at 115V and 400Hz but also for a standard grid supply at 240V and 50Hz.

8.2 Assembling the output filter

Given the chosen filter layout and parameters values designed in the previous chapter the output EMI filter has been built. The inductors have been manually wound in a single layer bobbin to minimize the parasitic capacitive coupling, using a 0.8mm diameter copper wire as suggested in the inductor code designer program. Regarding the two cores forming the global DM inductor (Fig. 7.14), the large one (AMCC 16A) allowed two bobbins of 45 turns, one on each side of the double C core; however the other one (AMCC 6.3), because of saturation, did not allow more than 40 turns, thus permitting the winding of just one side. After the two inductors, the DM 68nF capacitors have been connected together with the 10nF capacitor from their central point to earth. The ferrite tubes, around the output phase wires, as described in chapter 7 conclude the filter setup.

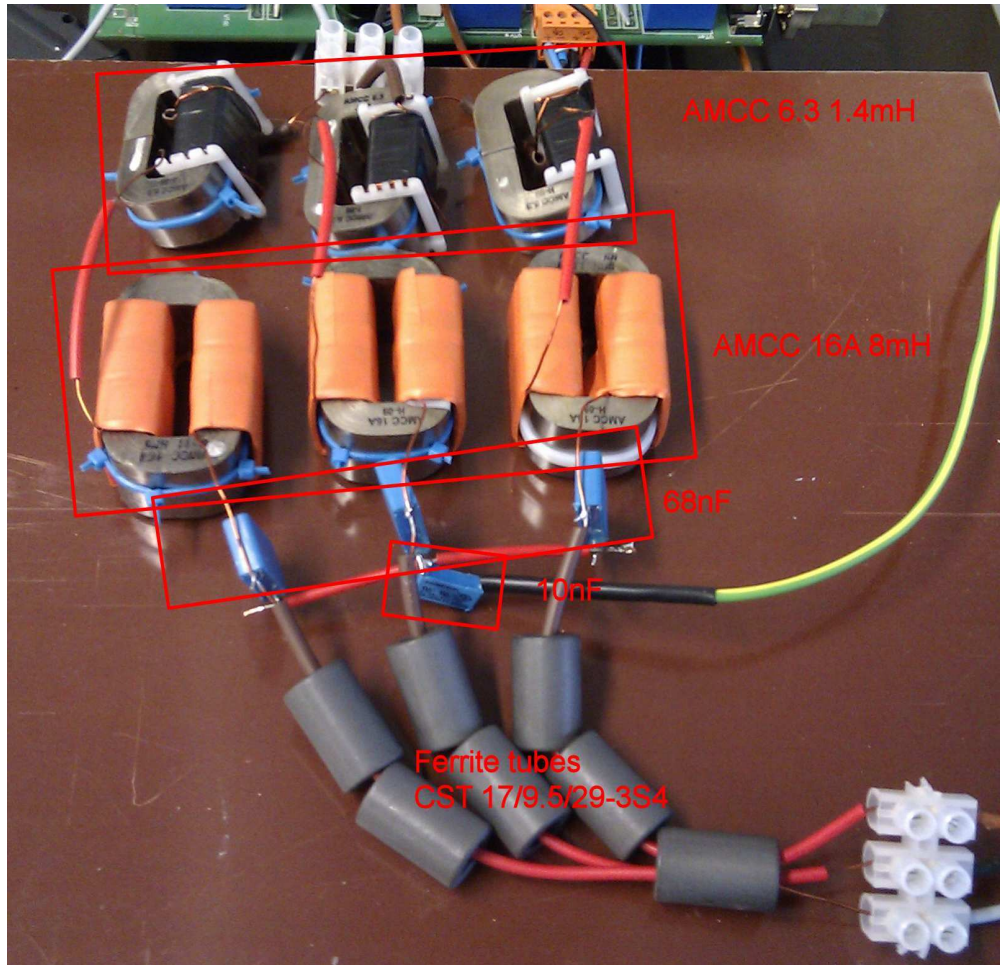


Figure 8.1: Output filter with component details

The final layout for the components can be seen in Fig. 8.1 where all the parts are highlighted; it is worth mentioning that the weight of the whole output EMI filter is 1.5kg, that is almost half of the matrix converter's weight, that is 3.6kg.

8.3 Experimental emission measurements

This section collects and reports the current emission measurements before and after the filter insertion, to provide a final overview of the system after the filter have been set in place. Different measures have been carried out at different voltages and currents: two different input supplies have been fed to the converter: the aircraft one at $115V_{rms}$, 400Hz and the standard grid at $240V_{rms}$, 50Hz. The modulation index, once the motor has started, has initially been kept constant at the final value of 0.7, while two different output frequency have been generated: 50Hz and 100Hz.

A further set of measurements will also report measurements for different values of

the modulation index, to verify the consistency of the filter behaviour. Three values for the modulation index have been chosen: the lower one has experimentally been found in such a way that it will grant the minimum current but still will allow the motor rotation, the higher value has been set to be equal to 0.85 that is close to the theoretical maximum value for this type of modulation, plus a middle value chosen between these two.

8.3.1 Input emissions

This section illustrates that the output filter has no actual influence on the input emissions neither improvement or deterioration for both DM and CM. A first set of figures show the measured input EMI while supplying the converter with an input supply at 115V, 400Hz. The input emission are compared before and after the filter insertion for the two output frequencies generated by the converter: 50Hz and 100Hz. Fig. 8.2 and Fig. 8.3 report the DM emissions while Fig. 8.4 and Fig. 8.5 plot the CM ones.

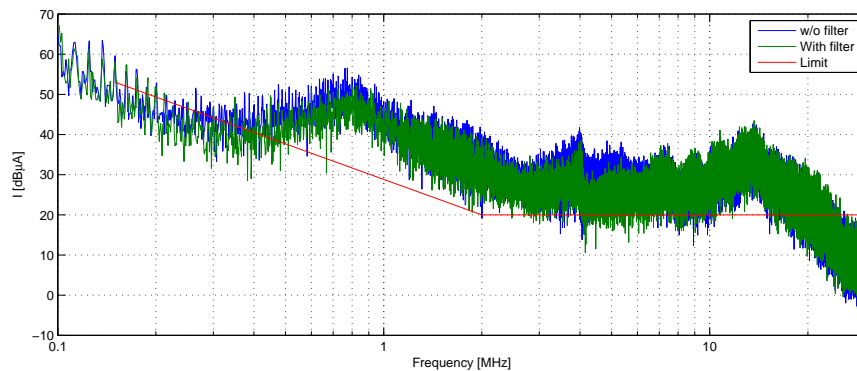


Figure 8.2: Comparison of Measured input DM emissions: without and with output EMI filter (115V-400Hz to 80V-50Hz)

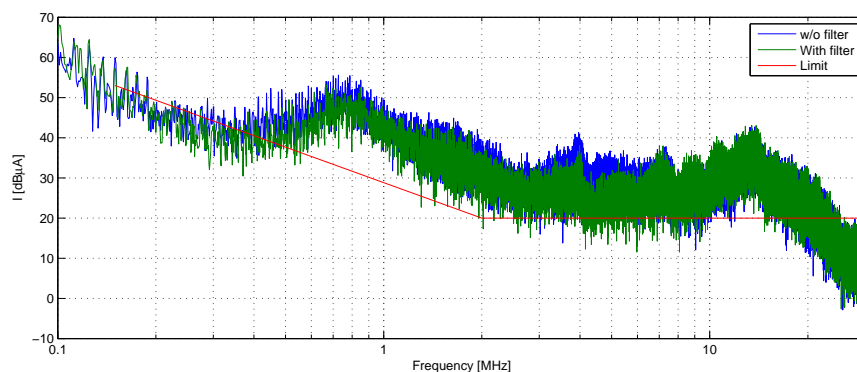


Figure 8.3: Comparison of Measured input DM emissions: without and with output EMI filter (115V-400Hz to 80V-100Hz)

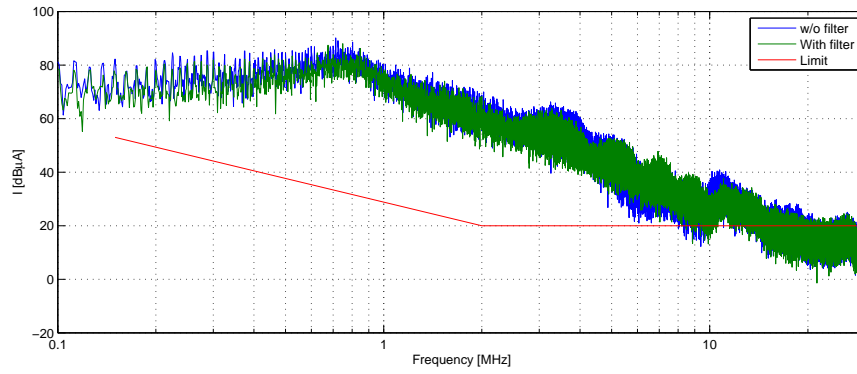


Figure 8.4: Comparison of Measured input CM emissions: without and with output EMI filter (115V-400Hz to 80V-50Hz)

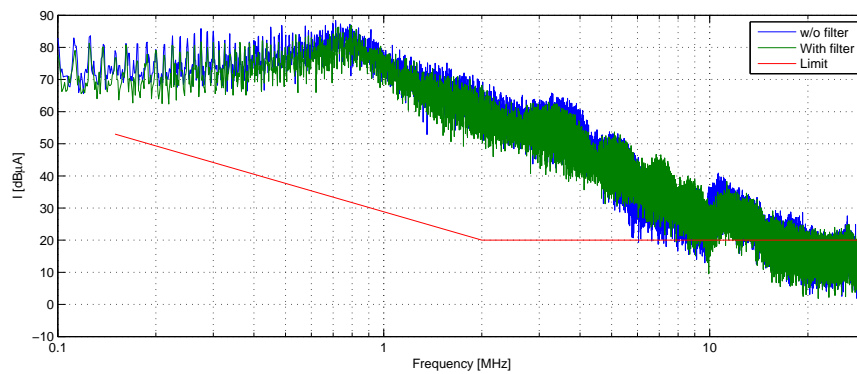


Figure 8.5: Comparison of Measured input CM emissions: without and with output EMI filter (115V-400Hz to 80V-100Hz)

Now the same measurements have been carried out for a standard grid input supply: 240V at 50Hz. This case will generate higher emission due to the higher voltage and higher output current. Again Fig. 8.6 and Fig. 8.7 show the input DM emissions while Fig. 8.8 and Fig. 8.9 illustrate the input CM ones, showing no practical difference, even in this case.

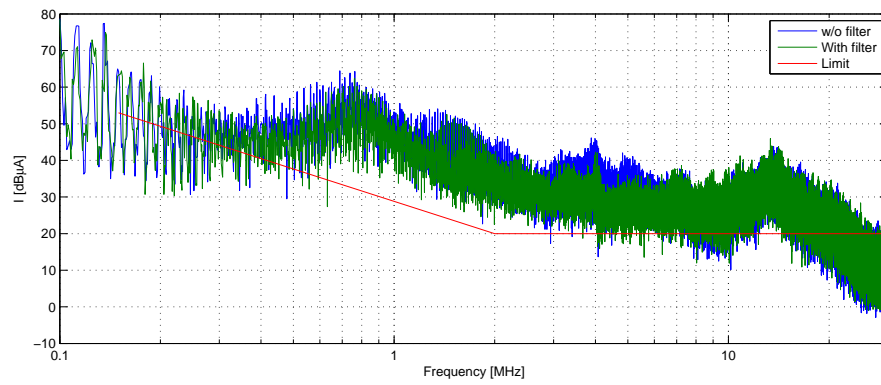


Figure 8.6: Comparison of Measured input DM emissions: without and with output EMI filter (240V-50Hz to 168V-50Hz)

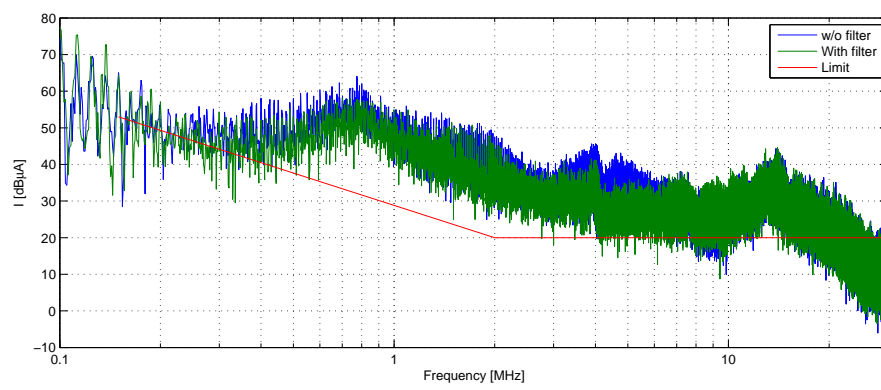


Figure 8.7: Comparison of Measured input DM emissions: without and with output EMI filter (240V-50Hz to 168V-100Hz)

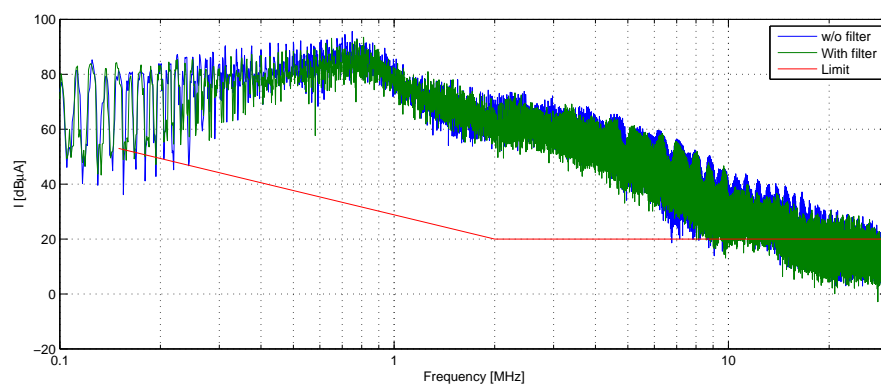


Figure 8.8: Comparison of Measured input CM emissions: without and with output EMI filter (240V-50Hz to 168V-50Hz)

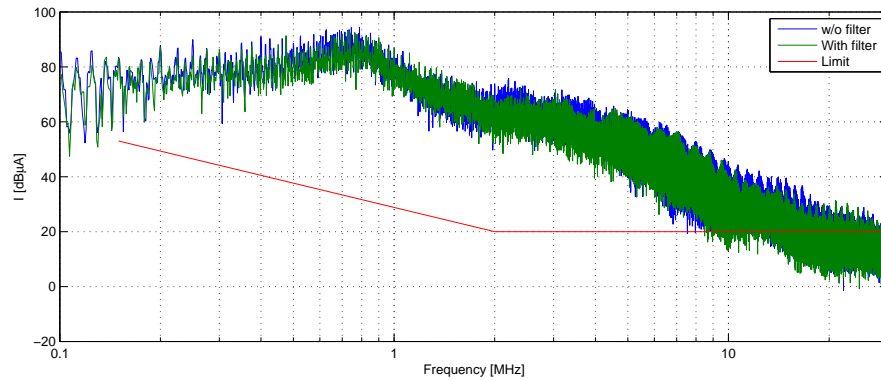


Figure 8.9: Comparison of Measured input CM emissions: without and with output EMI filter (240V-50Hz to 168V-100Hz)

8.3.2 Output emissions

This section will now illustrate the impact of the designed filter on the output emissions. At first the EMI in the case of an aircraft supply system are reported, showing DM emissions (Fig. 8.10 and Fig. 8.11) and CM emissions (Fig. 8.12 and Fig. 8.13) for 50Hz and 100Hz output respectively. In all these cases, experimental measurements demonstrate that the emissions have now dropped under the limit.

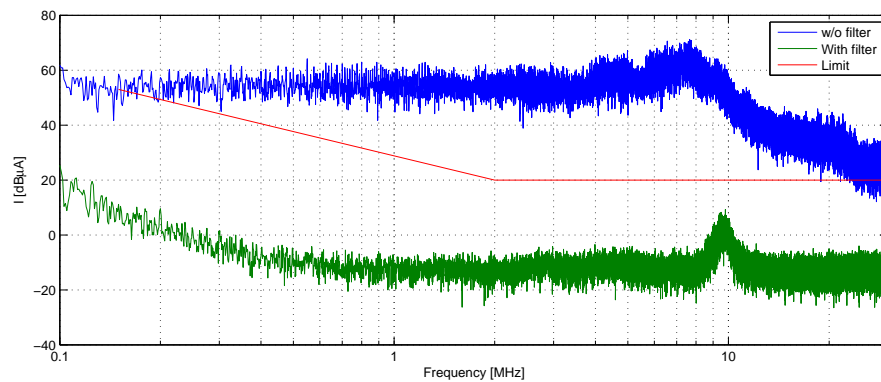


Figure 8.10: Comparison of Measured output DM emissions: without and with output EMI filter (115V-400Hz to 80V-50Hz)

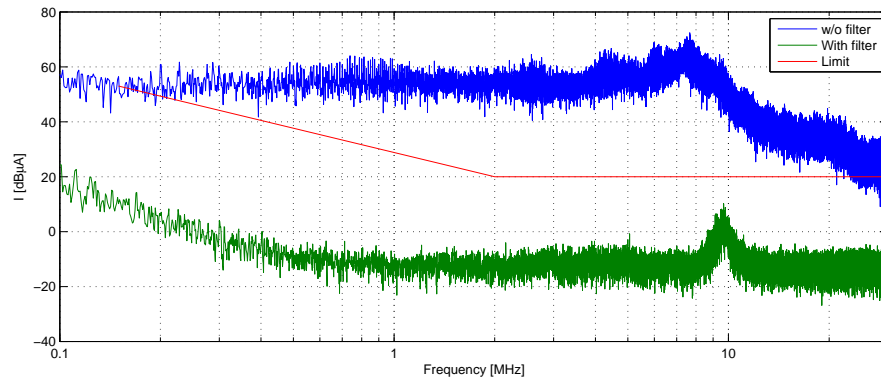


Figure 8.11: Comparison of Measured output DM emissions: without and with output EMI filter (115V-400Hz to 80V-100Hz)

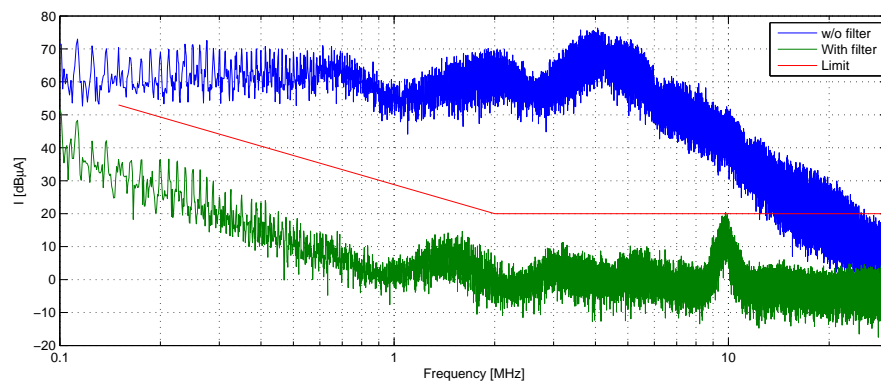


Figure 8.12: Comparison of Measured input CM emissions: without and with output EMI filter (115V-400Hz to 80V-50Hz)

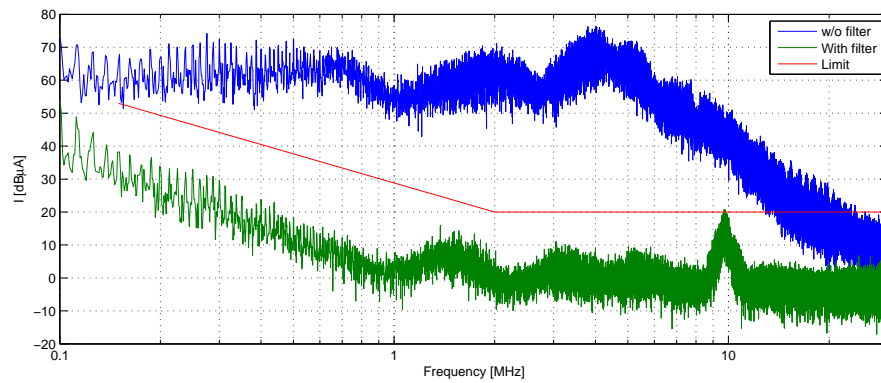


Figure 8.13: Comparison of Measured input CM emissions: without and with output EMI filter (115V-400Hz to 80V-100Hz)

As it can be seen in the first two figures 8.10 and 8.11 regarding the DM emissions, they now are clearly under the standards limit; it may seem a case of over-design for the filter because it could attenuate at least 10dB less. However, as it has been explained

during the filter design, the resonance point of that filter has to be at low frequencies not to encounter problems of resonance with the switching frequency harmonic clusters. With such a design constraint the final attenuation will be more than the one needed, thus resulting in such attenuation. In the common mode case, instead, the filter is attenuating just the needed amount: the new emissions are quite close under the limit also considering the visible peak at 10MHz, thus showing a proper design.

Now, the same measurements will be carried out, once again, for a regular 240V, 50Hz supply, to show that the filter works properly, disregarding the input voltage or frequency. This is shown in figures from 8.14 to 8.17.

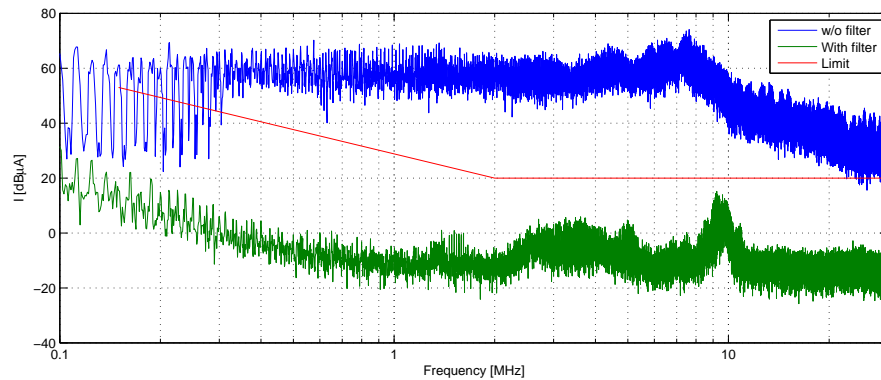


Figure 8.14: Comparison of Measured output DM emissions: without and with output EMI filter (240V-50Hz to 168V-50Hz)

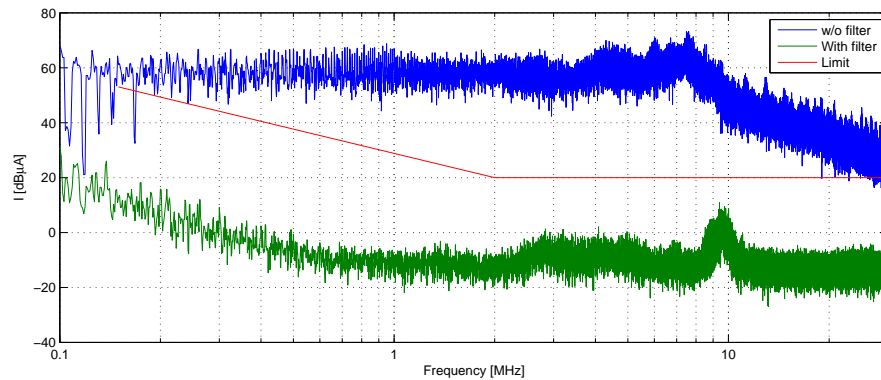


Figure 8.15: Comparison of Measured output DM emissions: without and with output EMI filter (240V-50Hz to 168V-100Hz)

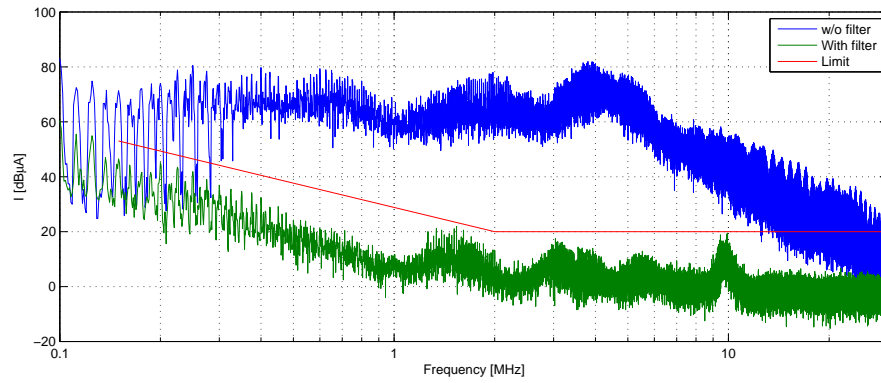


Figure 8.16: Comparison of Measured input CM emissions: without and with output EMI filter (240V-50Hz to 168V-50Hz)

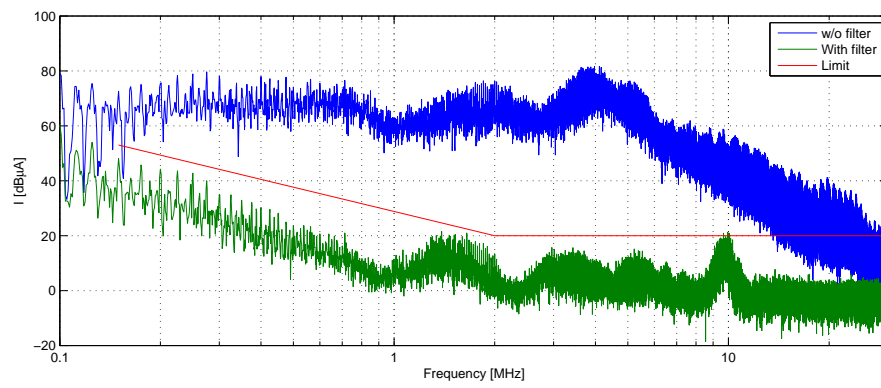


Figure 8.17: Comparison of Measured input CM emissions: without and with output EMI filter (240V-50Hz to 168V-100Hz)

8.3.3 Influence of the modulation index q on the emissions

This last section of measurements reports the emissions for different values of the modulation index, again for an aircraft grid at $115V_{rms}$, 400Hz and a standard one at $240V_{rms}$, 50Hz. For the aircraft supply the six measured cases are grouped in table 8.1, while table 8.2 reports the cases for the standard grid.

$f_{out} = 50\text{Hz}$		$f_{out} = 100\text{Hz}$	
q	I_{rms}	q	I_{rms}
0.35	375mA	0.55	455mA
0.65	500mA	0.7	415mA
0.85	630mA	0.85	420mA

Table 8.1: Modulation index and motor rms current for measurements with aircraft supply at 115V, 400Hz

$f_{out} = 50\text{Hz}$		$f_{out} = 100\text{Hz}$	
q	I_{rms}	q	I_{rms}
0.3	530mA	0.3	400mA
0.6	1A	0.6	560mA
0.8	1.5A	0.85	750mA

Table 8.2: Modulation index and motor rms current for measurements with standard supply at 240V, 50Hz

All the measurements obtained for these cases were compared and no noticeable difference in the emissions was found, disregarding modulation index, input or output fundamental frequency. For this reason here will be reported just few significant measurements: Fig. 8.18 shows the input CM and DM emissions for a standard aircraft supply with the output frequency modulated at 100Hz. For the same case, Fig. 8.19 and Fig. 8.20 will report the DM and the CM output emissions.

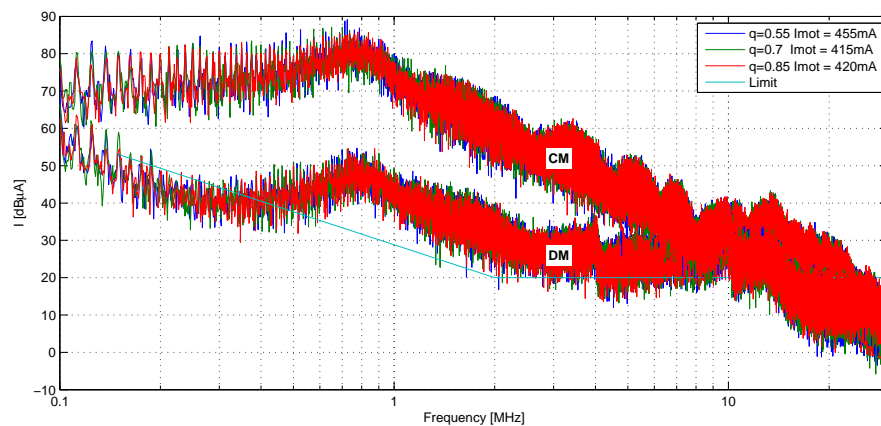


Figure 8.18: Input CM and DM emissions for different values of modulation index q (115V-400Hz input, 100Hz output)

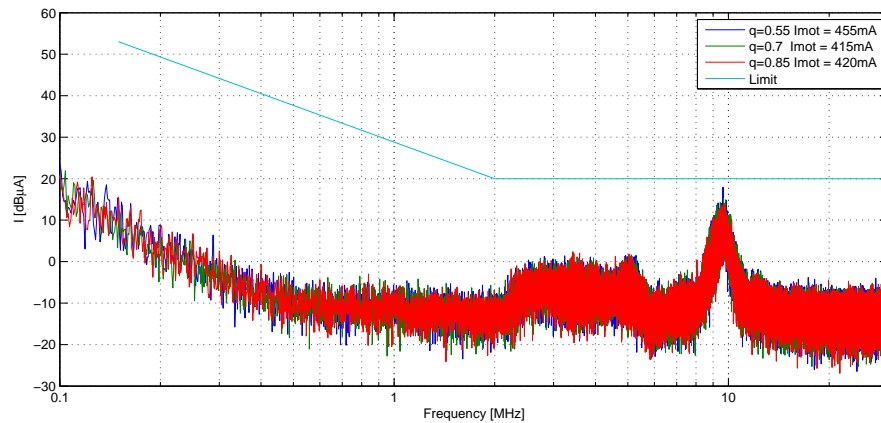


Figure 8.19: Output DM emissions for different values of modulation index q (115V-400Hz input, 100Hz output)

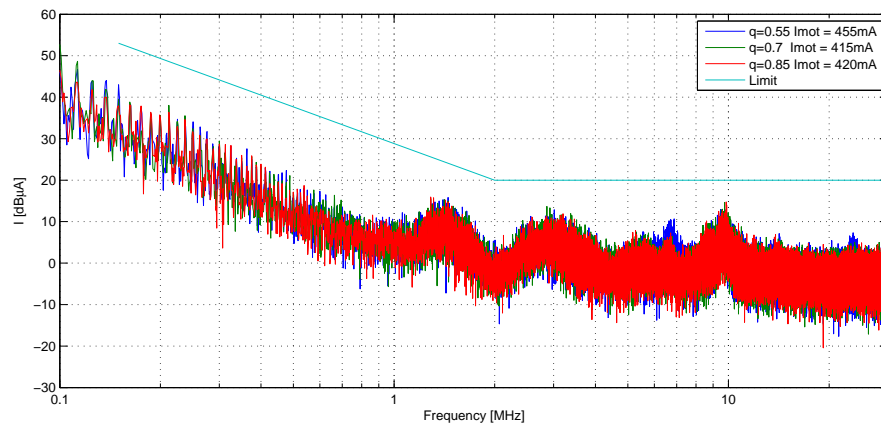


Figure 8.20: Output CM emissions for different values of modulation index q (115V-400Hz input, 100Hz output)

Considering the case of a standard grid supply at 240V and 50Hz, the measurements for 50Hz output frequency is reported because it has the higher output current (Table 8.2). Fig. 8.21 reports the input CM and DM emissions, while Fig. 8.22 and 8.23 deal with the output DM and CM ones. In this case the overall emissions are slightly higher, if compared with the previous case, and this is due to the higher input voltage. However, it is clear that the output current does not play a dominant role on the magnitude of the emissions.

Once again all the measured output EMI are contained under the standards limits, thus validating the performance of the filter.

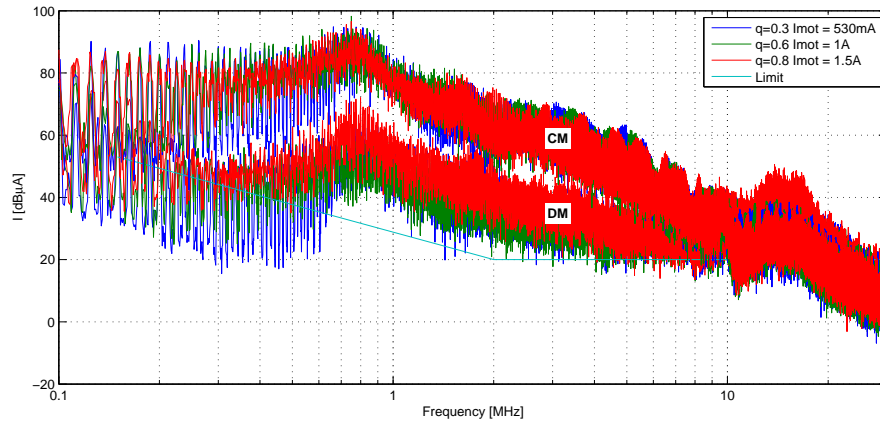


Figure 8.21: Input CM and DM emissions for different values of modulation index q (240V-50Hz input, 50Hz output)

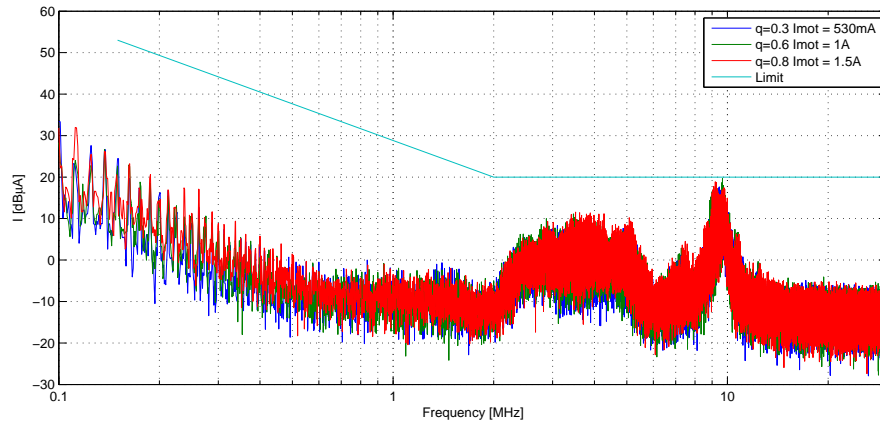


Figure 8.22: Output DM emissions for different values of modulation index q (240V-50Hz input, 50Hz output)

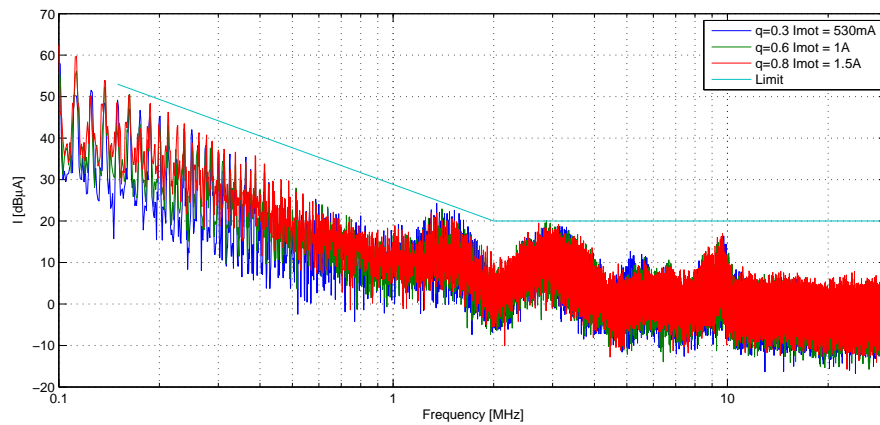


Figure 8.23: Output CM emissions for different values of modulation index q (240V-50Hz input, 50Hz output)

Conclusions and Further work

Any electrical/electronic equipment has to satisfy different EMI emissions standards, according to its specific field of operation. Aircraft standards are defined in [1], and limit the emissions for both common and differential mode for any appliance to be used on an aircraft power systems. EMI filter design needs nowadays to be part of the routine design of any appliance, so it is convenient to start it from an early stage of the design process timeline. For this reason it is vital to be able to estimate the system emissions before having the full system completed; therefore the approach followed in this research work is to provide a detailed procedure to characterize HF models for every part of the system separately and before final assembly.

This thesis has at first focused on the characterization of an Induction Motor drive for aircraft applications based on the use of a Matrix Converter system from the Electro Magnetic emissions point of view. A novel modelling methodology and a set of novel HF models have been provided for the Induction Motor, Matrix Converter; cables and LISN has also been modelled to represent the whole system. The novel methodology used consists in selecting appropriate model structures for both Induction Motor and Matrix Converter, and by identifying each single models parameters value by matching specific system impedance measurements. For the identification, a procedure has been proposed to fit the suggested models using Genetic Algorithms, which provide a fast and reliable method to fit the models by determining different unknown parameters, when only an impedance reference is available. For this application a matrix converter has been built to feed the chosen induction motor and differential and common mode impedances have been measured for the matching exercise. After the modelling has been finalised and the whole drive HF model has been implemented, the simulated emissions could be compared directly with the real experimental ones, showing an excellent accuracy of the estimation.

Based on the attenuation required for the Matrix Converter output emissions (motor side), an output EMI filter has been designed, trying to minimize its weight and fulfilling the requirements for the Aircraft power systems standards that limit the amount of capacitance allowed. For the inductors various materials have been tried, showing clearly a poor performance for the available ferrite materials that proved to saturate even for low values of current, thus losing their filtering capability. The adopted material is an alloy that shows extraordinary capabilities in terms of saturation and performance in high frequency, the Powerlite C from MetGlass. To complete the output filter some small ferrite tubes, made of Ferroxcube 3E4 material that is adequate for very high frequencies, had to be included to damper a peak present in the emissions at around 10Mhz. This peak could not be attenuated with the main components of the designed filter due to the frequency limitation introduced by its intrinsic parasitic components. Complete emission measurements have been carried out after the designed filter insertion to prove the validity of the filter, not just with aircraft 115V, 400Hz supply but also with a standard 240V, 50Hz supply that induced more load current. Emissions before and after the filter insertion have been compared, proving that the Matrix converter drive output, fitted with the filter, will now pass the EMI test procedure. This is a novel achievement since no EMI filter had been implemented in literature for a matrix converter for aircraft applications. Furthermore, additional emission measurements report the effectiveness of the filter when the modulation index in the control algorithm is varied, proving its effectiveness during every operating condition. The input EMI filter, due to time limitations, has only been designed; the design procedure, the input filter schematic and the simulated emissions after its insertion are reported in chapter 7. Its realization is left to a possible follow-up on this work, together with further size, weight and material optimization.

Scientific Publications

A.1 Papers published on refereed International Journals

- M. Degano, P. Zanchetta, E. Lavopa, J. Clare and L. Empringham.
HF Induction Motor Modeling Using Automated Experimental Impedance Measurement Matching. *IEEE Transactions on Industrial Electronics*, Publication Year: 2012, Volume: 59, Issue: 10, Page(s): [3789 - 3796](#)
- M. Odavic, V. Biagini, P. Zanchetta, M. Sumner and M. Degano.
One-Sample-Period-Ahead Predictive Current Control for High Performance Active Shunt Power Filters. *IET Power Electronics Journal*, Publication Year: 2011, Volume: 4, Issue: 4, Page(s): [414 - 423](#)
- J. Liu, P. Zanchetta, M. Degano and E. Lavopa.
Control Design and Implementation for High Performance Shunt Active Filters in Aircraft Power Grids. *IEEE Transactions on Industrial Electronics*, Publication Year: 2011, Volume: 59, Issue: 9, Page(s): [3604 - 3613](#)
- V. Biagini, P. Zanchetta, M. Odavic, M. Sumner and M. Degano.
Control and Modulation of a multilevel active filtering solution for variable speed constant frequency More electric aircraft grid. *Accepted for publication on IEEE transactions on Industrial Informatics*
- M. Degano, P. Zanchetta, J. Liu, P. Mattavelli.
Iterative Learning Control with Variable Sampling Frequency for Current Control of Grid Connected Converters in Aircraft Power Systems. *Accepted for publication on IEE transactions on Industry applications*

- M. Degano, P. Zanchetta, V. Biagini, P. Cortes, J. Rodriguez, M. Perez and S. Cesar
Optimal Dynamic Reference Finite States Model Predictive Control for Active Power Filtering Systems. *Submitted for publication on IEE transaction on power delivery*

A.2 Papers published on refereed International Conferences

- P. Zanchetta, Jun Yi Liu, M. Degano and P. Mattavelli.
Variable Sampling Frequency in Iterative Learning Current Control for Shunt Active Filter in Aircraft. *IEEE Energy Conversion Congress and Exposition (ECCE), Publication Year: 2011, Page(s): [3528 - 3534](#)*
- M. Odavic, V. Biagini, M. Sumner, P. Zanchetta and M. Degano.
Multi-sampled Carrier-Based PWM for Multilevel Active Shunt Power Filters for Aerospace Applications. *IEEE Energy Conversion Congress and Exposition (ECCE), Publication Year: 2011, Page(s): [1483 - 1488](#)*
- M. Degano, P. Zanchetta, J. Clare and L. Empringham.
HF induction motor modelling using Genetic Algorithms and experimental impedance measurement. *IEEE International Symposium on Industrial Electronics (ISIE), Publication Year: 2010, Page(s): [1296 - 1301](#)*
- V. Biagini, M. Odavic, P. Zanchetta, M. Degano and P. Bolognesi.
Improved Dead Beat Control of a Shunt Active Filter for Aircraft Power Systems. *IEEE International Symposium on Industrial Electronics (ISIE), Publication Year: 2010, Page(s): [2702 - 2707](#)*
- J. Liu, P. Zanchetta, M. Degano and H. Zhang.
High Performance Iterative Learning Control for Active Filters in Aircraft Power Networks. *IECON 2010 - 36th Annual Conference on IEEE Industrial Electronics Society 2010, Page(s): [2055 - 2060](#)*

External DLL

B.1 C code

This is the full code for the external library file, this file has simply to be compiled as a "Win32 DLL" with any C compiler, the binary file has to be named ventReal.dll and then placed inside the simulation folder. No others steps are needed.

```
#define _MSC_VER
//All the in/out variables are defined as double
// in the saberApi.h

#define time    inp[0]
#define VA     inp[1]
#define VB     inp[2]
#define VC     inp[3]
#define Vra    inp[4]
#define Vrb    inp[5]
#define Vrc    inp[6]
#define q      inp[7]

#define T11    out[0]
#define T12    out[1]
#define T21    out[2]
#define T22    out[3]
#define T31    out[4]
#define T32    out[5]
```



```

Tseq_Pulses = 4000;    //FPGA_CLOCK/FSW

vin_alpha=(2*VA-VB-VC)*I_3;
vin_beta=(VB-VC)*I_SQRT3;
vin_peak2 = vin_alpha*vin_alpha + vin_beta*vin_beta;
vin_peak = sqrt(vin_peak2);

VoA = Vra;
VoB = Vrb;
VoC = Vrc;

Ksin3wi = (float)4*q/(9*SQRT3)*sin(wit * 3);

m1add = I_3 + sin(wit) * Ksin3wi;
m2add = I_3 + sin(wit-TWOPI_3) * Ksin3wi;
/* m3add = I_3 + sin(wit+TWOPI_3) * Ksin3wi; */

m1dash = ((float)2/3)*VoA/vin_peak2;
m_11 = (m1dash * VA) + m1add;
m_12 = (m1dash * VB) + m2add;
/* m_13 = (m1dash * VC) + m3add;
m_11 = m_11 < 0 ? 0 : m_11;
m_12 = m_12 < 0 ? 0 : m_12;
m_13 = m_13 < 0 ? 0 : m_13; */
Timings[0] = (int)(Tseq_Pulses*(m_11));    //Time A → B
Timings[1] = (int)(Tseq_Pulses*(m_11+m_12)); //Time B → C

m2dash = ((float)2/3)*VoB/vin_peak2;
m_21 = (m2dash * VA) + m1add;
m_22 = (m2dash * VB) + m2add;
/* m_23 = (m2dash * VC) + m3add;
m_21 = m_21 < 0 ? 0 : m_21;
m_22 = m_22 < 0 ? 0 : m_22;
m_23 = m_23 < 0 ? 0 : m_23; */
Timings[2] = (int)(Tseq_Pulses*(m_21));
Timings[3] = (int)(Tseq_Pulses*(m_21+m_22));

```



```

    m3dash = ((float)2/3)*VoC/vin_peak2;
    m_31 = (m3dash * VA) + m1add;
    m_32 = (m3dash * VB) + m2add;
    /* m_33 = (m3dash * VC) + m3add; */
    Timings[4] = (int)(Tseq_Pulses*(m_31));
    Timings[5] = (int)(Tseq_Pulses*(m_31+m_32));

    T11 = (double) Timings[0] / FPGA_CLOCK;
    T12 = (double) Timings[1] / FPGA_CLOCK;
    T21 = (double) Timings[2] / FPGA_CLOCK;
    T22 = (double) Timings[3] / FPGA_CLOCK;
    T31 = (double) Timings[4] / FPGA_CLOCK;
    T32 = (double) Timings[5] / FPGA_CLOCK;

}

```

Note: some calculations have been commented because not needed due to mathematical considerations due to the modulation used, for example $m_{11} + m_{12} + m_{13} = 1$, hence the last term is not needed when the first two are known.

B.2 MAST code

The following code is the MAST code that has to define the modulation block, in order to use the aforementioned DLL inside the saber simulator. A symbol needs to be created with the appropriate ports, and *tsample* and *q* must be passed as parameters of the block.

```
template matrix_ventR VA VB VC Vra Vrb Vrc SA_0 SA_1 SA_2 SB_0
... SB_1 SB_2 SC_0 SC_1 SC_2 sample gnd = tsample
```

```
electrical VA, VB, VC, Vra, Vrb, Vrc
```

```
number tsample
```

```
state logic_4 SA_0, SA_1, SA_2, SB_0, SB_1, SB_2, SC_0, SC_1,
... SC_2, sample
```

```
{
<consts.sin
```

```
state nu T11, T12, T21, T22, T31, T32;
foreign ventreal
```

```
when(dc_init){
  schedule_event(time, SA_0, l4_0)
  schedule_event(time, SB_0, l4_0)
  schedule_event(time, SC_0, l4_0)
  schedule_event(time, SA_1, l4_0)
  schedule_event(time, SB_1, l4_0)
  schedule_event(time, SC_1, l4_0)
  schedule_event(time, SA_2, l4_0)
  schedule_event(time, SB_2, l4_0)
  schedule_event(time, SC_2, l4_0)
} #end dc_init
```

```
when(event_on(sample)){
```

```
(T11, T12, T21, T22, T31, T32, debug1, debug2, debug3, debug4) =
... ventreal(time, V(VA), V(VB), V(VC), V(Vra), V(Vrb), V(Vrc), q)
```

APPENDIX B: EXTERNAL DLL

```
schedule_event (time ,SA_0 ,l4_1)
schedule_event (time ,SB_0 ,l4_1)
schedule_event (time ,SC_0 ,l4_1)

schedule_event (time+T11 ,SA_0 ,l4_0)
schedule_event (time+T11 ,SA_1 ,l4_1)
schedule_event (time+T12 ,SA_1 ,l4_0)
schedule_event (time+T12 ,SA_2 ,l4_1)

schedule_event (time+T21 ,SB_0 ,l4_0)
schedule_event (time+T21 ,SB_1 ,l4_1)
schedule_event (time+T22 ,SB_1 ,l4_0)
schedule_event (time+T22 ,SB_2 ,l4_1)

schedule_event (time+T31 ,SC_0 ,l4_0)
schedule_event (time+T31 ,SC_1 ,l4_1)
schedule_event (time+T32 ,SC_1 ,l4_0)
schedule_event (time+T32 ,SC_2 ,l4_1)

schedule_event (time+tsample ,SA_2 ,l4_0)
schedule_event (time+tsample ,SB_2 ,l4_0)
schedule_event (time+tsample ,SC_2 ,l4_0)
}
}
```

References

- [1] RTCA Incorporated. **RTCA DO-160E, Environmental Conditions and Test Procedures for Airbone Equipment**, 9 December 2004.
- [2] M.H. Rashid. *Power electronics handbook*. Academic Pr, 2nd edition, 2001.
- [3] T. Kume, K. Yamada, T. Higuchi, E. Yamamoto, H. Hara, T. Sawa, and M.M. Swamy. **Integrated filters and their combined effects in matrix converter**. *IEEE Transactions on Industry Applications*, 43(2):571–581, 2007.
- [4] G. Grandi, D. Casadei, and U. Reggiani. **Common-and differential-mode HF current components in AC motors supplied by voltage source inverters**. *IEEE Transactions on Power Electronics*, 19(1):16–24, 2004.
- [5] Ferroxcube Soft magnetic materials, **Ferrites for EMI suppression: 3E27**. Material survey, . ferroxcube.com.
- [6] Epcos, **SIFERRIT, Material N30**. Ferrites and accessories, . epcos.com.
- [7] Magnetics, **Ferrite materials - Toroids**. Ferrite Material Characteristics, . mag-inc.com.
- [8] MetGlass, **POWERLITE Inductor Cores**. Material Data Sheet. metglass.com.
- [9] Richard Lee Ozenbaugh. *EMI Filter Design*. Marcel Dekker, second edition, 2001. Revised and Expanded.
- [10] C.R. Paul. *Introduction to electromagnetic compatibility*. John Wiley & Sons, Inc, 2nd edition, 2006.
- [11] Ma Hongfei, Xu Dianguo, and Miao Lijie. **Suppression techniques of common-mode voltage generated by voltage source PWM inverter**. In *The 4th International Power Electronics and Motion Control Conference, 2004. IPEMC 2004.*, volume 3, pages 1533–1538, aug. 2004.

REFERENCES

- [12] J. Ollila, T. Hammar, J. Iisakkala, and H. Tuusa. **On the bearing currents in medium power variable speed AC drives.** In *IEEE International Electric Machines and Drives Conference Record, 1997*, pages MD1/1.1 –MD1/1.3, may 1997.
- [13] Y. Murai, T. Kubota, and Y. Kawase. **Leakage current reduction for a high-frequency carrier inverter feeding an induction motor.** *IEEE Transactions on Industry Applications*, 28(4):858–863, 1992.
- [14] S. Ogasawara and H. Akagi. **Modeling and damping of high-frequency leakage currents in PWM inverter-fed AC motor drive systems.** *IEEE Transactions on Industry Applications*, 32(5):1105–1114, 1996.
- [15] S. Ogasawara, H. Ayano, and H. Akagi. **Measurement and reduction of EMI radiated by a PWM inverter-fed AC motor drive system.** *IEEE Transactions on Industry Applications*, 33(4):1019–1026, 1997.
- [16] A. Von Jouanne, D.A. Rendusara, P.N. Enjeti, and J.W. Gray. **Filtering techniques to minimize the effect of long motor leads on PWM inverter-fed AC motor drive systems.** *IEEE Transactions on Industry Applications*, 32(4):919–926, 1996.
- [17] M.M. Swamy, K. Yamada, and T. Kume. **Common mode current attenuation techniques for use with PWM drives.** *IEEE Transactions on Power Electronics*, 16(2):248–255, 2001.
- [18] H. Akagi and T. Doumoto. **An approach to eliminating high-frequency shaft voltage and ground leakage current from an inverter-driven motor.** *IEEE Transactions on Industry Applications*, 40(4):1162–1169, 2004.
- [19] S. Ogasawara, H. Ayano, and H. Akagi. **An active circuit for cancellation of common-mode voltage generated by a PWM inverter.** *IEEE Transactions on Power Electronics*, 13(5):835–841, 1998.
- [20] I. Takahashi, A. Ogata, H. Kanazawa, and A. Hiruma. **Active EMI filter for switching noise of high frequency inverters.** 1:331–334, 1997.
- [21] PW Wheeler, JC Clare, M. Apap, L. Empringham, KJ Bradley, S. Pickering, and D. Lampard. **A fully integrated 30 kW motor drive using matrix converter technology.** In *Power Electronics and Applications, 2005 European Conference on*, pages 9–pp. IEEE, 2005.
- [22] K. Yamada, T. Higuchi, E. Yamamoto, H. Hara, T. Sawa, MM Swamy, and T. Kume. **Filtering techniques for matrix converters to achieve environmentally harmo-**

- nious drives.** In *European Conference on Power Electronics and Applications*, pages 1–10. IEEE, 2005.
- [23] IEC CISPR 11, **Industrial, scientific and medical equipment - Radio-frequency disturbance characteristics - Limits and methods of measurement.**
- [24] L. Ran, S. Gokani, J. Clare, K.J. Bradley, and C. Christopoulos. **Conducted electromagnetic emissions in induction motor drive systems. I. Time domain analysis and identification of dominant modes.** *IEEE Transactions on Power Electronics*, 13(4):757–767, 1998.
- [25] L. Ran, S. Gokani, J. Clare, K.J. Bradley, and C. Christopoulos. **Conducted electromagnetic emissions in induction motor drive systems. II. Frequency domain models.** *IEEE Transactions on Power Electronics*, 13(4):768–776, 1998.
- [26] A. Boglietti, A. Cavagnino, and M. Lazzari. **Experimental High-Frequency parameter identification of AC electrical motors.** *IEEE Transactions on Industry Applications*, 43(1):23–29, 2007.
- [27] G. Grandi, D. Casadei, and U. Reggiani. **Equivalent circuit of mush wound AC windings for high frequency analysis.** 1:SS201–SS206, 1997.
- [28] G. Grandi, D. Casadei, and A. Massarini. **High frequency lumped parameter model for AC motor windings.** In *European Conference on Power Electronics and Applications*, volume 2, pages 578–583, September 1997.
- [29] J. Shepherd, A.H. Morton, and L.F. Spence. *Higher Electrical Engineering.* Pitman Pub., 1975.
- [30] L. Gyugyi and B.R. Pelly. *Static power frequency changers: theory, performance, and application.* Wiley New York, 1976.
- [31] P. Wheeler, J. Clare, L. Empringham, M. Apap, and M. Bland. **Matrix converters.** *Power Engineering Journal*, 16(6):273–282, 2002.
- [32] L. Huber and D. Borojevic. **Space vector modulation with unity input power factor for forced commutated cycloconverters.** In *Industry Applications Society Annual Meeting, 1991., Conference Record of the 1991 IEEE*, pages 1032–1041 vol.1, 28 1991-oct. 4 1991.
- [33] M. Venturini. **A New Sine Wave In, Sine Wave Out Conversion Technique Eliminates Reactive Elements.** *Proc. Powercon 7th 1980*, E3:1–15, 1980.

REFERENCES

- [34] P. Wood. **General theory of switching power converters.** in *Proc. IEEE PESC 1979*, 1:3–10.
- [35] A. Alesina and M.G.B. Venturini. **Analysis and design of optimum-amplitude nine-switch direct AC-AC converters.** *IEEE Transactions on Power Electronics*, 4(1): 101–112, 1989.
- [36] N. Burany. **Safe control of four-quadrant switches.** In *Industry Applications Society Annual Meeting, 1989., Conference Record of the 1989 IEEE*, pages 1190–1194. IEEE, 1989.
- [37] P.W. Wheeler, J.C. Clare, L. Empringham, M. Bland, and K.G. Kerris. **Matrix converters.** *IEEE Industry Applications Magazine*, 10(1):59–65, 2004.
- [38] Semikron Semiconductor, **IGBT Bi-Directional Switch Module SK 60GM123.** Device Data Sheet. semikron.com.
- [39] LEM Transducers, **Current transducer LAH 25-NP.** Device Data Sheet, . lem.com.
- [40] LEM Transducers, **Voltage transducer LV-25-P.** Device Data Sheet, . lem.com.
- [41] O.A. Mohammed and S. Ganu. **FE-Circuit Coupled Model of Electric Machines for Simulation and Evaluation of EMI Issues in Motor Drives.** *IEEE Transactions on Magnetics*, 46(8):3389–3392, 2010.
- [42] M. Gen and R. Cheng. *Genetic algorithms and engineering optimization.* Wiley-interscience, 2000.
- [43] Z. Michalewicz. *Genetic algorithms + data structures = Evolution Programs.* Springer, 1996.
- [44] H. Akagi and T. Shimizu. **Attenuation of conducted EMI emissions from an inverter-driven motor.** *IEEE Transactions on Power Electronics*, 23(1):282–290, 2008.
- [45] M. Moreau, N. Idir, and P. Le Moigne. **Modeling of conducted EMI in adjustable speed drives.** *IEEE Transactions on Electromagnetic Compatibility*, 51(3):665–672, 2009.
- [46] A.H. Morton. *Advanced Electrical Engineering.* Longman Scientific & Technical, 1990.
- [47] L. Tihanyi. *Electromagnetic Compatibility in Power Electronics.* Butterworth-Heinemann, Oxford, United Kingdom, 1995.

REFERENCES

- [48] D.F. Knurek. **Reducing EMI in switch mode power supplies.** In *Telecommunications Energy Conference, 1988. INTELEC '88., 10th International*, pages 411–420, oct-2 nov 1988.
- [49] Shuo Wang, Fang Luo, and F.C. Lee. **Characterization and Design of Three-Phase EMI Noise Separators for Three-Phase Power Electronics Systems.** *IEEE Transactions on Power Electronics*, 26(9):2426–2438, sept. 2011.
- [50] B. Muralidhara, A. Ramachandran, R. Srinivasan, and M.C. Reddy. **Experimental investigation and measurement of common mode voltage in a 5-level inverter fed adjustable speed 3-phase Induction Motor drive.** In *Vehicle Power and Propulsion Conference (VPPC), 2011 IEEE*, pages 1–5, Sept. 2011.
- [51] D. Gonzalez, J. Gago, and J. Balcells. **Analysis and simulation of conducted EMI generated by switched power converters: application to a voltage source inverter.** In *Proceedings of the 2002 IEEE International Symposium on Industrial Electronics (ISIE), 2002*, volume 3, pages 801–806, 2002.
- [52] S. Zhang and K.J. Tseng. **Modeling, simulation and analysis of conducted common-mode EMI in matrix converters for wind turbine generators.** In *Power Electronics and Motion Control Conference, 2008. EPE-PEMC 2008. 13th*, pages 2516–2523, sept. 2008.
- [53] K. Raggl, T. Nussbaumer, and J.W. Kolar. **Guideline for a Simplified Differential-Mode EMI Filter Design.** *IEEE Transactions on Industrial Electronics*, 57(3):1031–1040, march 2010.
- [54] Hung-I Hsieh, Jhong-Shu Li, and Dan Chen. **Effects of X Capacitors on EMI Filter Effectiveness.** *IEEE Transactions on Industrial Electronics*, 55(2):949–955, feb. 2008.
- [55] Epcos. **EMI suppression capacitors (MKP).** pages 3–4, May 2009.
- [56] A. Massarini, M.K. Kazimierczuk, and G. Grandi. **Lumped parameter models for single-and multiple-layer inductors.** In *Power Electronics Specialists Conference, 1996. PESC '96 Record., 27th Annual IEEE*, volume 1, pages 295–301, jun 1996.